Improving Cadmium Zinc Telluride Spectrometer Performance and Capabilities

by

Joshua D. Mann

A dissertation submitted in partial fulfillment
of the requirements for the degree of
Doctor of Philosophy
(Nuclear Engineering and Radiological Sciences)
in The University of Michigan
2016

Doctoral Committee:

Professor Zhong He, Chair
Professor Kimberlee Kearfott
Professor Andrew Yagle
Assistant Research Scientist Yuefeng Zhu

ACKNOWLEDGEMENTS

First and foremost I would like to thank my advisor, Prof. Zhong He for his continued support from an undergrad internship through a long PhD program. Early on, his physics-based approach to engineering problems shaped me as a researcher. Later his deep knowledge and thoughtful feedback pushed me to develop new ideas. Were it not for his boundless patience my work would have never reached fruition.

Almost as important to this work are the other contributors to my thesis. I would like to thank the remaining members of my committee: Prof. Kim Kearfott, Prof. Andrew Yagle, and Dr. Yuefeng Zhu for their time, understanding, and constructive criticism of my work. I would also like to thank Prof. Sara Pozzi for her feedback during the my prospectus. Finally, I would like to thank my editors for their time and attention to detail: Sean O'Neal, Jiawei Xia, Bennett Williams, Michael Streicher, and Steven Brown.

None of this work would have been possible if not for those who came before me. Long before my arrival Prof. He cultivated a group of self-motivated individuals intent on building state-of-the-art detector systems, and I am grateful for their guidance. I would like to thank Dr. Feng Zhang for his incredible technical understanding and willingness to teach it, Dr. Hao Yang, Dr. Crystal Thrall, Dr. Weiyi Wang, and Dr. Jason Jaworski for broadening my understanding, and especially Dr. Willy Kaye for taking a risk on an undergrad and bringing me into this group.

I would lastly like to thank my friends and family for emotionally helping me to the end. The unqualified encouragement of my parent's Dave and Karen and pride from my brother Matt pushed me when I wasn't sure I could finish. I would also like to thank my housemates Charles and Kigoma, my friends Alex and Victoria, and my girlfriend Ruby for helping me maintain my sanity.

TABLE OF CONTENTS

CHAPTER

LIST OF FIGURES

Figure

LIST OF TABLES

Table

LIST OF ABBREVIATIONS

CZT cadmium zinc telluride

GM Geiger-Müller

HPGe high purity germanium

BNL Brookhaven National Lab

ASIC application-specific integrated circuit

PCB printed circuit board

GMI Gamma-Medica Ideas

DAQ data acquisition

TAC time-to-amplitude converter

FWHM full width at half maximum

TEC thermoelectric cooler

CAR cathode/anode ratio

TAW time-amplitude walk

SVD singular value decomposition

PHD peak-hold drop

Z atomic number

SRT Shockley-Ramo Theorem

FPGA field gate programmable array

ADC analog-to-digital converter

SNR signal to noise ratio

ABSTRACT

Improving Cadmium Zinc Telluride Spectrometer Performance and Capabilities

by

Joshua Mann

Chair: Zhong He

CdZnTe is the premier semiconductor material for room-temperature gamma-ray spectroscopy and imaging. The high effective atomic number $Z_{\text{eff}} = 52$ and high density $\rho = 6\text{g/cm}^3$ yield excellent detection efficiency; a pixelated detector design allows for 3D position sensitivity and material non-uniformity corrections resulting in $< 1\%$FWHM energy resolution at 662 keV; the wide bandgap $E_{\text{BG}} = 1.61\text{eV}$ permits room temperature operation. Fabrication improvements and the feasibility of floating-temperature operation are analyzed in this work.

Several fabrication changes are tested to mitigate gain nonuniformity in some pixels during operation. Changing the substrate from printed circuit board to ceramic improves operation, maintains spectroscopic performance, and is adopted. Switching the electrode contacts from gold to platinum drastically raises the leakage current and is rejected. Two proprietary fabrication techniques are proposed. The first, fabrication A, raises the leakage, degrades spectroscopic performance, and is rejected. The second, fabrication B, causes greater gain nonuniformity, degrades resolution, and is also rejected.

To reduce system power consumption, a temperature correction algorithm is developed that allows data collection at operating temperatures different from the calibration temperature without performance degradation. This begins with isolating the temperature effects to the detector rather than the readout electronics, and demonstrating the accuracy of the electronic baseline as a surrogate for temperature. Considering the temperature effects, linear gain corrections only partially recover spectroscopic performance and cannot account for pixel nonuniformity or energy nonlinearity.

Parametric corrections pinpoint specific aspects of system operation susceptible to change with temperature. Peak hold drop, depth of interaction, and gain as a function of depth are individually corrected and recover spectroscopic performance almost entirely. To reduce data requirements, the corrections are reapplied assuming separability between the temperature and original parameter domains, with minimal resolution degradation.

CHAPTER I

Introduction and Background

1.1 Radiation and Detection

Radiation is found everywhere both in nature and society. Cosmic radiation cascades through the atmosphere and bombards the Earth from above while terrestrial radiation seeps from below in the form of radon gas. Radiation is used medically for diagnosis and cancer treatment, scientifically to study high-energy physics and the origins of the universe, and daily by the layman to detect smoke and treat food. Engineers have harnessed nuclear power for both potent weapons and consumer electrical generation. This ubiquity necessitates detectors, and the refinement of detection technology leads to specialization both for detectors and radiation applications.

1.1.1 Types of Radiation

Because radiation detectors are often optimally suited to detect certain types of radiation, it is important to categorize those types. Here “radiation” refers specifically to ionizing radiation, particles and photons energetic enough to eject electrons from atomic orbit. Terrestrially it comes primarily in four varieties: alpha, beta, neutron, and photon radiation. Cosmically it is comprised of many exotic particles with very high energies. For common land-based detection applications, cosmic radiation is negligibly rare and on an energy scale so much greater than terrestrial radiation that it is easily isolated and ignored.

Both alpha and beta particles are charged, massive and have a limited range. Alpha particles are He-4 nuclei and are easily stopped by a few centimeters of air[1]. Beta particles are unbound electrons and positrons, and although substantially lighter than alpha particles are stopped by a few millimeters of solid shielding[2]. Together these particles are of limited use for locating and identifying shielded radioactive sources.

While massive, because neutrons have no electrical charge they can travel long distances in air. Despite this property being useful for detection, neutrons are difficult to work with. At high energies they are unlikely to interact with any material[3], making the detection efficiency low. They are most quickly thermalized by low atomic number (Z) organic materials, but once slowed to easily-detectable thermal energies much of the emission information is lost. Unfolding the collected thermal neutron energy distribution into the original emitted spectrum is an unsolved problem for contemporary neutron detectors and an area of active research[4].

Photons are uncharged, massless packets of light, and come in two varieties of ionizing radiation: X-rays and gamma rays. They are generated by different physical processes, but to a radiation detector they behave the same. Gamma rays are typically more energetic and can travel hundreds of meters in air[5]. Common organic materials are mostly transparent to gamma rays, thus high Z, high density materials are needed for efficient detection. Additionally, photons are emitted with quantized energies specific to the emission source[6]. This results in a unique energy signature for each source and consequently allows the gamma-ray sources to be determined from the energy spectrum of a perfect detector. Finally, most nuclear processes release gamma rays of known energy. Taking these properties collectively, gamma rays are the most useful source of radiation for detection and the focus of this work.

1.1.2 Means of Radiation Detection

Originally radiation detection was done via gas-filled detectors. These come in the three varieties: ionization chambers, proportional counters, and Geiger-Müller (GM) tubes. All involve a fill gas held in an electric field between two electrodes. Charged particles, directly via alpha or beta particles, or from secondary emissions due to gamma and neutron interactions, ionize the gas, then the electrons and/or ions are collected and read out by the electrodes. Ionization chambers do not multiply the initial number of free charges, so they produce small pulses proportional to the incident energy and are best suited to high-energy alpha or beta detection[7]. Proportional counters greatly multiply the initial number of free charges proportionally to the incident energy, so they are best suited for low-energy X-ray and neutron detection[8]. GM counters multiply the initial number of free charges to the point of saturation, so they can only act as simply counters. Furthermore, because they cannot differentiate incident energies and gamma-ray detection efficiency varies with energy, they yield unreliable count rates as a gamma-ray detector[9]. Also, interactions in gas-filled detectors can occur either within the fill gas or within the detector walls. The fill gas is typically low density and low Z, making gamma-ray interactions unlikely. The wall can be high Z, but has a very small active volume, also making gamma-ray interactions unlikely. These properties collectively result in a low gamma-ray detection efficiency for gamma rays.

Current gamma-ray detection is usually done via one of two prevailing techniques: scintillation or detection via semiconductors. Both processes begin with a high-energy photon interacting in the detector medium, producing a secondary electron. Scintillation then involves the absorption of the secondary electron and transduction of its energy into visible light[10]. This light is collected by an optoelectronic device, either a photodiode or photomultiplier tube, converted into an electronic signal proportional to the incident photon energy, amplified, and passed to readout electronics.

Inorganic scintillators are often chosen for their simplicity and their relatively inexpensive cost[11]. Organic scintillators trade efficiency for speed, allowing them to discern a higher incident event rate, and the ability to crudely perform both gamma-ray and neutron spectroscopy[12].

With semiconductor detection, the secondary electron slows within the detector medium, exciting a number of additional electrons proportional to its initial energy. These electrons are excited from the valence band to the conduction band, creating mobile electron-hole pairs. The proportionality constant, which is a function of the bandgap, determines how many pairs are created per unit of incident energy. The detector is held under bias so these pairs separate and drift along the electric field lines. This induces a charge on the collecting electrodes, which is amplified and passed to readout electronics. Due to the large number of created electron-hole pairs, the primary advantage of semiconductor detectors is better statistics, thus superior energy resolution[13]. In a scintillator each information carrier requires on the order of 100 eV to produce[14], whereas the bandgap energy of most semiconductor detectors is < 3 eV[15]. This more than thirty-fold increase in the number of information carriers results in reduced statistical variation in the amount collected for identical energy depositions, thus a much better theoretical limit on energy resolution.

1.2 Semiconductor Detectors

1.2.1 Detection Physics

There are three important physical processes by which gamma rays can interact with semiconductor detectors: Compton scattering, photoelectric absorption, and pair production. Compton scattering is an interaction where the incident photon collides with and liberates a bound electron in the detector but is not absorbed. This results in a scattered gamma ray and a liberated recoil electron with energy E_{e^-}, given in Equation (1.1), dependent on both the incident photon energy E_γ and the scattering angle θ, where m_e is the rest mass energy of the electron 511 keV[16]. Photoelectric absorption is an interaction where the incident photon is completely absorbed by a detector atom, ejecting a recoil electron with energy, given in Equation (1.2), equal to the incident photon energy E_γ less the recoil electron binding energy E_b. This binding energy is emitted as either an X-ray or an Auger electron, both of which typically travel only a short distance and generally result in a subsequent full energy deposition in the detector[17]. Pair production requires the strong electric field near the nucleus of a detector atom, but doesn't interact with it. Instead, an energetic photon is replaced by an electron-positron pair with respective energies E_{e^-} and E_{e^+}, given in Equation (1.3), equal in sum to the incident photon energy less twice the electron rest mass energy[18].

$$E_{e^-} = E_\gamma \left(\frac{(E_\gamma/m_e)(1 - \cos\theta)}{1 + (E_\gamma/m_e)(1 - \cos\theta)} \right) \tag{1.1}$$

$$E_{e^-} = E_\gamma - E_b \tag{1.2}$$

$$E_{e^-} + E_{e^+} = E_\gamma - 2m_e \tag{1.3}$$

Spectroscopy is a means of gamma-ray source identification by generating a histogram of incident events by energy, then matching the recorded peaks to known emission energies. Photoelectric absorption results in a single energy deposition equal to the incident photon energy, consequently it is the most useful for gamma-ray spectroscopy. With pair production, the electron has very short range and is typically fully absorbed within the detector, but the positron annihilates with a bound electron, releasing two 511 keV photons. One or both of these photons could undergo photoelectric absorption or escape the detector without interacting, resulting in three different energy depositions. Because this interaction is known, the incident photon energy can be recovered and used constructively for spectroscopy. It is only when the incident photon Compton scatters then escapes that there is a continuum of possible energy depositions and the spectroscopic information lost. Semiconductor materials are therefore chosen to maximize photoelectric absorption and minimize photon escape following Compton scatter. The probability of photoelectric absorption per atom scales with $\sim Z^{4.5}$, of pair production with Z^2, and of Compton scatter with Z, therefore it is desirable that a semiconductor detector have a high atomic number[19].

1.2.2 Material Considerations

There are several material concerns for semiconductor detectors. The first is to characterize and minimize trapping. This is where impurities in the detector material temporarily block the movement of electrons or holes in the detector, effectively trapping them. Although these charges eventually migrate to the electrodes, the charge collection time for each event is limited, and trapping reduces the total induced charge during this time window[20]. This degrades the one-to-one correlation between deposition energy and the magnitude of the readout signal and should be minimized. In terms of material selection, this manifests as a preference for uniform semiconductor crystals.

Finally, a good semiconductor detector seeks to minimize noise. This is also impacted by the configuration of readout electronics, but at the material level requires minimizing leakage current. Again impurities play a role, reducing the effective resistance of a material and increasing leakage. The material itself also plays a role, as smaller bandgaps result in greater leakage current from thermal excitation. This is not a prohibitive concern because thermal leakage can be reduced by cooling a semiconductor detector[21].

1.2.3 Common Detector Materials

Successful semiconductor detectors were initially made from single-element materials, due to the comparative ease of purification and uniform crystal growth. Silicon is the first such material, having been used in radiation detectors since the 1960s. The low atomic number of 14 limits its usefulness as a gamma-ray spectrometer, however. Above the 20 keV energy limit of soft x-rays, Compton scatter is the dominant interaction, and into the high-energy gamma-ray energy range, photons are unlikely to interact at all. Coupled with a thin activation layer in pure silicon diodes, this material is only well-suited for low energy photon and charged particle detection[22].

Directly below silicon on the periodic table is germanium. With very high purity, uniform charge carrier transport, and excellent energy linearity, it is a good candidate for gamma-ray detection[23]. Furthermore the higher Z of 32 improves detection efficiency, and the narrow bandgap generates more charge carriers for a given incident photon energy than other semiconductors. In combination these properties ensure high purity germanium (HPGe) has superior energy resolution and has become the gold standard in gamma-ray semiconductor detectors. The narrow bandgap introduces one significant drawback, however: at room temperature thermal leakage dominates the photon induced charge, thus HPGe detectors require cooling to liquid nitrogen temperatures (77 K) for successful operation[24].

The limitations of the available single-element semiconductors have prompted the search for compound semiconductors suitable for radiation detection. Some target specific applications, such as the temperature-stable and radiation hard SiC for use in heavily irradiated or high temperature scenarios[25]. Most, however, seek to improve the efficiency and fieldability of HPGe. The approach is two-fold: a material with higher density and atomic number yields a more efficient detector, and a wider bandgap reduces the thermal leakage and eliminates the need for cooling. Some of the most widely studied of these compound semiconductors include HgI_2, TlBr[26],

Table 1.1: Comparison on Semiconductor Material Properties (transcribed from [15])

Material	Density g/cm^3	Atomic Number	Bandgap (eV)
Si	2.33	14	1.12
Ge	5.33	32	0.67
SiC	3.21	10	3.26
HgI_2	6.40	62	2.15
TlBr	7.56	58	2.68
CdTe	5.85	50	1.44
CdZnTe	5.78	49	1.57

CdTe[27], and CdZnTe[28]. Their material properties are compared with the elemental semiconductors in Table 1.1.

Although the material properties make the compound semiconductors desirable, practical issues limit their usefulness as radiation detectors. The biggest issue ubiquitous across all materials is uniformity. Creating secondary and tertiary compounds increases the minimum attainable amount of impurities and introduces or increases the likelihood of material defects such as twinning, grain boundaries, metal inclusions, and polycrystallinity[29]. Additionally, unlike the single-element semiconductors, the charge collection times for electrons and holes are different from one another in the four high-Z compound semiconductors. There are also material-specific practical concerns: HgI_2 sublimates at room temperature and requires hermetic sealing[30], and TlBr polarizes at room temperature, requiring cooling to $-20°C$[31].

1.2.4 Cadmium-Zinc-Telluride Detectors

The practical issues surrounding the compound semiconductor materials are challenging, but not insurmountable. The advantages offered by room-temperature operation have prompted decades of research into overcoming them, with CZT currently showing the most promise. Material growth advances[32] and detector readout improvements[33] together have alleviated both CZT problems of imbalanced charge collection time and material non-uniformity.

The charge collection time, derived from the product of charge carrier mobility μ and charge carrier lifetime τ, differ significantly in CZT for electrons and holes. The biggest breakthrough in mitigating this issue was the development of single-polarity charge sensing readout techniques, so the electrons could be recorded and the holes ignored[34]. First accomplished via a coplanar grid[35], a detector in this configuration has a single planar cathode and two interwoven anodes with separate readouts. By recording the induced charge on each electrode and accounting for the weighting potential as explained in 1.3, a signal can be generated that depends only on incident energy, not the position of the interaction in the crystal. This technique has been modified by placing non-collecting electrodes in a ring around the detector near the anode side and measuring the transient induced signal, known as a virtual Frisch grid[36]. It has also been refined by fully pixelating the anode side, resulting in much more information to read out at the expense of much more complicated electronics[37].

With any single-charge sensing technique, the underlying simplification assumes the holes are motionless during the electron collection, thus they do not contribute to the induced charge on any electrode. This was always a fair assumption with the mobility-lifetime product of holes in CZT typically being $\mu_\mathrm{h}\tau_\mathrm{h} \approx 10^{-5}$–$10^{-4}\,\mathrm{cm}^2/\mathrm{V}$ and of electrons originally being $\mu_\mathrm{e}\tau_\mathrm{e} \approx 10^{-3}\,\mathrm{cm}^2/\mathrm{V}$[38]. With improved crystal growth technique, the validity of this assumption has only increased, as current Redlen detectors usually exceed $\mu_\mathrm{e}\tau_\mathrm{e} > 10^{-2}\,\mathrm{cm}^2/\mathrm{V}$[39].

The driving force behind improving crystal growth has always been material uniformity. More than fifteen years ago, vendors grew crystals via the high-pressure Bridgman method and with reasonable yield, volumes were limited to $10 \times 10 \times 10\,\mathrm{mm}^3$[40]. After more than a decade of refinement and transitioning to the traveling heater method, Redlen can reliably grow large-volume $20 \times 20 \times 15\,\mathrm{mm}^3$ CZT crystals with high uniformity and a low concentration of defects[41]. Utilizing pixelated anodes also alleviates material non-uniformity. Each pixel can be calibrated individually so bulk property differences that vary slightly from pixel to pixel are corrected for and material non-uniformities in one pixel do not impact the performance in another pixel[42].

Pixelation offers one additional advantage to CZT detectors in the form of reduced leakage current. Assuming the leakage is roughly uniform, the bulk leakage is evenly divided into each pixel. For example, with a resistivity $\rho \approx 10^{10}$–$10^{11}\,\Omega$/cm[43], an average large-volume detector with cathode biased to -3000 V generates 60 nA leakage current. Using pixelation of at least 8 × 8, this is brought below 1 nA per channel and drastically reduces the leakage-induced noise. Pixelation therefore serves to improve the signal to noise ratio (SNR) and increase the maximum bias. Because increasing bias reduces the effects of trapping, this increases τ and effectively reduces the charge collection time.

1.3 Shockley-Ramo Theorem

In order to interpret the induced electrical signals on a given electrode to determine useful information about the incident gamma-ray energy deposition, the Shockley-Ramo Theorem (SRT) is used. Physically, radiation interacts within the semiconductor detector and its energy is transduced into a cloud of electron-hole pairs. This charge cloud moves the through the detector along the electric field lines until it is collected by the terminal electrodes. Counterintuitively, it induces a time-dependent charge on all electrodes throughout the duration of its movement through the detector, not just at the moment of collection and not just on the collecting electrode. SRT proves a simple relationship between the magnitude of the charge cloud and the charge induced on the electrodes, generating a one-step conversion backwards from the electrode charge read out by the system electronics to the energy deposited by an incident gamma ray.

1.3.1 Mathematical Formulation

The brute force approach to calculating induced charge, Q, requires integration of the normal component of the instantaneous electric field $\boldsymbol{E}$ over the electrode surface $\boldsymbol{S}$ for each point along the trajectory of the moving charge q. This is shown in Equation (1.4), where ϵ is the dielectric constant of the semiconductor medium[44].

$$Q = \oint_{\boldsymbol{S}} \epsilon \boldsymbol{E} \, d\boldsymbol{S} \tag{1.4}$$

Making minor assumptions that there is no external magnetic field and that space charge within the detector is stationary, the charge in the detector can be separated into two components: first the space charge and moving charge in an identical detector with grounded electrodes, and second a biased detector absent any space charge or moving charge. The components of the induced charge can similarly be separated into an electrode potential component, a space charge component, and a moving charge component. Because electrode bias is constant and space charge is immobile within the detector, only the moving charge component varies with time. Furthermore, due to the separated formulation, it is independent of electrode bias.

Using only the conservation of energy, a much simpler relationship between the moving charge and induced charge is proven[45]. Calling φ_0 the weighting potential, the charge induced on an electrode only depends on the position of the moving charge within the medium, as shown in Equation (1.5).

$$Q = -q\varphi_0(\boldsymbol{x}) \tag{1.5}$$

This formulation eliminates the need for integration and makes the only challenge calculating the weighting potential. This unitless parameter is calculated by setting the collecting electrode to unit bias and all others to zero, determining the electric field, then calculating the divergence, as shown in Equation (1.6).

$$\boldsymbol{E}(\boldsymbol{x}) = -\nabla\varphi(\boldsymbol{x}) \tag{1.6}$$

With the weighting potential precalculated for a given detector geometry, converting between the induced and moving charge is a one-step process[46]. This simplification is applied to existing geometries, but has also shaped the engineering of detectors into new geometries that yield additional information.

1.3.2 Engineering Applications

SRT is built entirely from physics, but has important applications in the design of semiconductor detectors. Applied to the most basic detector, a planar configuration where the spatial extents of the electrodes are much greater than the thickness of the detector, the weighting potential is linear on both electrodes, as seen in Figure 1.1. Although this is simple to construct and calculate, the induced signal depends linearly on both the position of interaction within the detector and the incident energy deposition. Because only the electrons move quickly in CZT, given a reasonable charge collection time both electrodes will generate an equivalent signal that depends on both energy and depth. With one output and two unknowns, neither energy nor depth of interaction can be determined from this detector configuration.

A better approach places an additional electrode called the Frisch grid between the cathode and anode, very near the anode[47]. The Frisch grid bias is proportionally lower than the anode such that there is a similar operating field throughout the entire detector bulk. With this design, the cathode weighting potential is identical to the planar configuration but the anode weighting potential is zero between the cathode and Frisch grid, increasing rapidly between the Frisch grid and anode, as shown in Figure 1.2. This position-independence throughout the active region means the anode signal depends only on the charge deposition. With two independent electrode outputs and two unknowns, this electrode configuration is the simplest

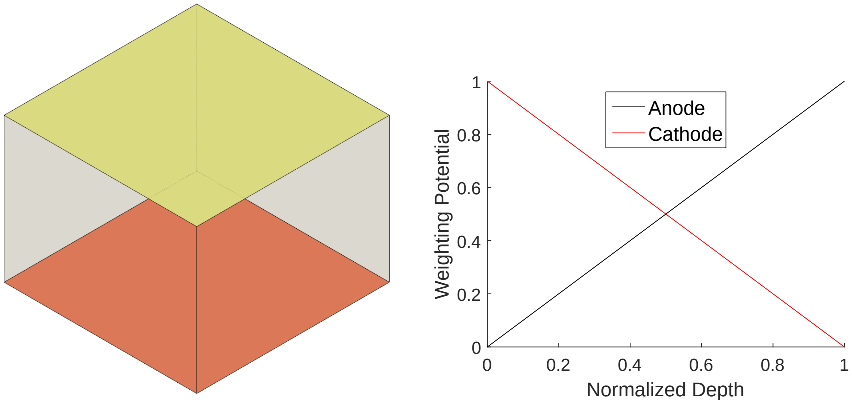

(a) (b)

Figure 1.1: Planar detector configuration (a) and weighting potential (b) with the anode shown in yellow and the cathode shown in red.

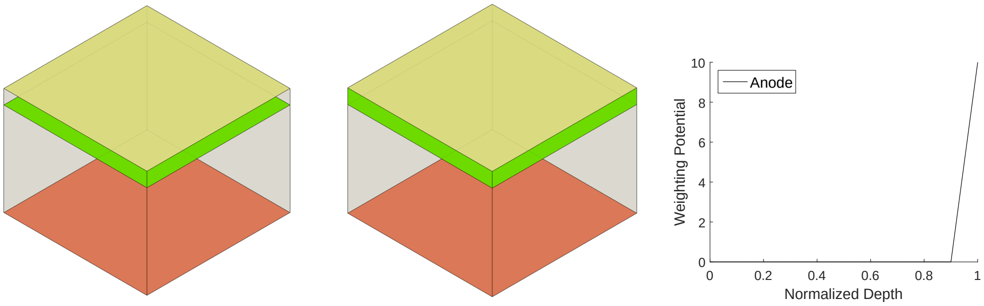

(a) (b) (c)

Figure 1.2: Frisch grid (a) and virtual Frisch grid (b) detector configurations and weighting potential (c) with the anode shown in yellow, the cathode shown in red, and the (virtual) Frisch grid electrodes shown in green.

where the energy and position can be determined. Unfortunately, placing an electrode within the detector bulk would ruin the monocrystallinity required in a semiconductor detector, so a virtual Frisch grid must be used instead. Here only the side surfaces very near the anode terminate into an electrode near the anode bias[48]. The uniform electric field assumption is not as strong near the center of the anode with this virtual configuration.

The coplanar grid configuration eliminates the weakness of the virtual Frisch grid and mitigates the dead region of all Frisch grids. There is once again a planar cathode, but there are two intertwined anode electrodes that each cover half of the anode sur-

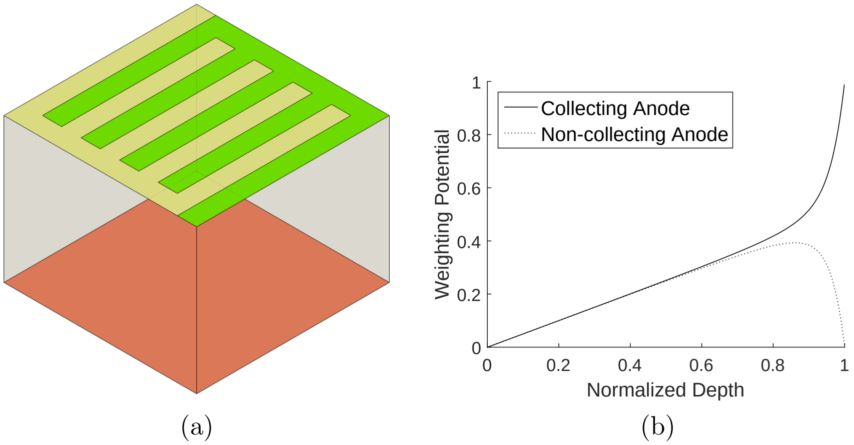

(a) (b)

Figure 1.3: Coplanar detector configuration (a) and weighting potential (b) with the collecting anode shown in yellow, non-collecting anode shown in green, and the cathode shown in red.

face. These are held at the same bias and generate a uniform electric field throughout the detector bulk. Assuming the electron cloud formed during a gamma-interaction is smaller than the pitch between the electrodes, each deposition will occur under a single anode. However, for events that occur relatively far from the anode side, the weighting potential is shared nearly evenly between the collecting and non-collecting anodes, as shown in Figure 1.3. Taking the difference in outputs from each electrode yields a signal that is nearly zero throughout the detector bulk, only rapidly rising to unity very near the anode surface. This effectively removes the depth dependence from the anode signal, so similar to the Frisch grid the anodes and cathode in conjuction can be used to determine the incident energy and depth of interaction[49].

A logical extension of the coplanar configuration is the cross-strip configuration, where both the anode and cathode are divided into narrow strips with independent readout. The anode strips are orthogonal to the cathode strips so that the x and y position of the gamma-ray interaction can be determined simply from which strips collect the event. The weighting potential, shown in Figure 1.4 is an exaggeration of the coplanar configuration, with the signal now being shared between many anodes until collection. Once again a subtraction of the signals is depth-independent, a

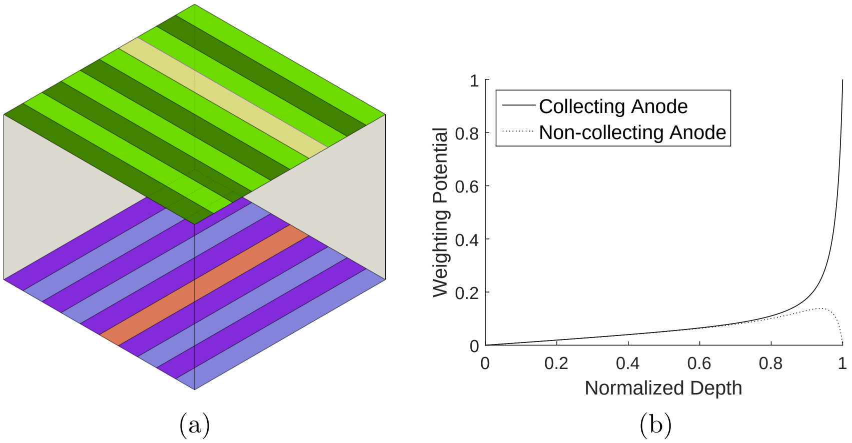

Figure 1.4: Cross-strip detector configuration (a) and weighting potential (b) with the collecting anode shown in yellow, non-collecting anodes shown in alternating shades of green, the collecting cathode shown in red, non-collecting cathodes shown in alternating shades of blue, and the plotted non-collecting weighting potential belonging to the nearest neighbor of the collecting anode.

summation of the cathode signals from each strip is depth and energy dependent, and together they can determine the depth and energy of interaction[50].

A further extension is the pixalated configuration. Here a planar cathode is once again used, and position sensitivity is preserved by dividing the anode into pixels. Seen in Figure 1.5, the weighting potential is a larger exaggeration of the coplanar weighting potential, with the value for the collecting pixel being so small far from the anode side that signal subtraction is often unnecessary. Knowing the collecting pixel gives the x and y position, the depth-independent anode signal provides the energy of interaction, and the ratio of the anode and cathode signals yields the depth of interaction[51].

The point on the weighting potential curve where the anode weighting potential begins to rapidly rise is called the inflection point. For both cross-strip and pixelated detector configurations, the distance between the inflection point and the anode surface is determined by the pitch between anodes. The smaller each collecting anode is relative to the entire surface area, the longer induced charge is shared with non-collecting anodes, and the nearer the inflection point is to the anode surface[52]. This

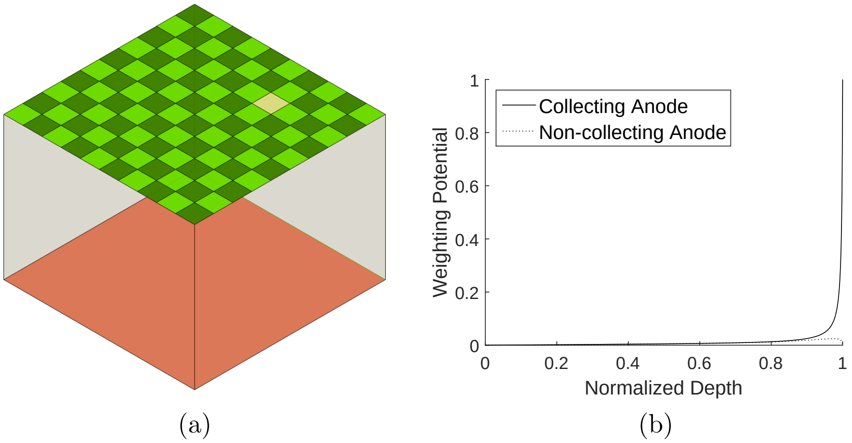

(a) (b)

Figure 1.5: Pixelated detector configuration (a) and weighting potential (b) with the collecting anode shown in yellow, non-collecting anodes shown in alternating shades of green, the cathode shown in red, and the plotted non-collecting weighting potential belonging to the nearest neighbor of the collecting anode.

is known as the small-pixel effect.

Intuitively, cross-strip detectors seem advantageous over pixelated because they provide the same information but require $2n$ electrodes rather than the n^2 needed for pixelation, where n is the number of strips/pixels in each dimension. The advantages of pixelation are purely practical, but substantial. First, although it requires many more preamplifiers, with pixelation all of them are on the anode side, so the anode can be grounded while the cathode is negatively biased. Conversely, with cross-strips at least half of the preamps will operate on biased electrodes, complicating the electrical design. Furthermore, assuming uniform detector material, the leakage current passing through each electrode is proportional to the fraction of the surface covered by each electrode. This means pixelated detectors see leakage reduced by a factor of n compared with cross-strip detectors and n^2 compared with single-anode detectors. For these reasons, pixelated detectors are the focus of this work.

1.4 Imaging

With an understanding of SRT and the subsequent development of single-charge sensing techniques, an additional advantage for CZT detectors emerged. Their position-sensitivity makes them suitable for gamma-ray imaging. CZT systems use two primary means of imaging gamma rays, depending on the incident energy: Compton imaging and coded aperture imaging. The cross-sections, shown in Figure 1.6 indicate that Compton scattering is dominant at intermediate energies, meaning for energies from hundreds of keV to several MeV, CZT systems are suitable Compton cameras.

Compton imaging requires each photon interact at least twice within a detector, beginning with a Compton scatter and ending with a photoelectric absorption. For each interaction, the deposited energy and the x,y,z coordinates are known. The scattering angle θ is a function of the incident photon energy E_γ and the scattered photon energy E'_γ, where $E'_\gamma = E_\gamma - E_{e^-}$, as shown in Equation (1.1). Taking the energy deposition of the photoelectric absorption to be the scattered photon energy and the total deposition of both interactions to be the incident photon energy, the scattering angle is found. The vector between the two interactions represents the photon trajectory after scatter, so a cone drawn around the vector with angle θ represents the possible incident photon trajectories, as illustrated in Figure 1.7. While a single photon points to all directions on a cone, overlapping the cones from many interactions with different scattering angles eventually converges to the source direction[53]. This is illustrated in Figure 1.8 for a single interaction, several interactions where a hot-spot begins to emerge, and many interactions where the hot-spot has converged to the source direction.

For lower energies where photoelectric absorption is the dominant interaction in CZT, another imaging mode is used. Here a mask comprised of materials transparent and opaque to gamma rays in the target energy range is placed between the detec-

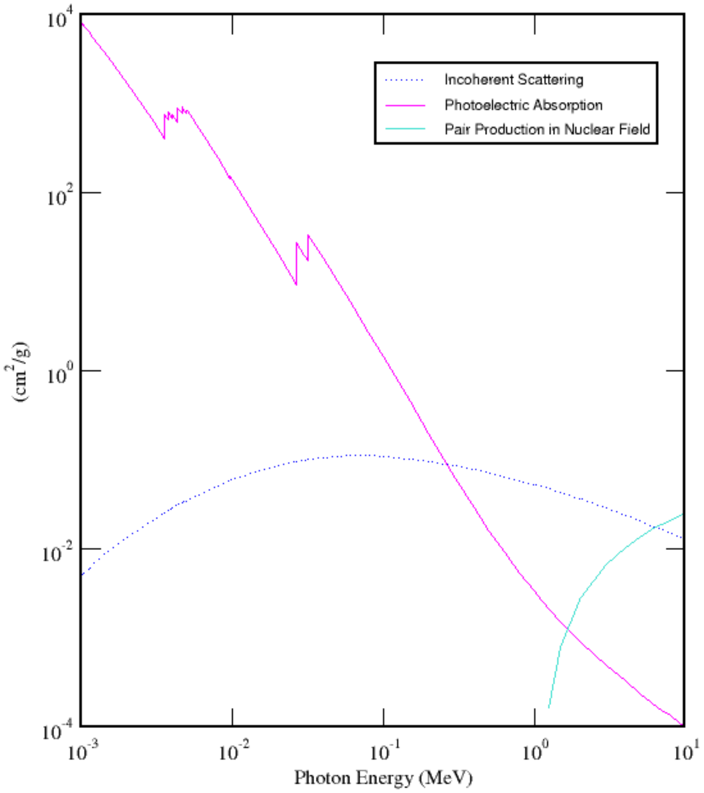

Figure 1.6: Gamma-ray interaction cross-sections for photoelectric absorption, incoherent (Compton) scatter, and pair production in CZT material (taken from [54]).

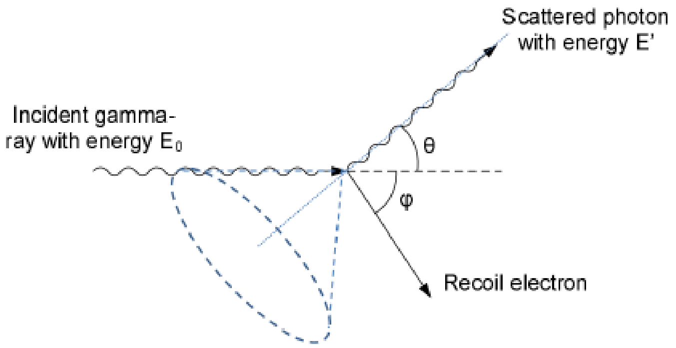

Figure 1.7: Illustration of Compton scattering and determination of Compton cone (taken from [55]).

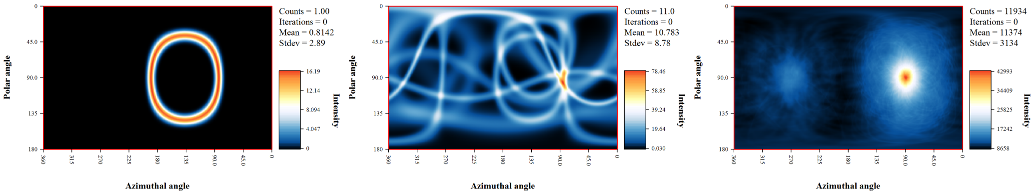

(a) (b) (c)

Figure 1.8: Overlapping Compton rings starting with single event (a), increasing to several events (b) and converging after many events (c).

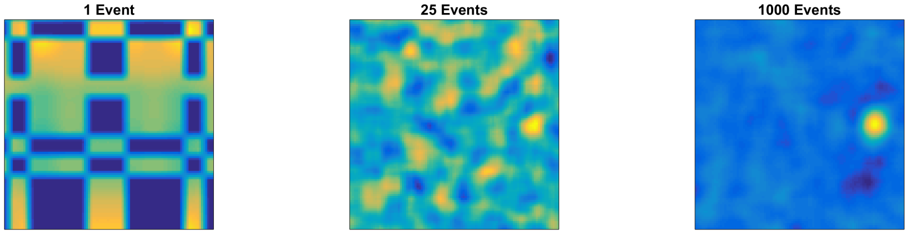

(a) (b) (c)

Figure 1.9: Shadows cast by photons passing through coded aperature starting with single event event (a), increasing to several events (b) and converging after many events (c).

tor and possible radiation source locations. A flood of photons through these mask elements casts a shadow because regions of the detector beneath an opaque element never see any events. The mask is arranged in a known configuration, so the position of the shadows depend only on the source position. While the source direction after a single event is ambiguous because there are many transparent elements it could have passed through, by combining the shadows cast by many events convergence is reached[56]. This is illustrated in Figure 1.9 for a single event where the possible directions match the mask pattern, for several events where only a few possible directions are likely, and for many events where the source direction has converged.

1.5 CZT Systems

Both because of room temperature operation and imaging capability, CZT detectors have been in development as detector systems for as long as CZT has been a viable semiconductor material. Several research systems from outside of the University of Michigan Orion group have been built. Additionally the Orion group and offshoots have developed several generations of steadily improving CZT systems.

Dr. Ralph James' group at Brookhaven National Lab (BNL) has the simplest CZT system with position sensitivity[57]. Abandoning pixelation altogether, they use a virtual Frisch grid with four isolated side-electrodes instead of a single ring. The x,y interaction position is determined by taking the ratio of the induced transient signal on each side electrode. With this method, they achieved $< 1.0\%$ full width at half maximum (FWHM) energy and 0.3 mm FWHM spatial resolution in a 6×6 array of $6 \times 6 \times 15$ mm^3 detectors for Cs-137. They have the advantage of simplified electronics and cheaper construction at the cost of substantially reduced efficiency. As opposed to a pixelated design where interactions occurring in different pixels of the same detector are recorded, for Compton events to register in a virtual Frisch grid system they must scatter in one detector and be absorbed in another.

Dr. Carolyn Seifert's group at Pacific Northwest National Lab used a more traditional pixelated approach in designing the GammaTracker CZT detector system[58]. Using two 3×3 planes of $15 \times 15 \times 10$mm^3 detectors and a Cs-137 source, the system was designed to achieve 1% FWHM energy and 0.5 - 1.2 mm FWHM spatial resolution while maintaining good Compton efficiency. While it set a high performance benchmark, it was never completed due to electronics issues.

The Orion group under Dr. Zhong He at the University of Michigan has a long history of developing high-performance CZT detector systems. Beginning in the late 1990s, this group was the first to demonstrate the depth-sensitivity of pixelated devices using SRT, as well as the first group to demonstrate Compton imaging within a single crystal[59]. Years of research led to increased crystal size and uniformity, improved ASIC design, and ultimately improved system design. The analog Polaris system, described in section 2.1, achieved 0.96% FWHM energy resolution for events occurring in only one pixel, and 1.21% FWHM energy resolution for all events combined at 661.7 keV. It also achieved 0.3 mm FWHM spatial resolution in the depth direction and 1.7 mm FWHM spatial resolution in the x,y directions[60].

There are several improvements to the Polaris system currently under development. Using a low-noise analog ASIC developed by BNL in collaboration with the Orion group, single detectors have achieved 0.48% FWHM single-pixel and 0.71% FWHM overall resolution[61]. Using a digital ASIC, where the waveforms from each pixel are digitized and sampled, even better resolution has been shown. Additionally, similar to the BNL virtual Frisch grid system, the transient induced signals on pixels neighboring the collecting pixel can be compared, allowing for sub-pixel spatial resolution reducing it to approximately 0.3 mm FWHM in the x,y directions[62]. Although these designs offer significant improvements over the Polaris system, they are under active development, thus the Polaris design is the focus of this work.

CHAPTER II

Polaris Systems

2.1 Polaris

2.1.1 Hardware

All Polaris systems use the same standardized detectors: single-crystal CZT with a planar cathode and an 11×11 pixelated anode. Each crystal is mounted on a carrier board, made either of printed circuit board (PCB) or Rogers ceramic, which connects the anode pads to pins that interface with an ASIC. The x,y dimensions of each detector are 20mm × 20mm, while the depth varies by design series. The 1.72 mm pitch between pixels was chosen because it is small enough to take advantage of the small-pixel effect, but much larger than the expected electron cloud size for common laboratory gamma-ray sources[63]. Detectors designated 1R are 5 mm thick, 2R are 10 mm thick, and 3R through 5R are 15 mm thick. Collectively referred to as large-volume detectors, the 15 mm thick detectors vary by anode electrode design. In both 3R and 5R series detectors, there is simply a gap between anodes. It is wide in the 3R detectors and narrow in the 5R detectors. 4R detectors have a 100 μm wide steering grid between pixels with an additional 200 μm gap on either side of the grid. This grid is slightly biased below the anode and is used to steer electrons that would otherwise be lost to gap towards the collecting anodes. All electrodes are typically

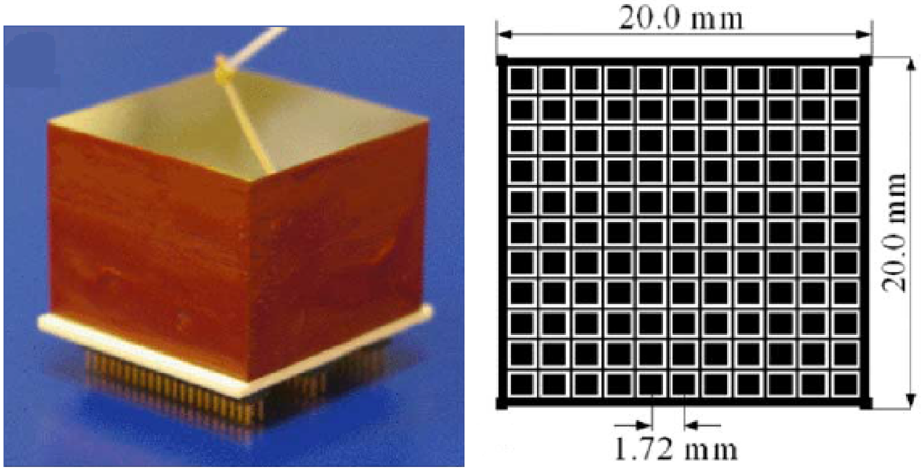

(a) (b)

Figure 2.1: Polaris 4R series detector (a) and pixelation schematic (b).

made of gold in Polaris detectors. A 4R series detector photograph and schematic are shown in Figure 2.1. During operation,an electric field of $2 * 10^5$ V/m is maintained across all detectors. Because the anode electrodes are grounded, this necessitates a cathode bias of -1000 V in the 1R detectors, -2000 V in the 2R detectors, and -3000 V in the large-volume detectors. The grid bias has negligible effect on the shape of the electric field throughout the bulk thus is optimized between -30 V and -200 V independently for each detector irrespective of the detector thickness.

The Polaris systems studied in this work all use VAS_UM2.3/TAT4 ASIC designed by GMI. This circuit, shown visually in Figure 2.2 and schematically in Figure 2.3 connects to an individual detector and mounts to the motherboard. The ASIC houses the preamplifier circuitry, converting the charge induced on each electrode to a voltage signal that is read by the motherboard and sent to a data acquisition (DAQ) computer. The ASIC generates two signals for each anode event, one for the magnitude and one for the timing, by splitting the preamplifier signal through a fast (100 ns) and slow (1 μs) shaper. The fast shaper provides statistically unreliable magnitude information but faster timing information, so once it exceeds a minimum trigger threshold it passes through a time-to-amplitude converter (TAC), generating the event time. Each time

(a) (b)

Figure 2.2: GMI VAS_UM2.3/TAT4 ASIC from top/detector side (a) and bottom/MOCA side (b).

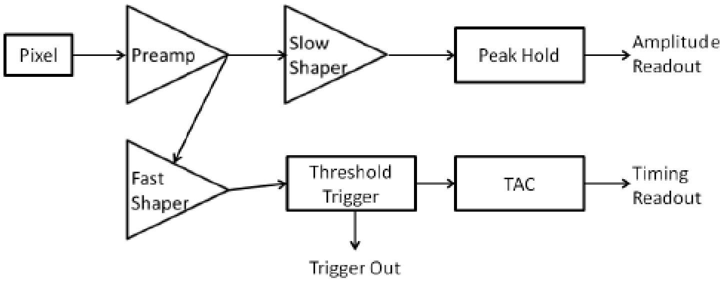

Figure 2.3: Circuit diagram for single channel of GMI VAS_UM2.3/TAT4 ASIC.

the trigger threshold is exceeded the slow-shaped signal is held by peak-hold circuitry until it read out by the motherboard.

The GMI MOCA board acts as the motherboard for up to nine ASIC-detector modules. Shown in Figure 2.4, the left-side (front-end) houses the detectors, while the right-side (back-end) has the ADCs responsible for readout, the connectors responsible for interfacing with the computer, the power-regulation transistors, and the field gate programmable array (FPGA) to control operation. Together with the ASICs and detectors, these pieces of hardware form the backbone of Polaris systems.

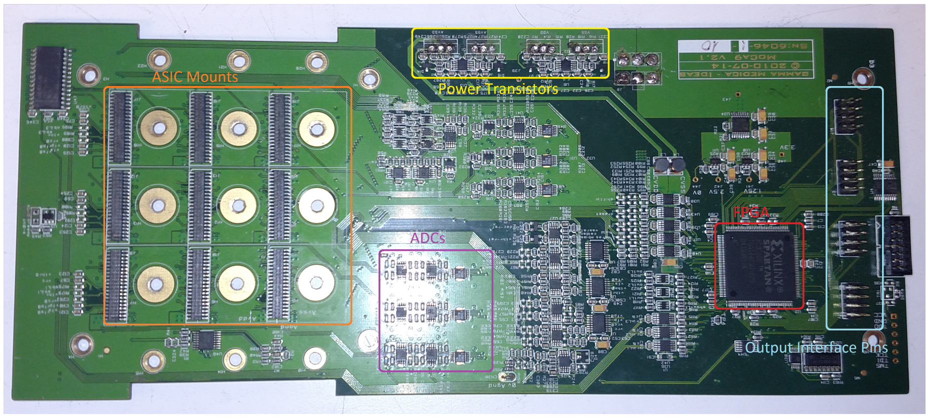

Figure 2.4: MOCA board photograph with overlaid labels.

2.1.2 Systems

The precursor to Polaris systems is the test box. It consists of a single MOCA board in aluminum housing. Electronically it can operate nine detectors, however the design has minimal cooling and can only maintain standard operating temperature with two. This system is used for new detector testing and for research on detectors or ASICs beyond the standard operating parameters.

Two nearly identical detector systems, named Polaris I and Polaris II, were finished in 2010 and 2011, respectively. These systems have 18 detectors on two counter-opposed MOCA boards operating in coincidence. There is a dedicated active cooling system with a large heatsink between the boards, passing through heat pipes and ending with a thermoelectric cooler (TEC) and fan at the top of the system. Fans also dissipate heat from the power-regulation transistors and the MOCA FPGAs. Shown in Figure 2.5, Polaris II is the system quoted with the 0.96% single-pixel resolution and the excellent efficiency afforded by 108 cm^3 of CZT.

In 2015, the final Polaris system with analog GMI ASICs was completed. The separable planes system, Polaris SP, mechanically separates the two MOCA boards so they can operating in coincidence with arbitrary geometry. Shown in Figure 2.6, it duplicates the cooling systems of the other Polaris designs across two planes, offering greater flexibility at the cost of increased power consumption.

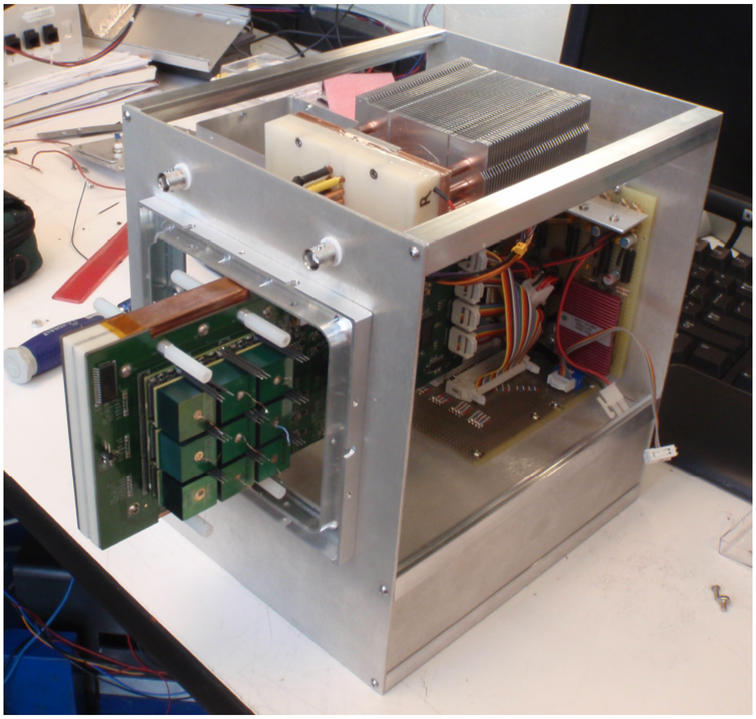

Figure 2.5: Polaris II opened for visibility and populated with 18 detectors.

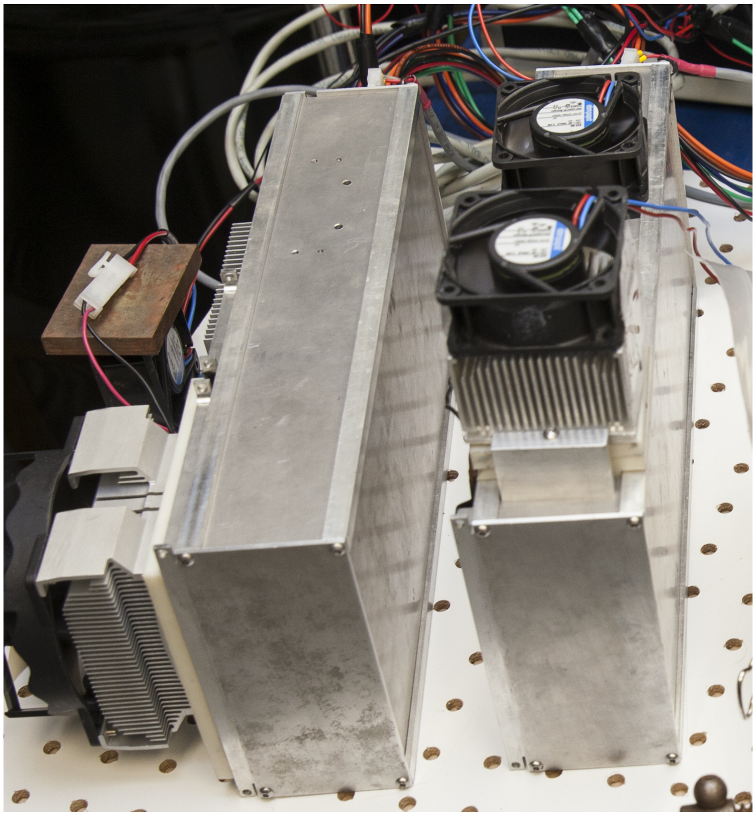

Figure 2.6: Both planes of Polaris SP.

2.2 Calibration

Detector fabrication obviously impacts operational performance, but the link between them cannot be quantified without first understanding the mechanics of detector calibration and operation. At its simplest, whenever a gamma-ray energy deposition occurs, a timing and amplitude signal are read out from every electrode involved in the interaction. There are two modes of operation: sparse and full readout. In sparse readout mode, only the signals from the cathode and the anode electrode(s) under which the interaction occurred are recorded; the signals from all other electrodes are discarded. Conversely, the GMI analog ASIC operates in full readout mode, where the signals from every electrode are recorded. The raw collecting anode signal is then compared with the raw cathode signal to determine the physics of the interaction.

This simplified model of event recording is complicated by several factors. Electronic noise on the preamps and transient signal induction on non-collecting anodes necessitate trigger thresholds, determined during the baseline and noise correction. Slight differences in preamp gain require a pixel correction and electric field non-uniformity requires a depth correction. Both are also affected by material non-uniformity, and are addressed during the amplitude signal calibration. For gamma rays that interact multiple times and trigger multiple anodes, the cathode/anode ratio is unsuitable for determining the interaction depth so the drift time is used. Because the timing circuit is non-instantaneous and the trigger threshold is constant, there is minor time-amplitude walk that must be corrected. Additionally the induced electric charge is not a perfectly linear function of the energy deposited and must be corrected via an additional calibration. Finally, the peak hold circuitry that maintains the signal between collection and readout isn't lossless, so the loss must be corrected.

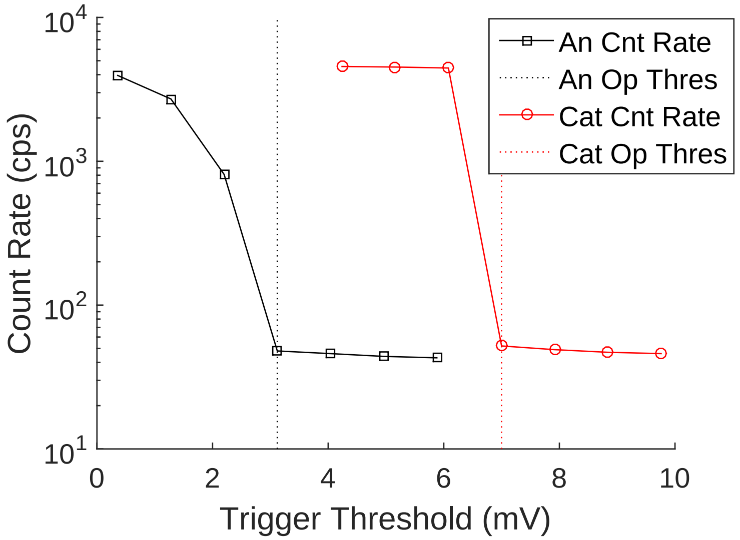

Figure 2.7: Count rate as a function of trigger threshold, used to determine minimum operating trigger threshold.

2.2.1 Baseline and Noise

The first determination for operation is the minimum energy threshold. One threshold is used for all anodes, and another is used for the cathode. They are calculated by biasing a detector, disabling triggering from the other electrode, and reducing the threshold until the event rate increases from the low background event rate to near system saturation, indicating that noise rather than radiation interactions are causing the triggering. This is shown for a sample module in Figure 2.7. The threshold is then set to the smallest value before the event rate spike.

An event-by-event correction is also necessary to filter out noise spikes and small transient signals from charge induced on anodes adjacent to the collecting anode. The baseline for each anode is the average recorded preamp value with zero charge collection, and deviations from this baseline are the noise. Found by recording the output value for all anodes that aren't triggered and aren't adjacent to a triggered anode, the baseline is recalculated every time the MOCA buffer dumps to the DAQ PC, approximately once every 1000 events. By setting a software threshold as a function of noise, false triggers can be filtered out after triggering the hardware threshold

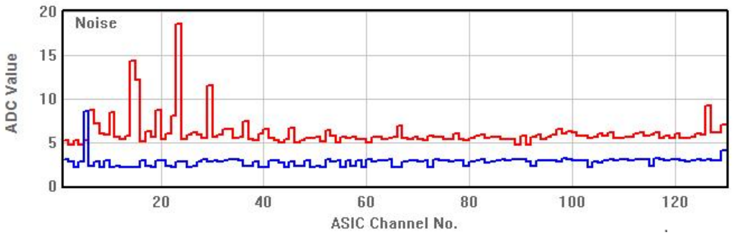

Figure 2.8: 4R-212 average noise in each channel for amplitude signal (red) and timing signal (blue) in a single buffer dump.

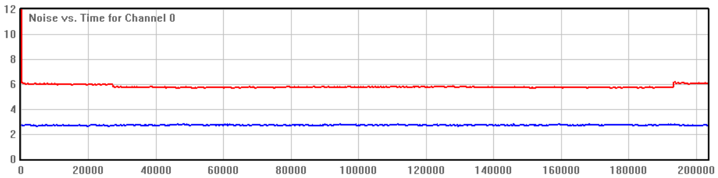

Figure 2.9: 4R-212 noise averaged across all channels as a function of time for amplitude signal (red) and timing signal (blue).

but before recording. This threshold is typically set to 3 standard deviations above the anode noise. The timing and amplitude noises are shown by channel for a single buffer dump in Figure 2.8. Ideally the baseline remains constant in time. Provided other operating parameters remain constant, this is a good assumption, as shown in Figure 2.9.

Finally, the baseline calculation allows for the reduction of common-mode noise, where the noise is correlated between pixels. In the event of common-mode noise, the baseline value for a single event will differ slightly from the average baseline. By shifting the recorded value on the collecting anode by the average of the baseline difference, correlated noise is corrected for.

2.2.2 Amplitude Signal

At it's most basic, an amplitude calibration correlates electrode amplitude signals from the preamp to the deposited energy. This is accomplished by recording gamma-ray interactions from a source with known energy and setting the ADC value of the energy spectrum photopeak centroid equal to the source energy. Assuming energy

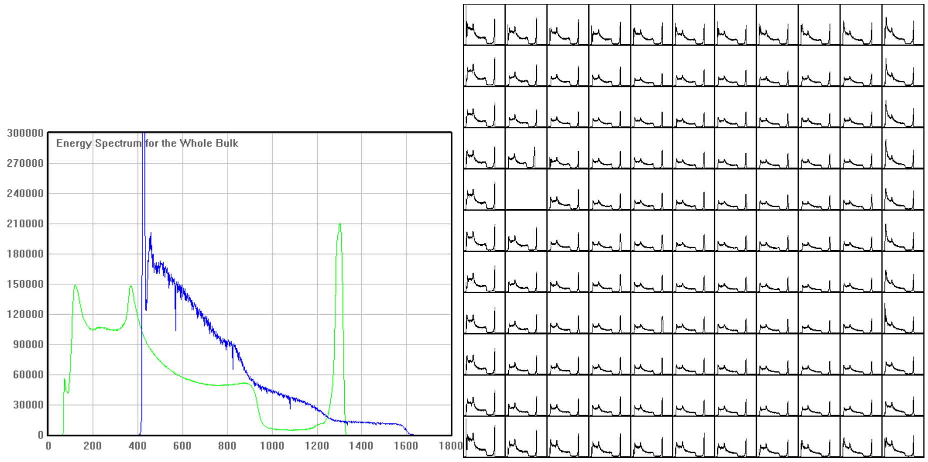

(a) (b)

Figure 2.10: 4R-212 raw overall amplitude spectra (a) for anode (green) and cathode (blue), and raw anode spectra for each anode channel (b).

linearity, zero energy is set equal to zero electrode signal, and the correlation is fully defined. For the Polaris system, Cs-137 is used because it's monoenergetic with a gamma-ray energy 661.7 keV well within the system dynamic range (30 keV to 3000 keV) that penetrates the entire detector depth with small attenuation and ensures irradiation throughout the entire depth. To correct for slight differences in preamplifier gain, this calibration is performed separately for the cathode and for each anode channel, as shown in Figure 2.10. Each recorded spectrum resembles a classic energy spectrum convolved with the weighting potential for the corresponding electrode. The anode signal is largely depth-independent, thus the anode spectra look normal, but the cathode signal decreases linearly with depth, thus the cathode spectrum monotonically decreases.

Taking advantage of SRT, the depth of each interaction is determined by the CAR. By plotting the raw photopeak centroid against the depth for each pixel and fitting a curve to it, an amplitude calibration is independently generated for each voxel in the detector. The overall depth separation and the photopeak depth fitting are shown in Figure 2.11. The raw anode amplitude centroid is low for depths near

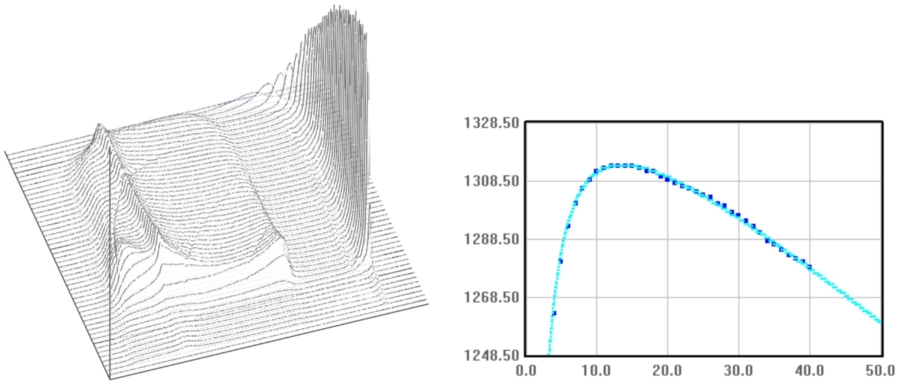

(a) (b)

Figure 2.11: 4R-212 raw depth-separated overall amplitude spectra (a) and channel 7 raw anode amplitude centroids (b) with binned values in dark blue and fitted curve in light blue.

the anode due to the rapid change in the anode weighting potential in this region, peaks a short distance from the anode, and decreases slowly approaching the cathode due to electron trapping.

2.2.3 Drift Time

The amplitude calibration as previously described can only correct single-pixel events, where the incident gamma ray only interacts once within the detector. With multi-pixel events, the cathode signal is the sum of each deposition, so the CAR cannot be used. Instead the drift time, although less accurate[64], must be used. Due to the depth-dependence of the cathode weighting potential, charge is induced on the cathode as soon as electron drift begins, thus the cathode timing spectrum has a narrow, depth-independent spectrum. The centroid of this narrow spectrum is taken as the fixed readout trigger time. Anode timing doesn't begin until the weighting potential spikes very near anode, thus the anode timing spectrum is a wide distribution that varies with depth. By plotting the anode drift time against the CAR depth of interaction for single-pixel events, a one-to-one correlation between drift time and interaction depth is determined and subsequently used to calculate the

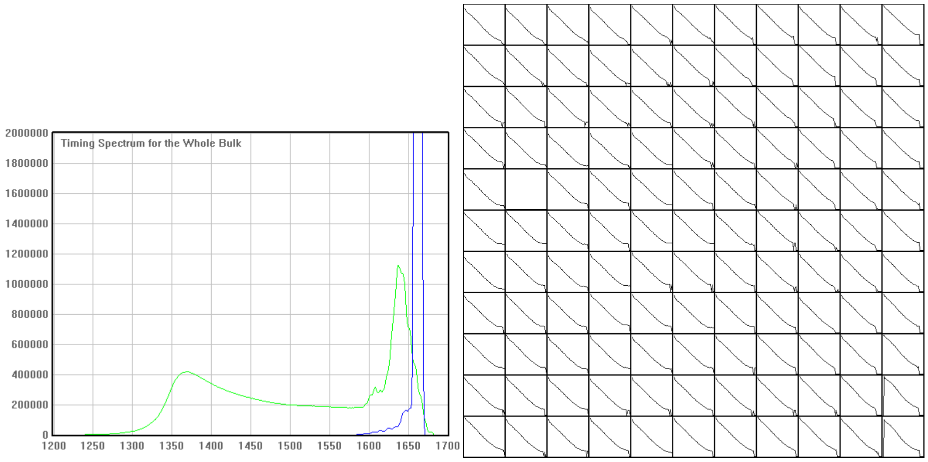

(a) (b)

Figure 2.12: 4R-212 overall drift time spectra (a) for anodes (green) and cathode (blue), and anode drift time centroid as a function of CAR depth for each channel (b).

depth at which each event occurs in multi-pixel interactions. The overall drift time spectra and depth-separated anode drift time centroids are shown in Figure 2.12

For ease of hardware design, drift time is recorded as the time between ASIC trigger and system readout, thus a larger value for drift time indicates an earlier trigger. Additionally, because charge induction on the cathode is immediate, the cathode timing is almost always greater than the anode timing and represents the start of event timing. Events with a greater anode timing occur very near the anode in the region of rapid weighting potential change, where induction is immediate on both electrodes, but the greater slope of the anode weighting potential means it exceeds the trigger threshold first.

2.2.4 Time Amplitude Walk

The simple threshold trigger used by all electrodes in the GMI analog ASIC results in time-amplitude walk. This phenomenon, illustrated for a simulated waveform in Figure 2.13, delays the trigger time as a nonlinear function of deposition energy. Despite having the same physical drift time, a lower energy deposition will consequently

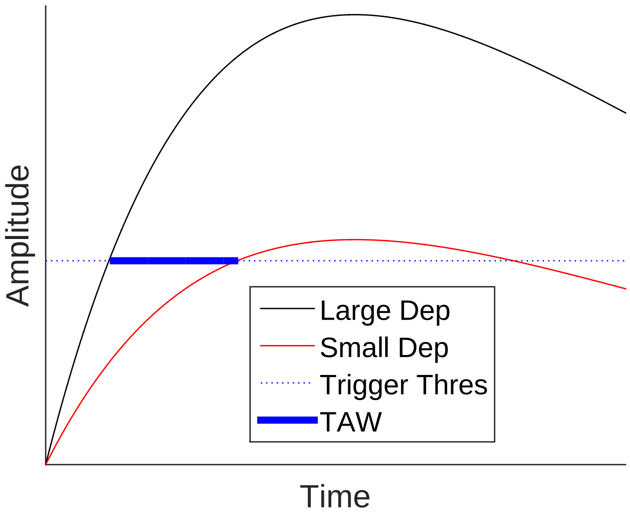

Figure 2.13: Illustration of time-amplitude walk for two simulated incident events occurring in the same location and differing in energy by a factor of two.

have a shorter recorded drift time. Because it occurs in all electrodes, the cathode and anode signals must be corrected independently.

Using two-pixel photopeak events, the total energy deposition is constant and therefore the cathode TAW is constant. The energy deposition on individual anodes varies from the minimum to nearly the full deposition. By coarsely binning the interactions individually by amplitude, a timing spectrum is generated for each bin with the minimum timing value (maximum drift time) representing cathode side events. The difference between the minimum timing for full and partial energy deposition is the anode TAW, thus it is corrected by adding this value to raw timing measurements. Practically, this is accomplished for any energy deposition by fitting a curve to the minimum timing as a function of amplitude.

The cathode TAW is corrected using single-pixel events in conjuction with the anode TAW correction. Considering only events near the cathode, drift time is fixed and the timing spectrum has a peak. Again coarsely binning the events by amplitude, after correcting the previously determined anode TAW, residual movement in the timing peaks for each bin are caused by cathode TAW and are corrected the same

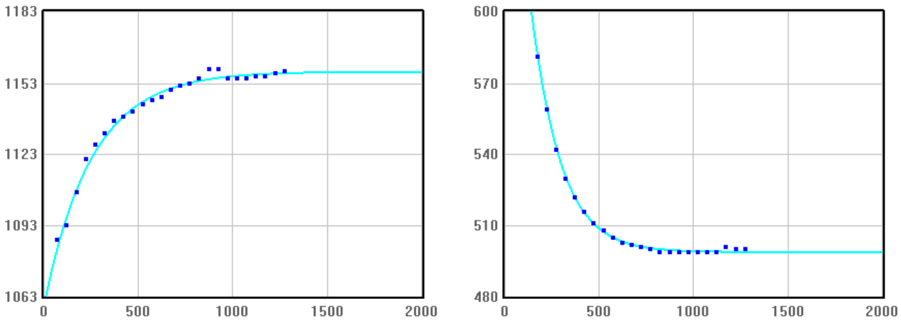

(a) (b)

Figure 2.14: 4R-212 anode minimum timing values as a function of amplitude (a) and anode TAW corrected cathode timing centroids as a function of amplitude (b) with values shown in dark blue and the fitted curve shown in light blue.

way. This is again implemented for all energy depositions by fitting a curve to the timing peaks as a function of amplitude, and is shown for both the anode and cathode TAW correction in Figure 2.14

2.2.5 Energy Nonlinearity

Corrections thus far have assumed a linear relationship between energy deposition and signal amplitude. There is known nonlinearity, however, that degrades the resolution for energy depositions far from the calibration energy. Furthermore, because nonlinearity primarily occurs in the preamps[65], it is dependent on each energy deposition and results in resolution degradation for multi-pixel events even if the total deposition is near the calibration energy.

To correct for nonlinearity, calibrations are taken using several lab sources summarized in Table 2.1 with gamma-ray energies spanning the dynamic range of the ASIC. For each gamma-ray energy, the nonlinearity is the difference between the known photopeak energy and the recorded photopeak centroid for single-pixel interactions using just the Cs-137 calibration. Plotting the difference as a function of recorded energy and fitting a fifth-degree polynomial yields a nonlinearity correction for any energy deposition.

Table 2.1: Nonlinearity Sources and Energies

Source	Energy (keV)	Intensity (%)
Cs-137	661.7	100.0
Ba-133	81.0	34.1
	276.4	7.2
	302.9	18.3
	356.0	62.1
	383.9	8.9
Na-22	511.0	100.0
	1274.5	99.9
Co-57	122.1	85.6
	136.5	10.7
Am-241	59.5	35.9
Co-60	1173.2	100.0
	1332.5	100.0
Na-24	1368.6	100.0
	2754.0	99.9

The nonlinearity calibrations are performed separately for each pixel but not for each depth, both practically to limit data collection time and necessarily because lower energy gamma-rays cannot penetrate the entire detector depth. This is valid because nonlinearity is assumed to occur primarily in the preamps, which are not depth dependent, as opposed to in the detector bulk. Finally, due to the low photopeak efficiency and short half-life of Na-24, a single 2754 keV photopeak centroid is used for the entire detector.

For multi-pixel events, cross-talk between the channels degrades the nonlinearity correction, which is applied individually to the energy deposited on each anode. To correct this, a secondary multi-pixel nonlinearity correction is generated by first applying the single-pixel nonlinearity correction to multi-pixel photopeak events at each gamma-ray energy, subtracting the known energy from the recorded energy, and fitting a curve to the difference. This is done for the detector as a whole rather than for each pixel, and is done separately for 2-pixel, 3-pixel, 4-pixel, and 5-or-more-pixel events.

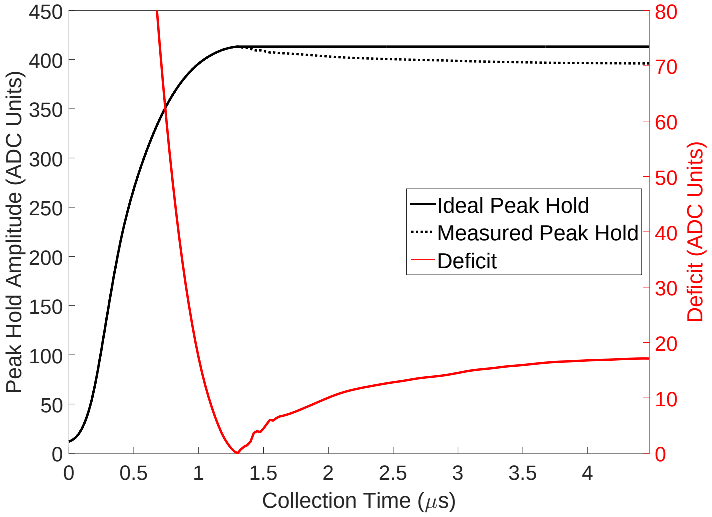

Figure 2.15: Illustration of ideal and realistic peak hold amplitudes, and signal deficit as a function of hold delay time.

2.2.6 Peak Hold Drop

One final consideration during calibration is the ASIC peak-hold circuitry. Ideally, for hold times exceeding the preamp shaping time of 1 μs, the peak hold amplitude would remain constant until read out by the MOCA board. In reality, the amplitude decreases slightly from the peak value as a function of hold time[66]. The drop is most easily visualized as the difference between the maximum peak hold amplitude and the peak hold amplitude for a given hold delay time. This is shown, along with an idealized and realistic peak hold curve, in Figure 2.15. System readout depends on the timing of the incident event, which the system operator cannot control, so the hold time varies and PHD must be corrected for each event.

Because PHD physically occurs after and independently of charge collection, it can be corrected first and independently of other detector calibrations. PHD does, however, vary with preamp amplitude, thus the correction must also be a function of the maximum peak hold amplitude. The correction is determined using the test-pulse injector built into the ASIC. For a fixed test pulse voltage, the injection time is increased in 25 ns increments across the range of possible hold delay times, and

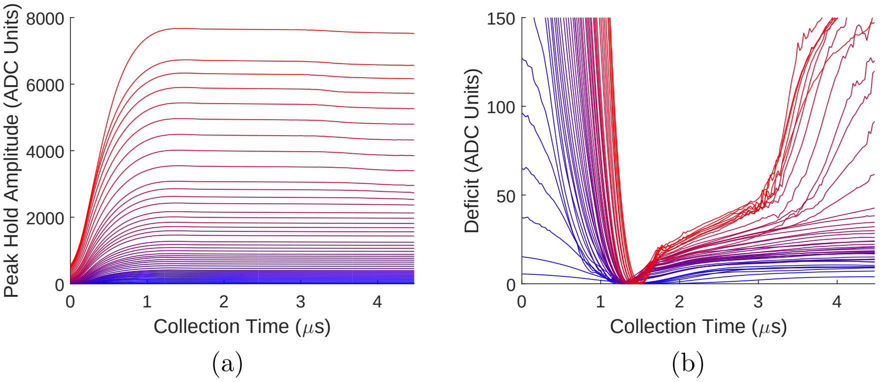

Figure 2.16: Peak hold amplitude (a) and deficit (b) curves used in PHD correction, where the color of the curve is a function of test-pulse injector voltage with blue being the lowest and red being the highest.

the peak hold amplitude is recorded for each. This is repeated across a range of test pulse voltages simulating the dynamic range of the ASIC. The peak hold amplitudes and deficits for the correction of an entire ASIC are shown in Figure 2.16.

The PHD correction is performed during operation by looking up the peak hold time and recorded amplitude of an event, interpolating the deficit between the nearest calibration amplitudes, and adding it back to the recorded amplitude. The peak hold time doesn't require interpolation because 25 ns is the minimum timing resolution of the system. Remembering there is negligible drift time for anode-side events, the amplitude recorded by the timing circuitry for these events during the Cs-137 calibration is the hold delay time. Because the TAC response is linear, the anode cutoff yields the TAC gain, which after baseline subtraction of the timing signal allows the direct conversion between recorded drift time and peak hold time during operation. Although each channel has independent peak hold circuitry, all anode channels have similar performance, so a single PHD correction is used for an entire ASIC.

2.3 Hardware Issues

There are some detector issues that cannot easily be corrected in software or calibrated around[67]. These must instead be fixed at the hardware level. Although the Orion lab contracts out detector fabrication, characterizing the operational effects and understanding the causes of these issues are still crucial for providing meaningful feedback to the vendors.

2.3.1 Gain Deficit

Gain deficit occurs when the gain for one anode channel is significantly lower than the gain in the other anode channels. When this occurs, the raw spectral features are all present in the gain-deficient channel but a lower amplitudes. This is accurately modeled by multiplying a regular channel by a gain less than unity, as shown in Figure 2.17. Gain deficit is corrected during the Cs-137 calibration with only a slight loss in SNR due to decreased amplitude and constant electronic noise. Because gain deficit is read from the raw resolution and convolved with the preamp gain variation across pixels, a minimum threshold of 2%, or 13.2 keV for Cs-137, below the detector average gain needs to be surpassed to identify a gain deficit pixel. It is a common and largely inconsequential problem, occurring in at least 10 pixels for 59 of the 146 Redlen 4R series detectors examined before testing new fabrication techniques.

Gain deficit becomes problematic when it changes over time. This effect, known as gain variation, causes the photopeak centroid in affected pixels to oscillate between two discrete values randomly over time. A pixel map of photopeak position vs. time is shown in Figure 2.18 with pixels experiencing gain variation highlighted. Because the oscillation is non-systematic and not correlated between detectors, it is impossible to know during operation which gain a pixel is operating in, thus gain variation cannot be corrected in software. Ultimately this widens the photopeak or creates a second peak, depending on the severity of the gain deficit.

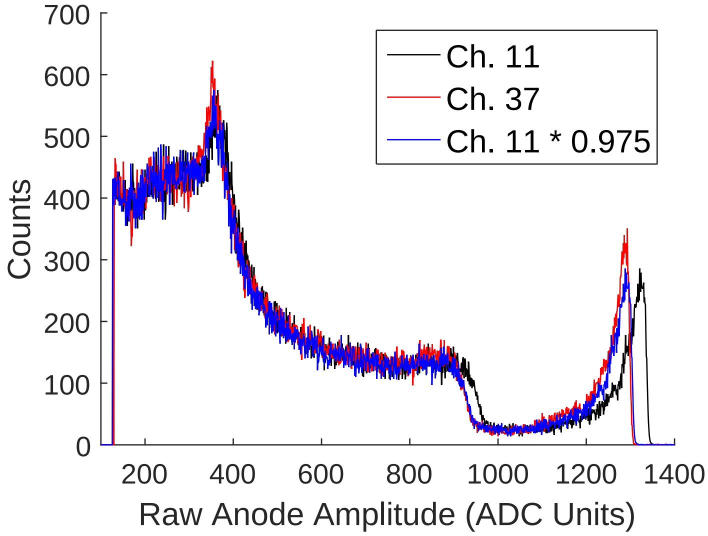

Figure 2.17: 1R-19 raw amplitude spectra for gain deficient, normal, and normal with adjusted gain pixels.

Because gain variation is read from the corrected resolution, magnitudes as low as 2 keV for Cs-137 are discernible in otherwise stable pixels. Between 2 and 5 keV, gain variation is minimal, degrading photopeak resolution no more than 0.75%. From 5 to 10 keV, minor gain variation acts degrades resolution significantly, up to 1.51%. In the range of 10 to 20 keV, moderate gain variation degrades the resolution by up to 3.02%, destroying the spectroscopic performance of the pixel and causing the misidentification of nearby photopeaks. Finally, above 20 keV major gain variation will yield separate Cs-137 photopeaks in the same pixel and frequent misidentification during operation.

Both gain deficit and gain variation are fabrication problems in that they occur on anode surface rather than within the material bulk. This was first hypothesized when no depth dependence of the gain variation effect was observed. It was confirmed by refabricating several detectors which severely experienced both problems and observing a drastic reduction in each. Refabrication here involved removing the carrier board and attaching a new one without physically altering the detector crystal.

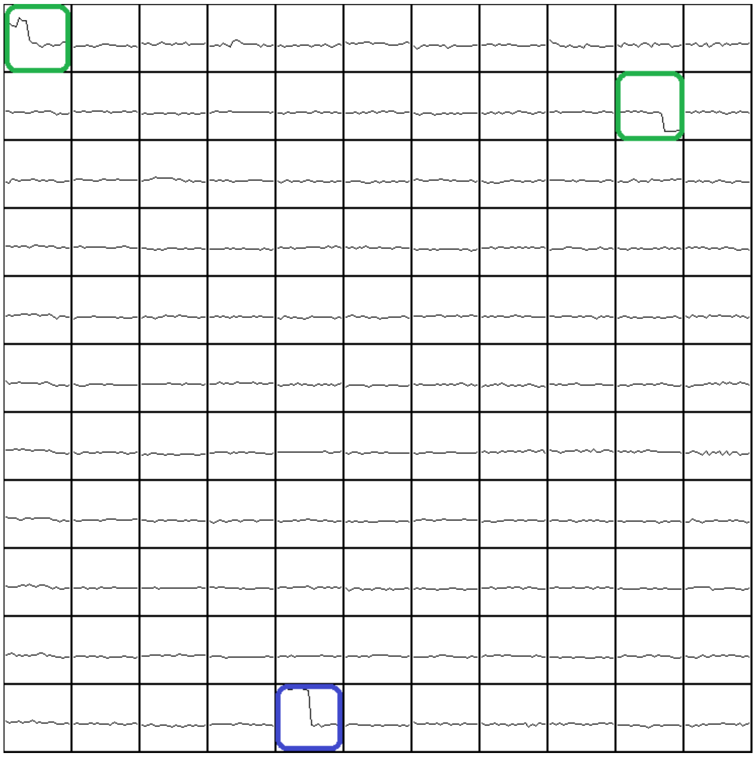

Figure 2.18: 1R-19 pixel map of photopeak centroid vs. time with pixels experiencing minor gain variation highlighted in green and moderate gain variation in blue.

2.3.2 Poor Steering

The steering grid is an electrode between the pixels of 1R, 2R, and 4R series detectors. It is biased typically between -30 and -120 V to guide electrons generated over the gap into an anode. As the magnitude of this bias increases, electrons are repelled harder from gap, but surface leakage between the anodes and the grid increases. Optimizing the grid bias, which must be done independently for each detector, is a balancing act between electron repulsion and leakage current. To compare steering at various grid biases, single interaction events that occur over the grid and are collected by multiple anodes must be examined. Such charge-sharing events trigger two adjacent anodes. Although Compton scatter events that interact with side-neighboring pixels are also possible, they cannot be isolated from charge-sharing events with the analog ASIC. Consequently, the two-pixel side-neighbor resolution is the best approximation of the charge-sharing event resolution and is used as the steering Figure

Figure 2.19: 1R-19 pixel map of two-pixel side neighbor event photopeaks, with a region of excellent steering highlighted in green and a region of poor steering highlighted in red.

of merit.

Because by design a uniform grid bias is used between each anode and the fabrication process cannot be replicated exactly for each anode, some pixels will have better steering performance than others. To some degree this is true of every common-grid detector, but those with very large two-pixel side neighbor resolution or very large fluctuations in this value from pixel to pixel have poor steering. There are several possible causes, such as mechanical nonuniformity in the grid electrode or anode pad position, or excess grid to anode leakage altering the electric field on the detector surface. Figure 2.19 illustrates a region of moderately poor steering in a detector with otherwise good steering.

2.3.3 Noise Triggering

Along with electronic noise generated by the ASIC preamps, the detectors also generate noise. The detector noise generated by each anode channel is typically far less than the analogous ASIC noise, but some pixels are significantly noisier than the average. There are three underlying causes: noise spikes that occur before applying cathode bias result from a virtual short between the noisy anode and the grid or another anode; noise spikes that occur after applying cathode bias but before applying grid bias result from a high leakage current through the bulk or over the side surface of the detector in the region collected by the noisy anode; noise spikes that occur after applying grid bias result from high leakage current between the noisy pixel and the grid.

Because each anode channel by design limitation has the same trigger threshold, there are only two options for operating a detector with noisy pixels. Either the trigger threshold can be set above the noise level of noisiest pixel, or the noisy pixels can be disabled. Raising the trigger threshold raises the minimum recordable energy for all pixels, hurting spectroscopy for low energy gamma rays and multi-pixel events with a small-angle Compton scatter. Disabling pixels reduces the detector efficiency as the material above those pixels is essentially ignored by the system. Bulk and surface resistivity are material properties, thus are determined during crystal growth and fabrication. They can only be observed during calibration and operation.

CHAPTER III

Alternative Fabrication Testing

3.1 Motivation for Fabrication Change

Between October 2012 and April 2013 Redlen fabricated and delivered 50 common-grid detectors, ten detectors each of five varieties, to test new fabrication processes. Because only the anode fabrication was considered, crystal bulk properties were irrelevant and the detectors were all of the small-volume 1R series. The first batch consisted of standard detectors for benchmarking. Detectors in the second batch were attached to a Rogers ceramic substrate instead of the standard PCB material. Detectors in third batch had platinum electrode contacts rather than the standard gold. Finally Redlen developed two proprietary detector fabrication techniques using the standard materials designed A and B that comprised the fourth and fifth batches, respectively.

Generally the goal of fabrication changes is to increase the yield, improve the performance, and reduce the cost of detector production. Specifically this collection of detectors was developed to reduce gain deficit and minimize gain variation. As important secondary concerns, the spectroscopic and imaging performances of detectors with new fabrication techniques needed to match or exceed those of the standard detectors.

Gold is the traditional electrode material because it has a greater work function than CZT but most closely approximates an Ohmic contact[68]. Platinum was selected here to create a Schottky barrier in hopes of reducing leakage current[69]. Rogers ceramic was similarly chosen for its greater resistivity than the original PCB material[70].

3.2 Detector Performance

Binning the gain deficit magnitude of each pixel in 10 keV increments, the histograms shown in Figure 3.1 reveal the frequency and severity of gain deficit pixels for each fabrication type. In terms of reducing the frequency of gain deficit pixels, every new fabrication technique is successful. Where 50% of the standard detectors have gain deficit in ten or more pixels, that value is 0% for ceramic substrate, 33% for platinum electrode, and 10% for both fabrication A and B detectors. The magnitude of gain deficit is also reduced in fabrication A and especially ceramic detectors, but is increased in platinum and fabrication B detectors.

Binned by severity, gain variation is examined analogously and is shown by fabrication type in Figure 3.2. Similarly to gain deficit, fabrication A and especially ceramic detectors show a reduction in both the magnitude and frequency of gain deficit detectors. For fabrication B detectors, the magnitude is reduced at the cost of greater frequency. Detectors with platinum electrodes have gain variation anodes with larger magnitude and with greater frequency.

Because several of the new fabrication techniques alter the resistivity near the grid, it is important to examine the grid leakage current. This leakage partially dictates the optimal grid bias, so both are shown for each fabrication type in Figure 3.3. Every new fabrication type experiences elevated grid leakage with a minor increase in ceramic detectors, a moderate increase in fabrication B detectors, and a major increase in both platinum and fabrication A detectors. Additionally, due to excessively leakage one platinum detector was capped at 14 V grid bias and another was rejected outright.

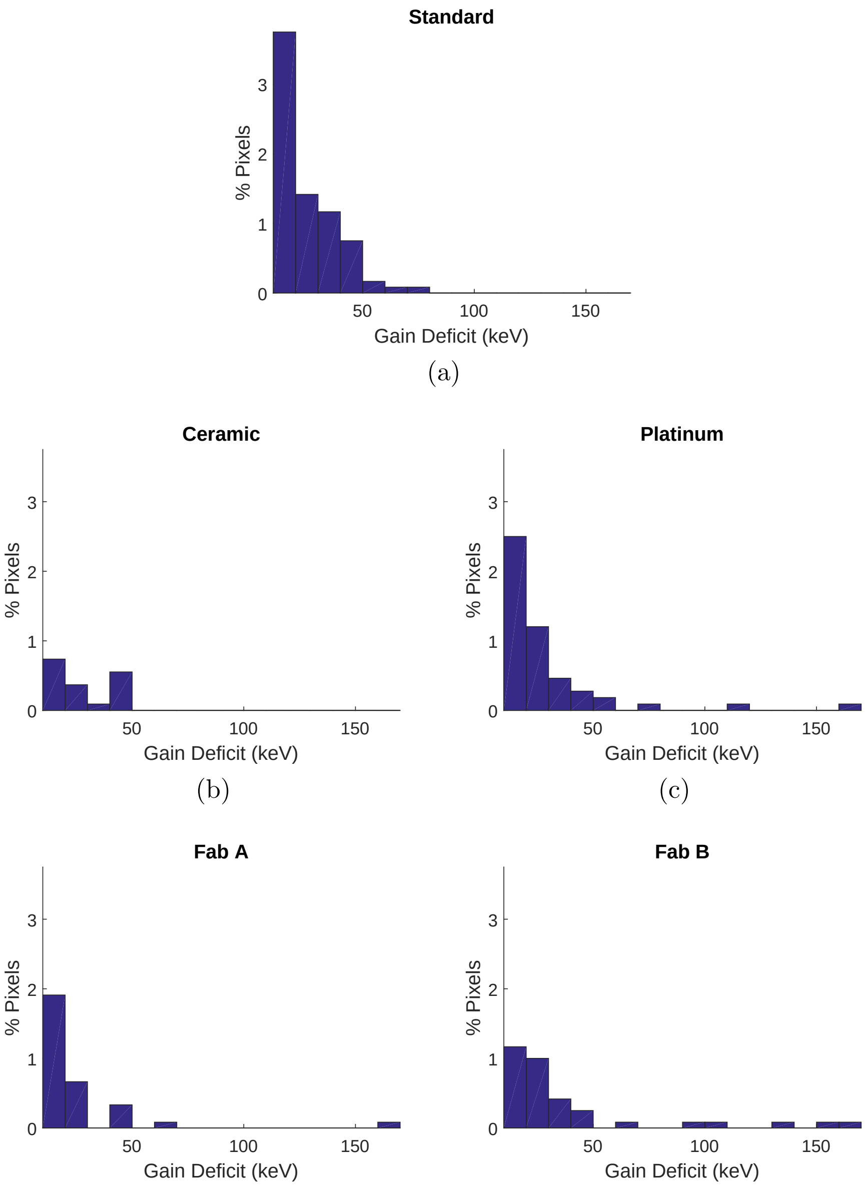

(a)

(b)

(c)

(d)

(e)

Figure 3.1: Histograms showing the frequency and magnitude of gain deficit pixels for standard (a), ceramic (b), platinum (c), fabrication A (d), and fabrication B (e) detectors with fixed axes for ease of comparison. Frequency rather than absolute pixel count is compared to account for pixels disabled due to excessive noise and a rejected detector.

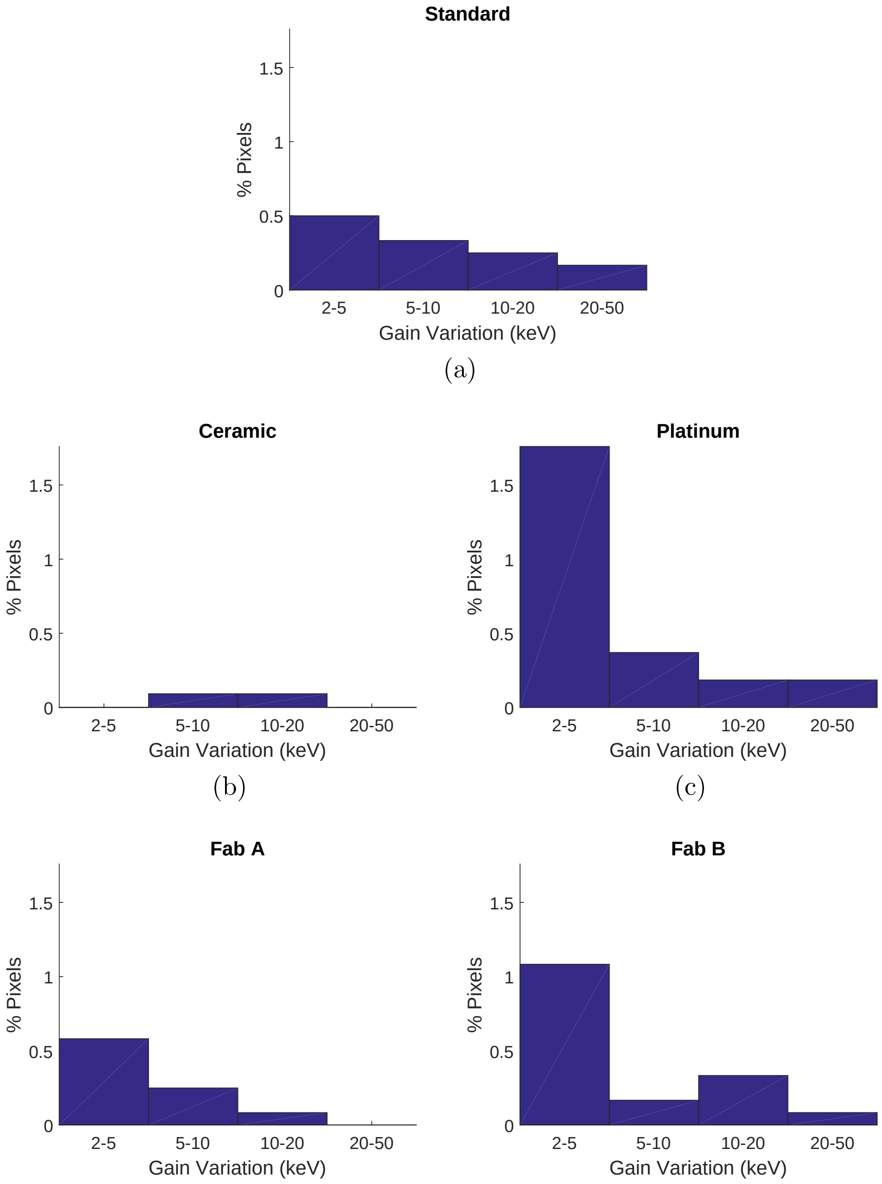

(a)

(b)

(c)

(d)

(e)

Figure 3.2: Histograms showing the frequency and magnitude of gain variation pixels for standard (a), ceramic (b), platinum (c), fabrication A (d), and fabrication B (e) detectors with fixed axes for ease of comparison. Frequency rather than absolute pixel count is compared to account for pixels disabled due to excessive noise and a rejected detector.

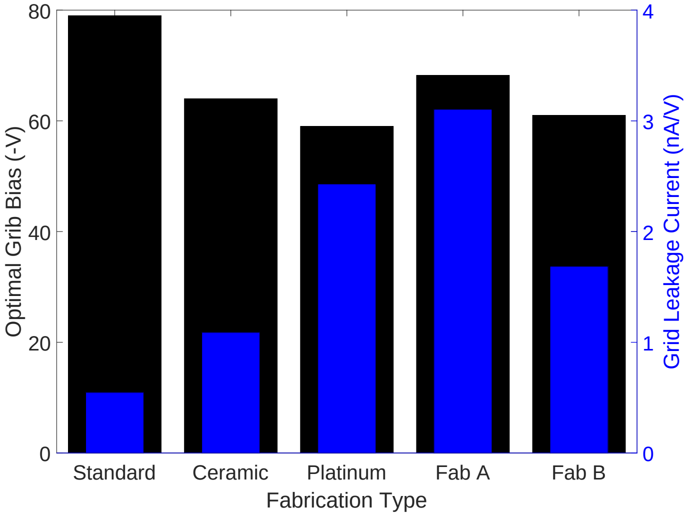

Figure 3.3: Comparison of average OGB and grid leakage current for each new fabrication type.

Both are discarded during performance analysis.

Despite these drastic leakage current differences, each new fabrication technique shows a minor and relatively uniform reduction in optimal grid bias that is only understood in conjunction with steering. Using the corrected two-pixel side-neighbor resolution as the basis for comparison, Figure 3.4 compares the steering for each fabrication type. Because (non-rejected) platinum and fabrication B detectors steer similarly to standard detectors despite greater grid leakage, their grids repel electrons from the gap better. This is doubly true for ceramic detectors, where the steering is improved. Finally, the very poor two-pixel side neighbor resolution of fabrication A detectors indicates they were unable to optimize steering and the resolution at optimal grid bias was largely governed by the high leakage current.

For detectors with identical bulk material operated on identical ASICs, the raw resolution is determined by the leakage current, the charge collection efficiency, and gain deficit. The grid leakage current manifests as noise and widens the photopeak. Partial charge loss to the gap and gain deficit reduce the recorded amplitude, moving events to a low-energy tail region and also widening the photopeak. The raw

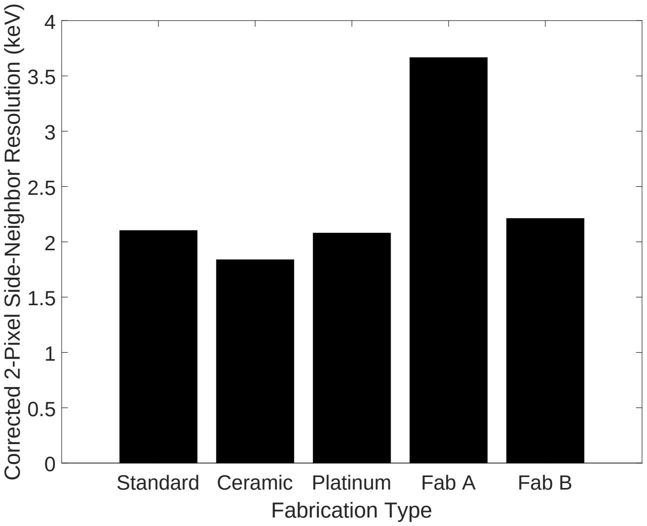

Figure 3.4: Comparison of average two-pixel side-neighbor resolution as steering figure of merit for each fabrication type.

resolution for each fabrication type, shown in Figure 3.5, mirrors the previous results: platinum and fabrication B detectors show slight improvement over standard detectors due to similar steering and reduced frequency of gain deficit pixels; ceramic detectors show significant improvement due to better steering and drastically reduced frequency of gain deficit pixels; fabrication A detectors show slight degradation in spite of reduced gain deficit frequency due to substantially worse steering.

During operation, the most important parameters are the spectroscopic and imaging performances. The best spectroscopy comes from the single-pixel event spectra, and the results are shown for each fabrication type in Figure 3.6. Compared to standard detectors, ceramic substrate detectors show great improvement, platinum electrode detectors show slight improvement, and both fabrication A and B detectors show slight degradation. The imaging results, summarized in Figure 3.7, indicate imaging improvement for sources above the cathode in detectors of all new fabrication types. The side polar and side azimuthal imaging performances show degradation for all new fabrication types, but this is less concerning as side imaging is uniformly poor even among the standard detectors due to small detector thickness.

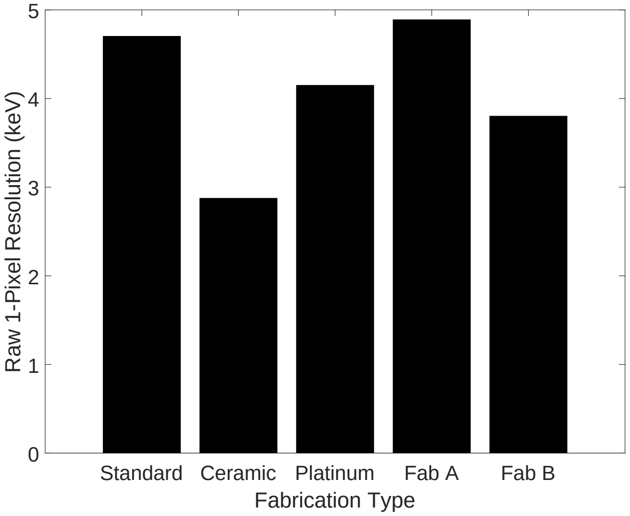

Figure 3.5: Comparison of average raw one-pixel resolution for each new fabrication type.

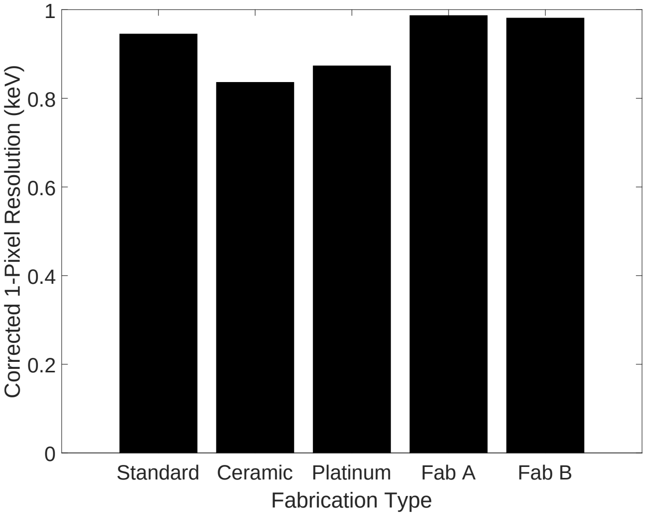

Figure 3.6: Comparison of average corrected one-pixel resolution as spectroscopy figure of merit for each new fabrication type.

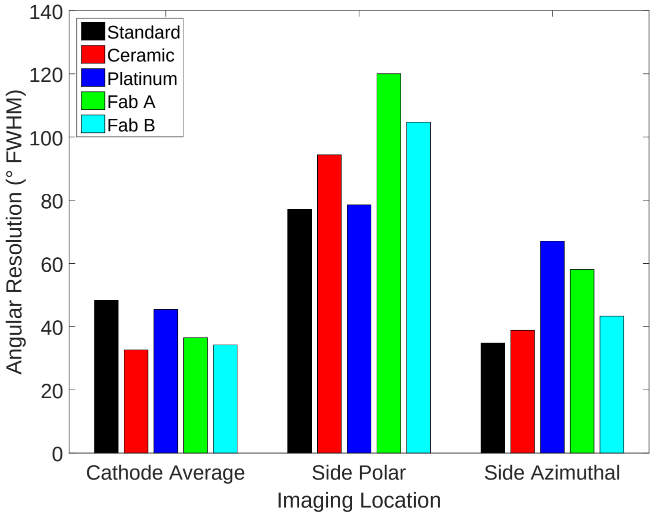

Figure 3.7: Comparison of imaging performance by source location for each new fabrication type.

3.3 Design Impact and Future Work

The results of this analysis shaped the future design of large-volume detectors in the Orion group. Switching from PCB to a ceramic substrate showed unambiguous improvement in every aspect of detector operation. Furthermore it showed the most drastic reduction in frequency and severity of pixels experiencing gain deficit and gain variation. It was therefore adopted as the standard substrate for new detectors. The high leakage current, high rejection rate, and poor gain variation performance of the platinum electrode detectors made it a clear rejection on adopting them for future use. The exceptional leakage of fabrication A detectors deteriorated all aspects of their performance and resulted in rejecting them for future fabrication. The poor gain variation performance and degraded resolution of fabrication B detectors also made them a clear rejection. These results include ten detectors and over 1200 independent anodes for each fabrication type, thus are statistically significant.

Because the use of ceramic substrates has almost entirely mitigated gain deficit and gain variation, they are no longer actively studied. This is theorized to be the result of reduced thermal expansion in the substrate reducing mechanical changes to the detector surface. In the future, it would be beneficial to prove the underlying physical process that caused it, both to feed back to the vendors and to better understand and simulate detectors internally. Additionally gain variation historically was assessed only during initial detector testing despite a known time dependence. Performing a long-term study would help characterize the photopeak movement and could show it has a time dependence, just on a longer scale than previously considered. Finally, because both gain problems have largely been isolated to the substrate material on new detectors, the findings should be confirmed by refabricating old PCB-substrate detectors and retesting.

CHAPTER IV

Early Temperature Work

4.1 Cooling Cost

Although room-temperature operation adds great flexibility to CZT detector systems, it comes with some limitations. Particularly with pixelated anodes, operating the readout electronics is power-intensive and consequently generates heat. This heat must be removed to prevent the detector-ASIC modules from exceeding the room-temperature operating range. For a single crystal, passive radiative cooling is sufficient, and with two or three crystals convective cooling via a PC fan suffices. For larger array systems, active conductive cooling is required. The power requirements for system operation, summarized in Table 4.1, clearly indicate cooling is more expensive than all other components of operation combined for array systems. Historically it has been simpler to regulate system operating temperature than to let it float and account for performance changes. In a current effort to improve system battery life, the power consumption must be reduced. The first step is to isolate the effects of temperature on the ASIC from the effects on the detector in order to improve system performance while reducing the power regulation requirements.

Table 4.1: Power consumption for each component of the Polaris detector systems

Component	Test Box w/ 1 Detector	Polaris I/II	Polaris SP
ASIC Power	500 mW	9.0 W	9.0 W
Detector Bias	<200 μW	<3.6 mW	<3.6 mW
FPGA Power	2.0 W	4.0 W	4.0 W
PC Communication	1.5 W	1.5 W	1.5 W
MOCA Power	3.0 W	9.5 W	9.5 W
Component Power Subtotal	7.0 W	25.0 W	25 W
Fan Cooling	1.8 W	3.7 W	17 W
TEC Cooling	0.0 W	38.4 W	54.6 W
Cooling Subtotal	1.8 W	42.1 W	71.6 W
Total	8.8 W	67.1 W	96.6 W

4.2 Performance Shift with Temperature

The first goal was simply to visualize the effects of temperature over a large range on CdZnTe detectors. This was done by placing a detector system into a Thermotron S-1.2-3200 environmental chamber with a 30 μCi Cs-137 source, calibrating at 15°C, then operating over a range of temperatures and tracking the movement of the ostensibly 661.7 keV photopeak centroid. Throughout three trials the system was populated with two large volume Redlen CdZnTe detectors. To maintain consistent heat generation, the ASICs and their position on the MOCA board were kept constant. Additionally, in each trial the first ASIC was mounted with a common grid detector, and the second was mounted with a simple pixel detector. Each trial involved measurements at 5°C increments from 5-25°C. Each measurement lasted two hours preceded by two hours of unrecorded operation at the designated temperature to allow for system equilibration. Scattering events coincident on both detectors are rare and discarded for simplicity in this and all subsequent experiments involving two detectors.

For the first experiment, the overall photopeak centroid position is compared with the environmental chamber temperature. Shown in Figure 4.1, it clearly demonstrates the photopeak centroid trending upward with temperature. For all trials the photopeak increases monotonically, although not perfectly linearly. The range of centroid movement is systematically greater in common grid detectors than simple pixel detectors. That there is movement at all confirms the linear correction already performed is ineffective. Moreover, because the ASICs are functionally identical, a systematic difference among modules with different types of detectors mounted suggests that the change in the combined module performance is predominantly due to a change in the detector performance.

This experiment also clearly demonstrates that leakage current strongly depends on operating temperature. The results, shown in Figure 4.2, suggest a monotonic increase in leakage as a function of temperature but are limited by the 10 nA minimum resolution of the Ortec 710 quad bias supply used for readout. Additionally, the leakage varies greatly from detector to detector, but is systematically higher in the common-grid detectors than the simple-pixel detectors. This is expected and is a result of the grid electrode. The leakage in common-grid detectors is affected by bulk resistivity changes as a function of temperature as well as slight physical movement of the grid due to thermal expansion, whereas the leakage in simple-pixel detectors is only affected by bulk resistivity changes. The ASICs each have an on-board leakage current compensation circuit, meaning changing leakage current should not affect the photopeak centroid[71].

4.3 Temperature Sensor Linearity

The second purpose was to determine the accuracy of the onboard temperature sensors. The detector system was fortunately designed with two passive temperature sensors that are usable during field operation. A mock-up of their positions on the MOCA board front-end is shown in Figure 4.3. The first is a resistive thermometer located on the motherboard near the ASIC mounts. It is shared by all ASICs and

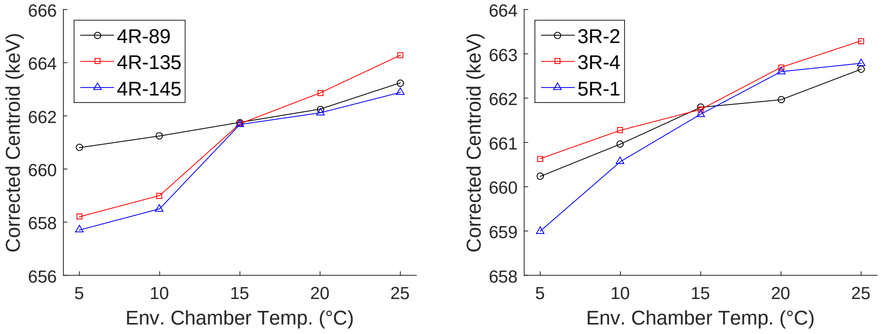

(a) (b)

Figure 4.1: Photopeak centroid as a function of environmental chamber temperature during measurements using a 15°C calibration for common-grid (a) and simple-pixel (b) detectors.

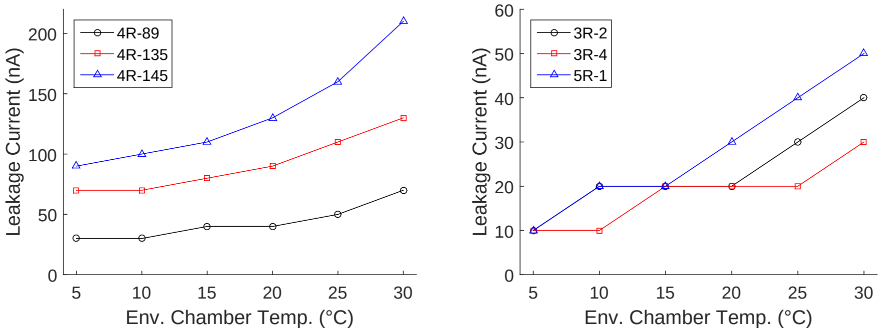

(a) (b)

Figure 4.2: Leakage current as a function of environmental chamber temperature during measurements using a 15°C calibration for common-grid (a) and simple-pixel (b) detectors.

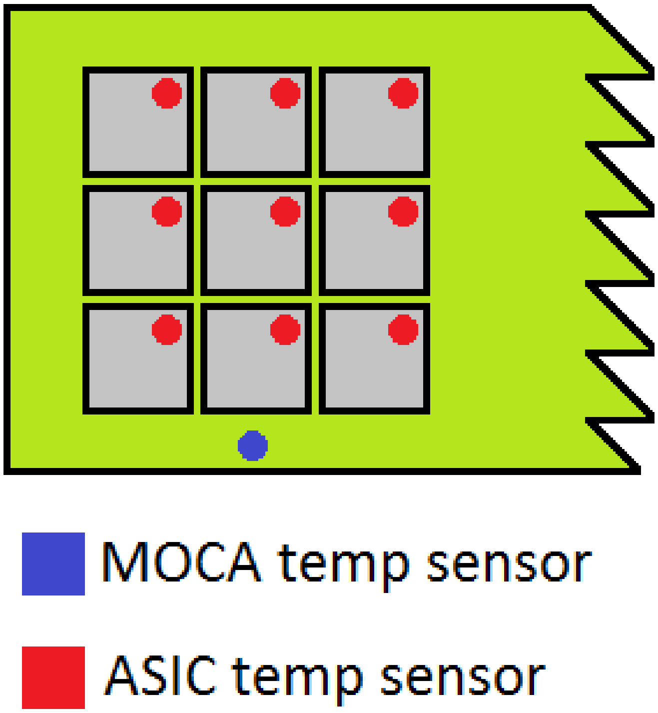

Figure 4.3: Mock-up of temperature sensor position on MOCA board.

the readout is converted directly into °C, but it only reads out once per minute. Each ASIC also measures its baseline, which serves as an indirect temperature measurement. The baseline, calculated by averaging the signal on all pixels that didn't trigger and aren't neighboring a pixel that did trigger, is recorded every time the system buffer writes to the data acquisition computer, typically about once every 1000 events. This has the advantage of measuring the temperature more often, from the ASIC directly, and independently for each ASIC, but has the disadvantage of being recorded in analog-to-digital converter (ADC) units, which cannot be directly converted into units of temperature. A unique measurement for each ASIC is important because SolidWorks heat-flow modeling shows a temperature gradient across the detectors, as shown in Figure 4.4.

The environmental chamber temperature served as the basis for comparison because it is the most direct and easily controlled, but is completely uninformative dur-

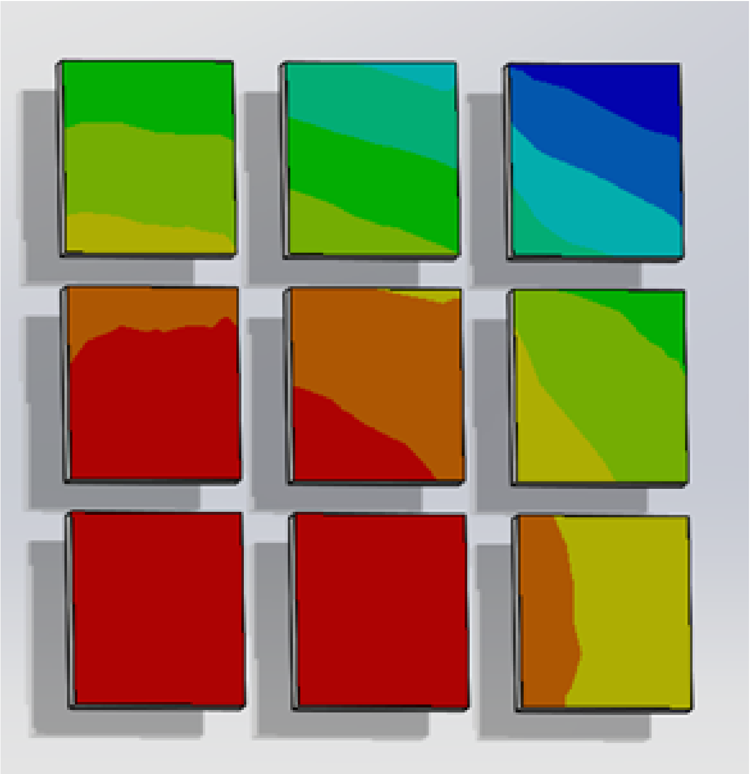

Figure 4.4: Simulated temperature gradient across cathode faces of detectors operating in Polaris configuration with range of 1°C.

ing field operation when the system must operate outside the chamber's temperature-controlled interior. The induced airflow and confined space within the environmental chamber make even comparing the manually set temperature within to measured room temperature outside of it only an indirect comparison of the detector temperature.

The recorded values from each temperature sensor gathered during the photopeak centroid measurement were averaged over the measurement duration and compared with temperature set on the environmental chamber. The raw values and linear fits are shown in Figure 4.5. The small uncertainty and R^2 values very near unity signify excellent proportionality between the three temperature measurements. Because there is a strong correlation between the three temperature measurements, they can be used interchangeably without introducing significant error.

The motherboard temperature is always 4-5°C higher than the environmental chamber temperature because the thermometer is near the heat-generating ASICs, thus equilibrates at a higher-than-ambient temperature. Additionally, because the linear trends for each ASIC are different and the actual temperature of the ASICs must be higher than the motherboard thermometer, these trends provide insufficient data to directly convert baseline measurements to units of temperature.

The ASIC mounted to the simple-pixel detectors covers a greater range of baseline values over the temperature domain despite greater leakage current in the common-grid detectors. This suggests that the baseline is dominated by electronic noise in the ASIC. Furthermore, while this experiment was repeated for each detector, it is only shown once for each ASIC because the differences are visually indistinguishable. This confirms that the leakage compensation is effective and baseline variation with temperature is almost entirely a result of electronic noise.

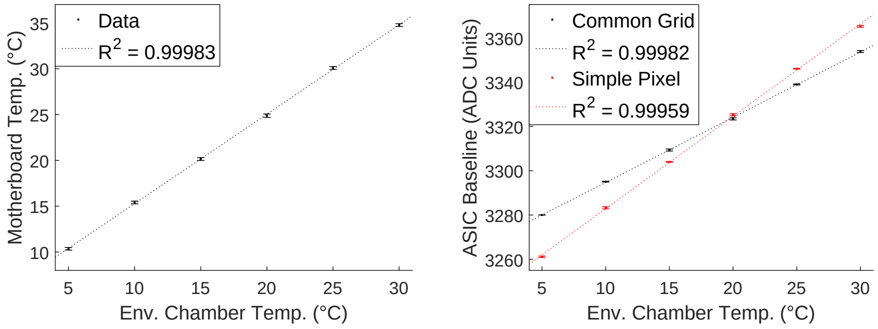

(a) (b)

Figure 4.5: Environmental chamber to temperature sensor reading correlation for motherboard thermometer (a) and ASIC baseline measurements (b) with error bars being twice the standard deviation of the averaged temperature sensor readings from each measurement.

4.4 Temperature Shift Isolation

The final objective was to isolate the primary cause of system performance change with temperature to either the detector or ASIC. Because data cannot be collected from a bare detector, the isolated temperature effects were found by collecting data from the combined ASIC-detector modules, then from the bare ASICs, and using the results to mathematically determine the detector response. With the modules mounted, each trial began with a five hour equilibration period at 5°C before data collection, followed by a temperature ramp from 5°C to 25°C with a Cs-137 source. The first measurement lasted 10 hours with discreet 1°C temperature increases every half hour, while the following two lasted 20 hours with a continuous temperature increase of 1°C/hour.

4.4.1 Experimental Design

A test pulse injection circuit was used to find the bare ASIC response. Shown schematically in Figure 4.6, it used a BNC BH1 NIM pulser external to the environmental chamber to generate pulses at 100 Hz. The pulse was brought into the

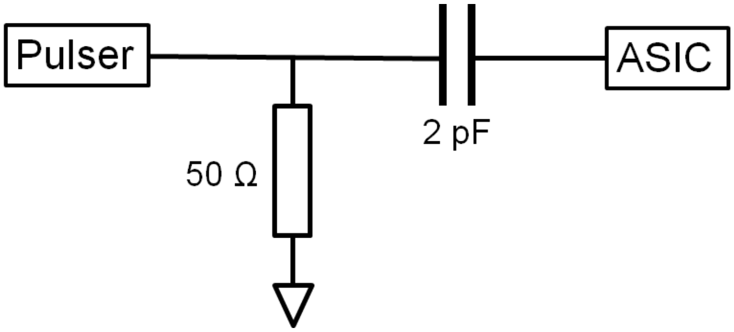

Figure 4.6: Test pulse injection circuit schematic.

environmental chamber via a well-insulated coaxial cable, injected through a high pass filter with an extremely temperature-stable capacitor[72], and terminated in a single channel for the ASIC. Each trial involved a pulse injector into each ASIC, and the experiment was repeated for the three different arbitrarily chosen channels highlighted in Fig. 4.7. All measurements with the bare ASIC lasted 20 hours with a continuous temperature increase of 1°C/hour following one hour of unrecorded operation at 5°C for temperature equilibration. The test pulse magnitude was chosen to produce Cs-137 energy events at room temperature.

To calculate the detector temperature response f_{Det} from the known combined response f_{comb} and ASIC response f_{ASIC}, the ASIC response is treated as a simple gain on the detector response, shown in Equation (4.1).

$$f_{comb}(B) = f_{Det}(B) f_{ASIC}(B) \tag{4.1}$$

Where B is the baseline. Using this formulation, the combined and ASIC responses are expressed in units of energy because they are calculated directly from measured data, while the detector response is a unitless correction because it is derived. In reality, the measured responses are in arbitrary ASIC ADC units scaled to Cs-137 energy E_{Cs} during calibration. To facilitate comparison, a newly defined calibrated isolated detector response F_{Det} is similarly scaled, shown in Equation (4.2).

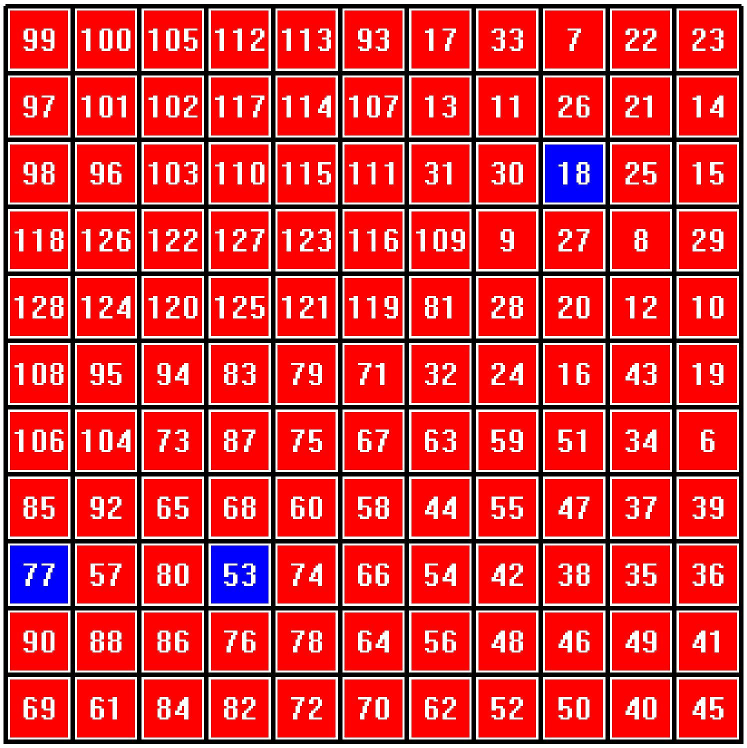

99	100	105	112	113	93	17	33	7	22	23
97	101	102	117	114	107	13	11	26	21	14
98	96	103	110	115	111	31	30	18	25	15
118	126	122	127	123	116	109	9	27	8	29
128	124	120	125	121	119	81	28	20	12	10
108	95	94	83	79	71	32	24	16	43	19
106	104	73	87	75	67	63	59	51	34	6
85	92	65	68	60	58	44	55	47	37	39
77	57	80	53	74	66	54	42	38	35	36
90	88	86	76	78	64	56	48	46	49	41
69	61	84	82	72	70	62	52	50	40	45

Figure 4.7: ASIC channel position map with channels used for test pulse injection in blue.

$$F_{Det}(B) = E_{Cs}\frac{f_{comb}(B)}{f_{ASIC}(B)} \tag{4.2}$$

4.4.2 Combined Results

The combined centroid for each trial of the ramp measurement processed with the 15°C calibration data, given by Figure 4.8, shows a clear upward trend in photopeak centroid as temperature increases. Similar to the centroid movement in the discrete temperature measurements, this movement is not perfectly linear, as indicated by the imperfect fit of the linear trend lines. The trend is, however, once again monotonically increasing, and the common-grid detectors shift over a larger range than the simple pixel detectors. Slight variations from the trend in individual data points are caused by the inherent uncertainty in calculating the geometric centroid from discretized data and exacerbated by the limited counts used for each data point.

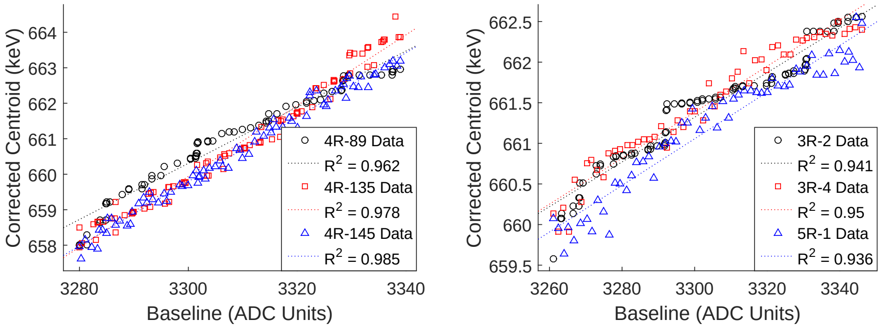

(a) (b)

Figure 4.8: Centroid shift with temperature for ramp measurement and linear fit of combined ASIC-detector modules for common grid (a) and simple pixel (b) detectors.

These centroid shifts represent the performance of all pixels in the detector. By looking at the specific pixels for which the ASIC responses are isolated, shown in Figure 4.10, it is clear that all of the anodes follow the same trend. Because each pixel has less than 1% the number of counts of the detector overall, the anode data must be downsampled to have sufficient statistics for the centroid calculation. Despite inferior statistics, an understanding of the system and a qualitative examination of the patterns in the data can shed light onto the cause of the centroid shift with temperature.

These centroid shifts represent the performance of all pixels in the detector. It is also informative to look at the combined response for the specific pixels in which the ASIC responses are isolated. Illustrated as a cartoon in Figure 4.9, there are several patterns that can qualitatively shed light onto the cause of the centroid shift with temperature.

If the anode shift remains roughly constant in each channel for a given detector, but varies by detector as shown in Figure 4.9b, that indicates a detector component shared by all channels is most susceptible to temperature change. The only components that fit this description are the cathode and the detector material bulk. Conversely, if the anode shift varies by channel but the same channel in each detector

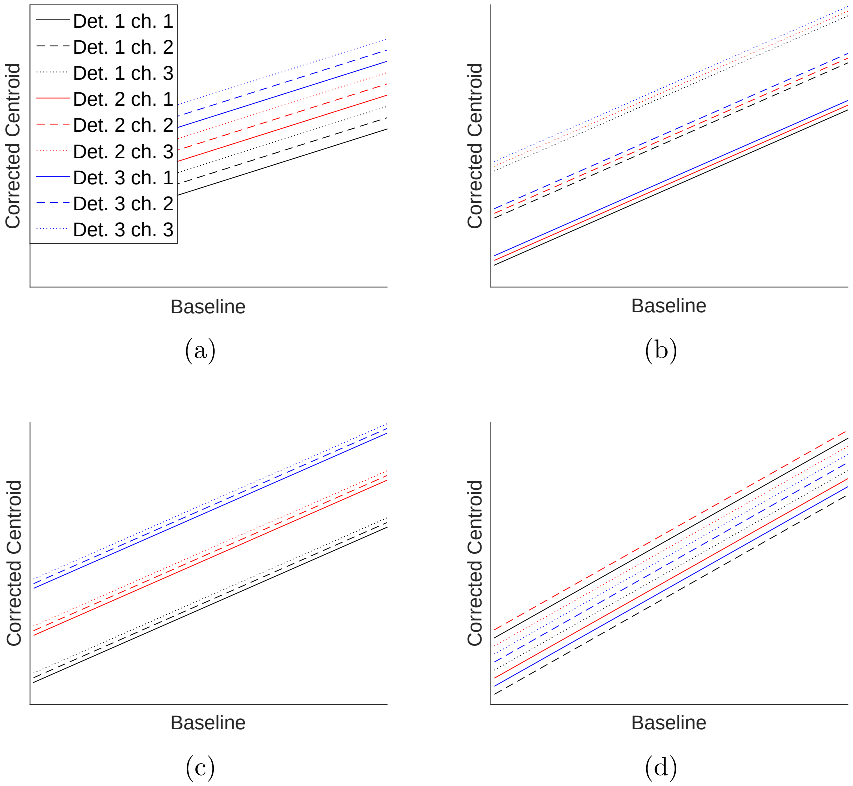

Figure 4.9: Illustration of centroid shift patterns of individual channels in combined ASIC-detector measurement indicative of certain hardware causes for performance change as a function of temperature. The centroid shift can be systematic by detector and ASIC channel (a), only by detector (b), only by ASIC channel (c), or entirely non-systematic (d).

is roughly the same as shown in Figure 4.9c, then some channel-specific component must be most vulnerable to temperature change. Furthermore, because there is no correlation in performance by channel between detectors, because the ASICs were kept constant throughout the experiment, and because each ASIC channel has a separate preamp, this would point directly to the preamps changing with temperature. A pattern in both channels and the detector, shown in Figure 4.9a indicates temperature dependence of hardware systems. No pattern in the anode trends as a function of detector or channel, shown in Figure 4.9d, indicates that the temperature shift comes predominantly from a channel-specific component of the detectors.

The measured anode temperature responses are shown in Figure 4.10. The cen-

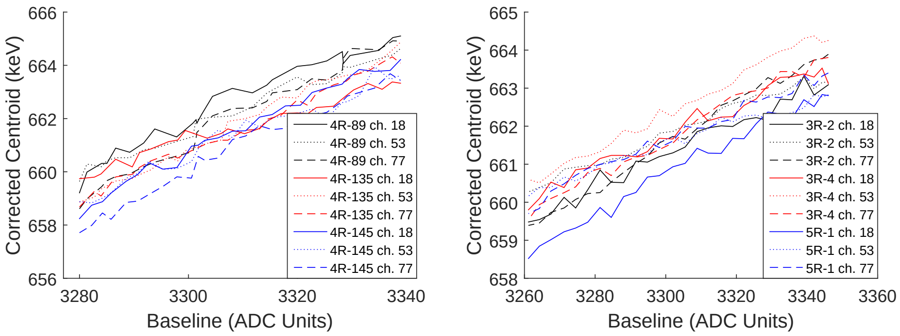

(a) (b)

Figure 4.10: Centroid shift with temperature of combined ASIC-detector modules for common grid (a) and simple pixel (b) detectors for only anodes examined in isolated ASIC measurement.

troid trends for each anode channel all follow the same monotonic increase with temperature found in the combined response, although there are no visually apparent patterns by detector or channel. This observation matches the illustration in Figure 4.9d and suggests the temperature shift is primarily caused by channel-specific components of the detector. The larger variations in individual data points from the trend are a result of fewer counts per data point compared with the overall measurement.

4.4.3 Isolated Results

The isolated ASIC shifts, shown in 4.11 cover a much narrower range of photopeak centroids over the same temperature range. This drastically reduced range makes the granularity of the data imposed by the two decimal place recording on the photopeak visible. The data here are clearly nonlinear and are best fit by a quadratic trend. The results for each channel and in both ASICs are very similar, suggesting excellent uniformity in each preamp.

Each channel-specific combined anode trend is made from downsampled data because each channel receives less than 1% the total number of counts. To mitigate the poorer counting statistics of these trends, the averaged channel responses for each isolated ASIC are used to determine the detector response. This is valid because

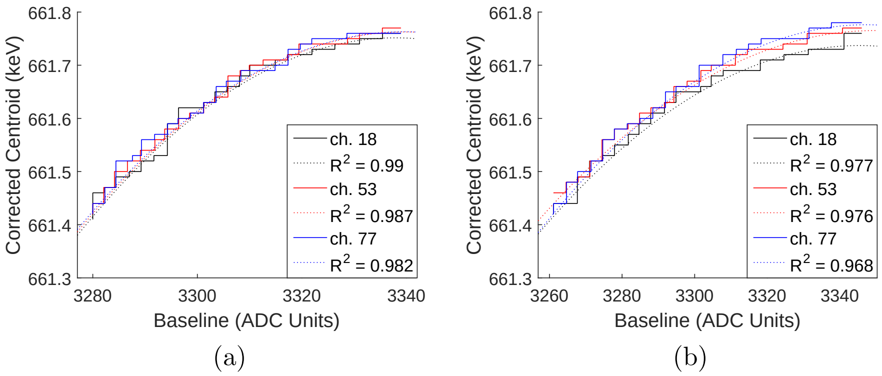

(a) (b)

Figure 4.11: Centroid shift with temperature measurement and quadratic fit of isolated ASICs previously mounted with common grid (a) and simple pixel (b) detectors.

although the linear fits differ, the slopes are of the magnitude as one another and as the overall detector slope for each anode response. Furthermore in isolating the detector and ASIC responses the exact fit is far less important than the magnitude for determining which component is more responsible for the combined temperature response, which this method preserves. The calculated detector response is compared with the collected responses for each detector individually in 4.12. The change in centroids over the temperature range is summarized in Figure 4.13 and clearly shows for each detector, the detector movement dominates the ASIC movement. This conclusively demonstrates the detector is predominantly responsible for the movement of the centroid with temperature. Additionally, the common grid detectors systematically have more movement than the simple pixel detectors, so removing the grid reduces the temperature effect.

4.5 Summary and Future Work

The mere observation that the photopeak invariably shifts when operated at different temperatures means that a more robust temperature correction is needed. Further analysis demonstrates the accuracy and reliability of the built in temperature sensing systems, allowing the cause of the temperature shift to be reliably isolated. Different

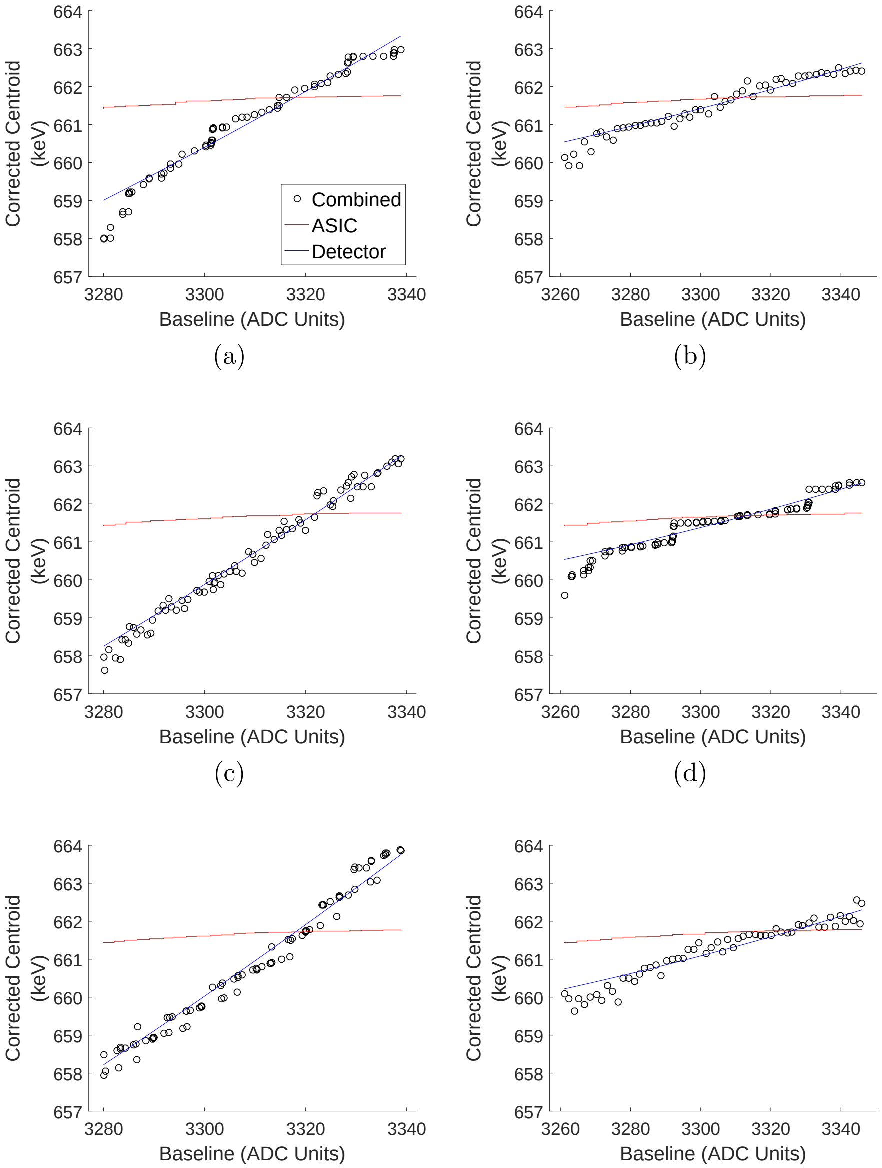

(a) (b) (c) (d) (e) (f)

Figure 4.12: Centroid shifts with temperature for common-grid detectors 4R-89 (a), 4R-135 (c), and 4R-145 (e), and simple-pixel detectors 3R-2 (b), 3R-4 (d), and 5R-1 (f).

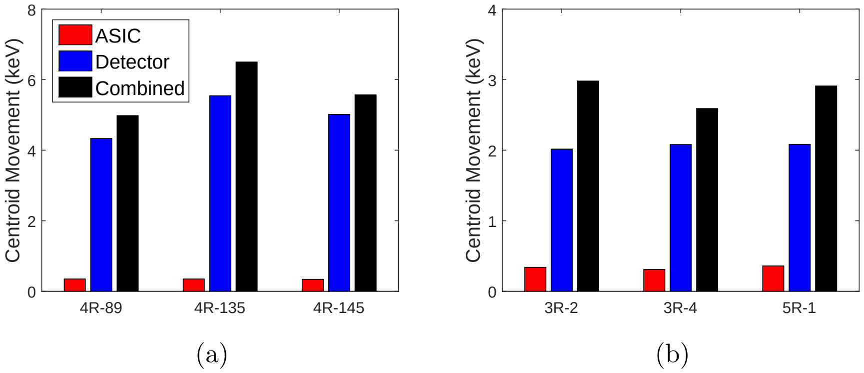

Figure 4.13: Range of centroid movements for each common-grid (a) and each simple-pixel (b) detector.

combined responses for different detectors, and seemingly random variations in the anode combined responses are clues to suggest that the temperature shift is predominantly caused by an anode component of the detector. This is further supported with by a test pulser injected directly into bare ASICs. The drastically reduced centroid movement here attributes the blame primarily on the detectors.

While this work did not specifically identify the physical cause for the photopeak shift, it did narrow the possibilities. Changes in the ASIC performance are not caused by the baseline temperature response because the former is quadratic and the latter is linear. They also cannot be caused by leakage current because the detectors were physically removed during the isolated ASIC measurement. ASIC performance as a function of temperature is therefore dominated by changes in the preamplifier gain and change in the capacitance and resistance of the detector-ASIC coupling with temperature. Changes in the ASIC are negligible compared with changes in the detector. The detector centroid shift with temperature cannot be caused by electron trapping because trapping increases with temperature and reduces the total signal. It would therefore result in the centroid decreasing with temperature, contrary to observations. It is not caused by physical changes to the cathode or to bulk resistivity because the anode centroid movements do not trend with detectors.

This conclusion greatly influences the approach taken to correct for temperature moving forward. On the software level, this work reduces the scope of parameters that must be considered for a future temperature correction to those that are channel-specific and unrelated to the gain correction. While this eliminates many possible causes, it still leaves a number of parameters including the anode timing, the electron mobility-lifetime product, and the peak-hold. The hardware level influence is outside the scope of this work and left to future students, but presents an interesting possibility. If the detector and ASIC can be mechanically separated, only the detector must be temperature-regulated. As the ASIC is the primary heat generator, this would be much less power intensive.

CHAPTER V

A Posteriori Temperature Correction

5.1 Simple Gain Correction

After observing the centroid change as a function of temperature, the ideal next step is to correct it algorithmically. The simplest implementation is a temperature-based gain correction factor applied to the recorded energy. Naively, this factor can be determined via a polynomial fit to the recorded centroid vs. operating temperature curve, and applied during operation to the recorded energy of each event after all other corrections. Because the centroid change as a function of temperature is predominantly linear, and for simplicity of implementation, the gain correction factor is determined by a linear fit.

Despite the apparent straight-forwardness, using a single correction factor for each detector has serious limitations. Fitting only to photopeak centroid determined during the Cs-137 calibration means the temperature gain correction cannot account for any temperature dependence of energy nonlinearity. Furthermore, fitting the overall centroid for each calibration cannot account for slight performance differences between pixels. Finally, grouping all events together for the fitting ignores the different responses between single-pixel and multi-pixel interactions. These limitations can be accounted for using several more specific gain correction implementations, at the cost of requiring additional calibration data.

The performance of corrections accounting for different parameters bounds the calibration data needed for a temperature correction. In principal if the centroid position of each pixel is not an independent function of temperature from the overall centroid position, then a single pixelated Cs-137 calibration is needed. This scenario requires only an overall Cs-137 calibration with less than 1% the number of counts at each other temperature. Otherwise, a full pixelated calibration must be taken at each temperature. Similarly, if energy nonlinearity does not depend on temperature, nonlinearity data is only required at a single temperature.

A posteriori corrections cannot conclusively determine the temperature dependence of the pixel centroid movement or the energy nonlinearity. Instead, the spectroscopic performance of each correction will be compared to approximate the temperature dependence. A performance improvement from accounting for centroid movement between pixels in the temperature correction would suggest that centroid movement by pixel is temperature dependent. A performance improvement from accounting for energy nonlinearity in the temperature correction would similarly suggest that energy nonlinearity is temperature dependent.

5.2 Data Collection

A larger data set was necessary to develop and test temperature gain correction algorithms. Once again the test box was populated with a common-grid detector 4R-186 and a simple-pixel detector 5R-1 each mounted on a GMI analog ASIC and placed within the environmental chamber. A full Cs-137 calibration was taken every 5°C from 5°C to 30°C. Additionally, nonlinearity data was taken with each source except Na-24 described in 2.1 at every temperature. Na-24 has a 15 hour half life thus it must be irradiated from a neutron generator for each trial. With low photoelectric absorption efficiency at 2754 keV, it also requires long collection times to form a single-pixel photopeak. In consideration for these issues, Na-24 was omitted for convenience.

Table 5.1: Eu-152 Energy Lines

Category	Energy (keV)	Intensity (%)	Max Pixels per Event
Included	121.8	25.6	1
	244.7	7.6	1
	344.3	26.5	3
	778.9	12.9	
	964.1	14.6	
	1408.0	21.0	
Excluded: too few counts	411.1	2.2	
	444.0	3.1	
	867.4	4.2	
	1299.1	1.6	
Excluded: overlapping peaks	1085.9	10.2	
	1112.1	13.6	

Throughout this analysis, the temperatures at which these datasets were collected are referred to as the calibration temperatures.

As a check for the temperature corrections, two hour Eu-152 measurements were taken every 2.5°C from 2.5°C to 30°C. Eu-152 is an excellent test source because it has many energy lines across the detector dynamic range, as summarized in Table 5.1. Several lines are excluded due to low intensity. Additionally the 1086 keV and 1112 keV lines overlap and cannot be resolved so they are also excluded. Finally, the 1408 keV line is well developed as used for further analysis, but must be used cautiously because it is slightly outside the upper bound of the nonlinearity calibration set by the Co-60 1333 keV line. Both the minimum trigger threshold and the dominance of photoelectric absorption over other interaction mechanisms makes it unlikely for multi-pixel photopeak events to occur for some low-energy lines. To account for this, only interactions triggering fewer than a maximum number of pixels are considered for additional analysis for these lines.

Finally, a ramping measurement was taken with Cs-137 to provide an additional check of the temperature correction. Here the environmental chamber temperature was increased continuously at a rate of 0.5°C per hour from 5°C to 20°C. Due to hardware availability, this experiment was performed with only the 4R series detector. Furthermore, because a ramp measurement cannot self-calibrate, there is no optimal performance for this experiment. Instead, only the improvement in using the temperature gain correction versus using no temperature correction is shown.

5.3 Correction Algorithms

Before developing the temperature corrections, consider a fixed-temperature calibration. Calibration data is taken at a calibration temperature T_c, processed, and used to correct events collected at an operating temperature T_{op}. The corrected centroid can be expressed as a function of both temperatures $E_{FT}(T_c, T_{op})$. During fixed-temperature operation, $T_c = T_{op}$ and no additional correction is necessary.

During variable-temperature operation, temperature corrections are necessary. The a posteriori temperature gain corrections examined in this chapter all follow the same paradigm: an incident event is processed via a fixed-temperature calibration collected at pivot temperature T_p, then post-processed with an additional correction parameter C_T to determine the energy for that event. Throughout this work, the pivot temperature is 15°C because it is in the center of the temperature range of collected measurements. A function for the correction parameter is calculated prior to operation by processing the dataset taken at each calibration temperature in the set S_T with the pivot temperature fixed-temperature calibration parameters, then calculating a linear fit for the centroids, as shown in Equation (5.1).

$$C_T(T_p, T_{op}) = \mathrm{Linfit}\Big(E_{FT}(T_p, T \in S_T)\Big) \tag{5.1}$$

The temperature-corrected energy E_{VT} is then the quotient of the energy determined from the fixed temperature calibration and the temperature correction factor, as shown in Equation (5.2).

$$E_{VT}(T_p, T_{op}) = \frac{E_{FT}(T_p, T_{op})}{C_T(T_p, T_{op})} \tag{5.2}$$

When developing gain correction algorithms, there are several important questions: are the pixels corrected individually or averaged for the entire detector; are events all treated the same or categorized by the number of pixels that triggered; is energy nonlinearity accounted for? This section addresses each question algorithmically, where each combination of answers forms a different correction algorithm.

5.3.1 Pixel Treatment

The first question is the simplest. Using the overall performance, there is a single temperature gain correction for the entire detector, whereas using the pixel-by-pixel performance will result in a different temperature correction for each pixel $C_T(p)$. For single pixel events, the implementation is the same and the temperature-corrected energy is calculated after all other corrections by taking the product of the recorded energy and the gain correction.

For multi-pixel events, the implementations differ. Using a single detector correction, the correction factor is multiplied only after the recorded energies are summed over each triggered pixel, as shown in Equation (5.3). Using a pixelated correction, the correction factor is multiplied by the recorded energy in each pixel, then the products are summed. This is shown in Equation (5.4).

$$E_{VT} = \frac{\sum_p E_{FT}(p)}{C_T} \tag{5.3}$$

$$E_{VT} = \sum_p \frac{E_{FT}(p)}{C_T(p)} \tag{5.4}$$

A pixelated correction can account for temperature-dependent changes on a smaller scale than the overall correction, so may improve performance. Individual pixels have reduced counting statistics thus see greater random fluctuation in the centroid even at fixed temperatures compared with the detector taken as a whole. Additionally, nonlinear changes with temperature in individual pixels would adversely affect a pixelated correction but would likely be averaged out in an overall-detector correction.

5.3.2 Event Categorization

An event can trigger either one, two, three, four, or five-or-more pixels. Calling this number the event class C_e, it is known to affect spectroscopic performance at fixed temperatures. For convenience, event class zero is defined as all events, regardless of the number of pixels triggered. To account for the spectroscopic effects as a function of temperature, a correction factor $C_T(C_e)$ is calculated for each nonzero event class. Similar to an overall correction, this factor is multiplied in the final step by the sum of the recorded energies from each triggered pixel to yield the temperature-corrected energy.

The pixelated correction requires a one-to-one correlation between known deposition energy and the recorded energy in each pixel. While the deposition energy for multi-pixel photopeak events is known for the detector overall, the energy for individual triggered pixels varies by event and cannot be binned into a single peak that can be used for correction. Consequently the pixelated temperature correction only uses single-pixel photopeak events, and is therefore incompatible with an event class temperature correction.

5.3.3 Nonlinearity Accounting

To account for nonlinearity, an energy term is incorporated into the temperature gain correction $C_T(E_{FT})$. Once again the gain correction factor is multiplied in the last step, either before or after summing the recorded energies depending on whether it is implemented for the entire detector or by pixels. It is important to note that this correction is applicable to Cs-137 measurements where for multi-pixel events there is a range of possible energy depositions in each pixel. For example, a two-pixel photopeak event with a 100 keV and a 561.7 keV deposition will use different nonlinearity correction factors than a two-pixel photopeak event with two 330.85 keV depositions.

While all other temperature gain corrections thus far are implemented the same way during post-calibration operation, accounting for energy nonlinearity adds an additional step. A fit to the Cs-137 photopeak position as a function of temperature can be precalculated during calibration, and the temperature correction factor is calculated during operating from this linear fit. Because fixed-temperature nonlinearity fits the photopeak positions with a fifth order polynomial, simple two-dimensional interpolation isn't accurate. Precalculating a lookup table during calibration is computationally cheap, but memory intensive. Instead, during operation the fixed-temperature nonlinearity correction is applied to the recorded energy for each temperature in S_T, rather than just the pivot temperature. This yields temperature-dependent nonlinearity-corrected energies $E_{NL}(E_{FT}, T \in S_T)$. A linear trend is fit to these and evaluated at the temperature of the incident event to determine the gain correction factor, as shown in Equation (5.5)

$$C_T(E_{FT}) = \text{Linfit}\Big(E_{NL}(E_{FT}, T \in S_T)\Big) \tag{5.5}$$

5.4 Performance Quantification

To assess each gain correction implementation, the spectroscopic performance of each must be quantified. The primary goal is to correct the centroid shift, so that measurements of a known source record the photopeak in the correct position regardless of operating temperature. This is addressed by comparing the variance of the centroid shift for each correction. The secondary goal is to maintain excellent energy resolution, which is addressed by comparing the FWHM of each photopeak before and after gain correction.

5.4.1 Centroid Variance

To quantify the centroid shift, the squared difference between the measured E_m and known E photopeak centroid is recorded at each temperature for each event class. The centroid variance for each event class $V_E(C_e)$ is defined as the sum of the squared differences for each temperature, as shown in Equation (5.6). The overall centroid variance V_E is then defined as the sum of the variance for each nonzero event class weighted by the number of recorded photopeak events $n(C_e)$ in that event class, shown in Equation (5.7). This weighting scheme is selected because the overall spectrum is simply the sum of the spectra for each event class, and the ultimate goal is to correct the overall centroid position.

$$V_E(C_e) = \sum_T (E_m(T, C_e) - E)^2 \tag{5.6}$$

$$V_E = \sum_{C_e} \frac{V_E(C_e)}{n(C_e)} \tag{5.7}$$

Using only the Cs-137 measurements, there is a single centroid variance for each temperature gain correction implementation. However, it is calculated independently for each photopeak, thus when considering the Eu-152 measurements the variance $V_E(E)$ can be expressed as a function of energy. One additional complication is selecting the known photopeak centroid value. The gamma-ray energy emitted by each isotope is the obvious selection, but using this in the variance calculation unfairly attributes inaccuracies in the fixed-temperature calibration procedure to the temperature correction. Instead, the centroid of each peak determined during each fixed-temperature calibration is used as the known centroid. This is referred to as the self-calibration centroid E_{sc}, is found for each calibration temperature, and has the simple equivalence expressed in Equation (5.8).

$$E_{sc}(T_c) = E_{FT}(T_c, T_c) \tag{5.8}$$

5.4.2 Resolution Ratio

The most straightforward way to analyze the effects of temperature correction on spectroscopy is to simply compare the resolution at each temperature, for each event class. This, however, does not account for changes in the fixed-temperature performance as a function of temperature. To generate a fair comparison, the resolution ratio $r_R(C_e)$ is defined for each event class as the ratio of the measured R_m and self-calibrated R_{sc} resolutions averaged over the temperature domain, as shown in Equation (5.9).

$$r_R(C_e) = |S_T|^{-1} \sum_{T \in S_T} \frac{R_m(T, C_e)}{R_{sc}(T, C_e)} \tag{5.9}$$

Resolution is a measure of uncertainty and depends variation in the number of charge carriers per event, counting statistics, and electronic noise. In the ASIC used, electronic noise is the dominant contributing factor. Assuming independent noise in each preamp, the two-pixel events for example are the sum of one-pixel events each affected by noise. Recalling that standard deviations add in quadrature, in this example the two-pixel resolution must be $\sqrt{2}$ times the one-pixel. In practice, factors such as weighting potential cross-talk and cross-correlated noise further degrade the multi-pixel resolution, so the square root of the event class is useful only as a lower bound. Still, it is used to calculate the event-class independent resolution ratio r_R, which is defined as the weighted average of the event-class specific resolution ratios. This is shown in Equation (5.10).

$$r_R = \left(\sum_{n=1}^{5} (\sqrt{n})^{-1} \right) \left(\sum_{C_e} \frac{r_R(C_e)}{\sqrt{C_e}} \right) \tag{5.10}$$

5.5 Correction Results

Before examining the details of each correction, it is helpful to visualize the effects of such a correction. Treating the self-calibration photopeak as the optimum solution and the uncorrected results as the baseline, each temperature gain correction implementation should have spectroscopic performance intermediate between the two. To illustrate, Figure 5.1 shows the overall energy spectra near the photopeak of the 5°C measurement after self-correction, after correction with the pivot temperature calibration and no temperature correction, and using the Cs-137-only event class temperature gain correction for the simple-pixel detector. The correction significantly improves the centroid position, moving it from 660.95 keV to 661.75 keV, much nearer to the 661.64 keV target value. The resolution improvement is minimal, however, changing from 1.63% without correction to 1.58% with correction and falling far short of the 1.3% value seen with self-calibration.

Because the self-calibration performance is used as the optimum, it sets the upper bound of each temperature gain correction. The centroids are known a priori and used during fixed-temperature calibration for photopeak alignment, thus are matched well by the self-calibration data and are not shown. Conversely, the self-calibration resolution isn't known a priori and does vary with each measurement. These values are therefore shown for the Cs-137 measurements by event class in Figure 5.2 with the common-grid detector and in Figure 5.3 with the simple-pixel detector, for the nonlinearity measurements in Figure 5.4 with the common-grid detector and Figure 5.5 with the simple-pixel detector, and for the Eu-152 measurements in Figure 5.6 with the common-grid detector and Figure 5.7 with the simple-pixel detector.

In both detectors, the resolution is relatively constant at low temperatures and

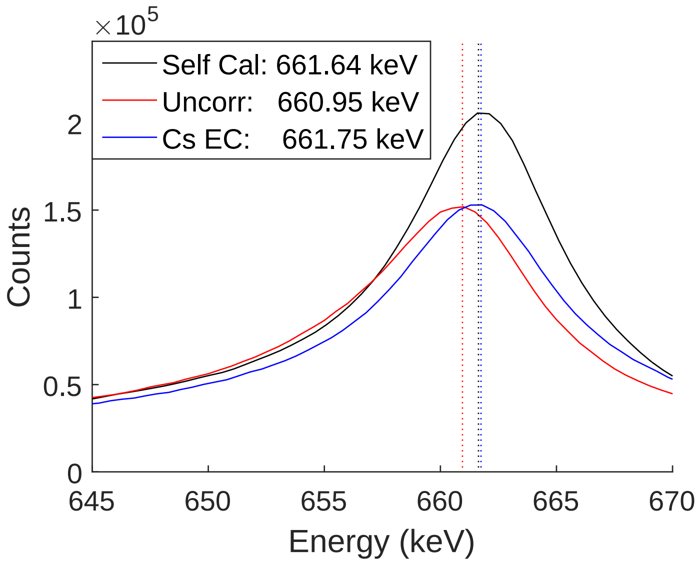

Figure 5.1: Comparison of photopeaks for simple-pixel 5°C measurement found via self-calibration, 15°C calibration, and 15°C calibration with gain-temperature correction.

degrades significantly with increasing temperature. This is true for all three sets of measurements. This degradation could result from increased leakage current and electronic noise reducing SNR. In the common-grid detector, this degradation is nonlinear with temperature, and so severe in the 25°C and 30°C measurements that they are excluded from temperature correction analysis. In the simple-pixel detector, some nonlinearity and Eu-152 peaks begin to overlap and are unresolvable in the 30°C measurement, thus these measurements are excluded from this analysis. As a function of photopeak energy E_{ppc}, the resolution behaves as expected, improving statistically at a rate of $1/\sqrt{E_{ppc}}$. In the simple-pixel detector, the resolution of each event class improves with energy but the overall resolution degrades at very high energies. This indicates that the nonlinearity corrections by event class are individually good, but poorly aligned. This trend does not affect the Cs-137-only temperature gain corrections, and washes out in the nonlinearity temperature gain corrections taken by event class.

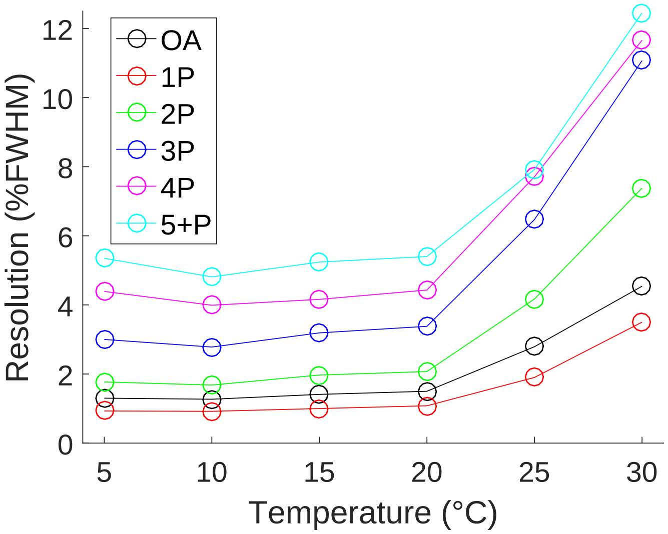

Figure 5.2: Self-calibration resolutions as a function of temperature for Cs-137 measurements by event class for common-grid detector.

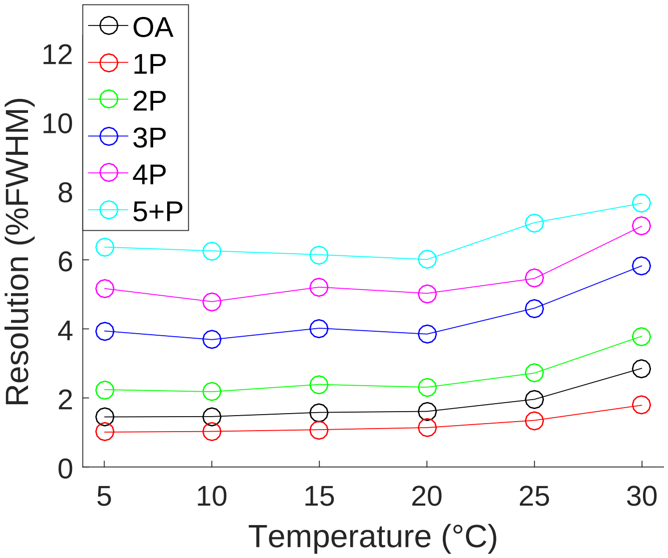

Figure 5.3: Self-calibration resolutions as a function of temperature for Cs-137 measurements by event class for simple-pixel detector.

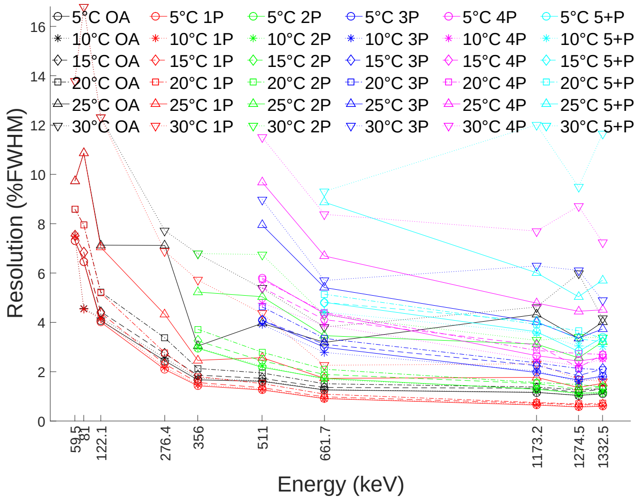

Figure 5.4: Self-calibration resolutions as a function of photopeak energy for non-linearity measurements by event class and environmental chamber temperature for common-grid detector.

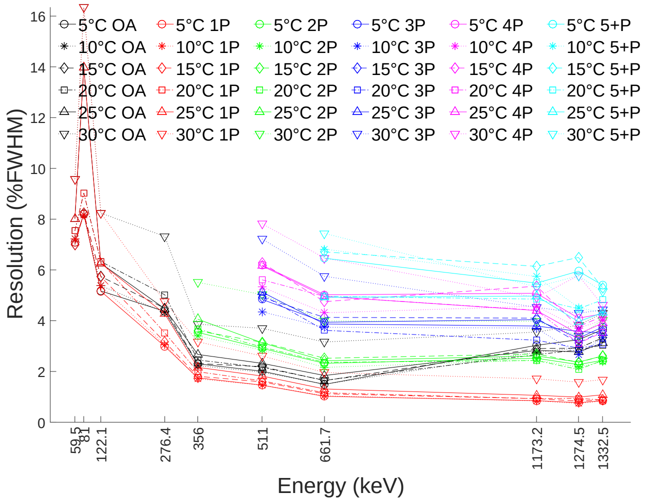

Figure 5.5: Self-calibration resolutions as a function of photopeak energy for non-linearity measurements by event class and environmental chamber temperature for simple-pixel detector.

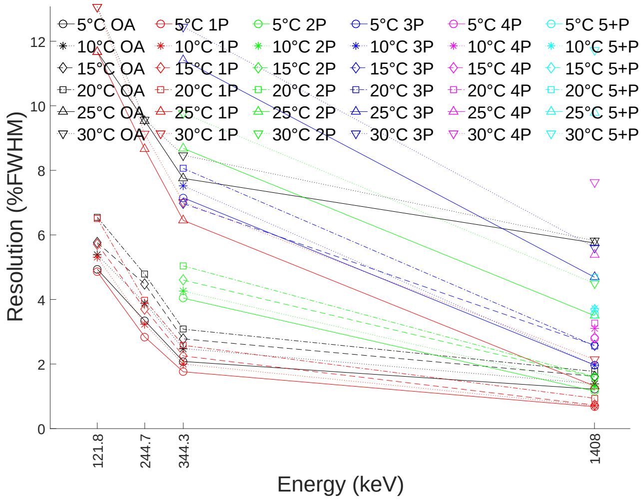

Figure 5.6: Self-calibration resolutions as a function of photopeak energy for Eu-152 measurements by event class and environmental chamber temperature for common-grid detector.

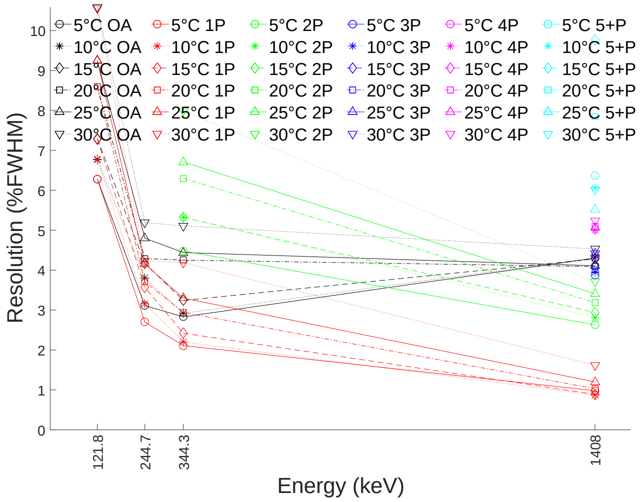

Figure 5.7: Self-calibration resolutions as a function of photopeak energy for Eu-152 measurements by event class and environmental chamber temperature for simple-pixel detector.

5.5.1 Cs-137 Measurements

With the baseline and optimal spectroscopy understood, the performance of each temperature gain correction method is examined. Of the eight total correction parameter combinations, the six physically meaningful methods are compared to determine which if any should be adopted for standard operation. The methods are applied independently and are summarized in Table 5.2. For the Cs-137 measurements, the centroid variances calculated via equation (5.6) are shown with the common-grid detector in Figure 5.8 and with the simple-pixel detector in Figure 5.9. The resolution ratios calculated via equation (5.9) are shown with the common-grid detector in Figure 5.10 and with the simple-pixel detector in Figure 5.11.

The goal of each correction is to most closely approximate the self-calibration performance and centroid variance is a function of the difference between the self-calibration and temperature-corrected centroid positions. Consequently the corrections with the lowest variance values are the best and corrections with variance values greater than using no temperature correction are worthless. Fortunately, in examining the centroid variances it is clear that every correction improves on the performance without any correction, particularly for the overall and low event class spectra. Additionally, the Cs-137-only event-class correction has the least centroid variance, while the pixelated corrections have the most. Collectively, the Cs-137-only corrections also show reduced variance compared with the analogous nonlinearity corrections, but this is intuitively expected because they are here applied only to data taken with Cs-137.

Taking into account the resolution ratios, every correction has resolution degradation compared to the self-calibration performance. The overall corrections use only a single temperature correction value at Cs-137 energy, regardless of pixel or event class, so the overall corrected resolution must match the overall uncorrected resolution. The corrected event class resolutions of the event-class corrections must analogously match the uncorrected event class resolutions, although the overall corrected resolution can

Table 5.2: Temperature Gain Correction Methods

Abbreviation	Cs-137 Only (Cs) or Nonlinearity (NL)	Overall (OA) or Event class (EC)	Whole detector (WD) or Pixelated (Pix)
Cs OA	Cs	OA	WD
Cs Pix	Cs	OA	Pix
Cs EC	Cs	EC	WD
n/a	Cs	EC	Pix
NL OA	NL	OA	WD
NL Pix	NL	OA	Pix
NL EC	NL	EC	WD
n/a	NL	EC	Pix

differ because the event class photopeaks are realigned. For the pixelated corrections, each pixel is aligned separately, so the corrected and uncorrected resolutions can differ. In both detectors, the resolutions for the overall corrections match the uncorrected as expected, the resolutions for the event class corrections show improvement in the overall spectrum due to better event class photopeak alignment, and the pixelated corrections show significantly degraded resolution. The pixelated corrections include more data and should in principle show improved resolution. The degradation seen in practice may be explained by a linear model fitting the overall detector better than individual pixels or by poor pixel peak alignment. For the overall and event class corrections, the Cs-137-only and nonlinearity resolutions closely match, as again expected because they are applied here only to data taken with Cs-137.

5.5.2 Nonlinearity Measurements

The same corrections are performed on the nonlinearity measurements and the analysis is repeated. The centroid variances are shown individually for each photopeak energy via equation (5.6) with the common-grid detector in Figure 5.12 and with the simple-pixel detector in Figure 5.13. The resolution ratios are similarly shown individually via equation (5.9) with the common-grid detector in Figure 5.14 and with

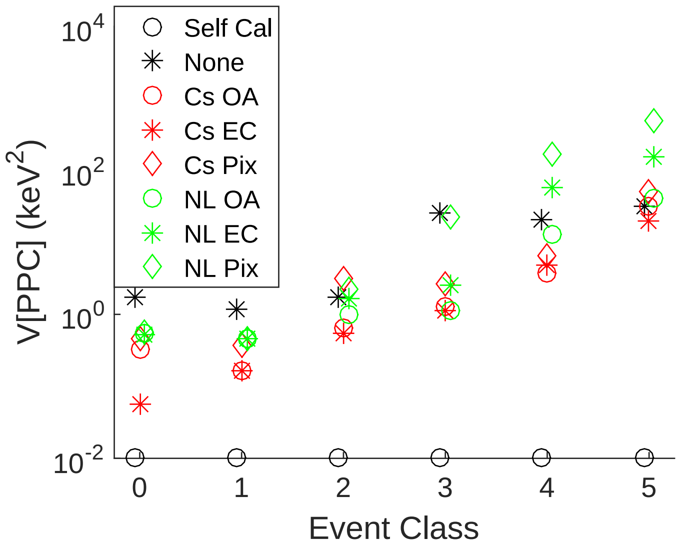

Figure 5.8: Centroid variances for each temperature gain correction method applied to Cs-137 measurements taken with common-grid detector. Self-calibration values are zero by definition and here artificially raised to appear on logarithmic axis.

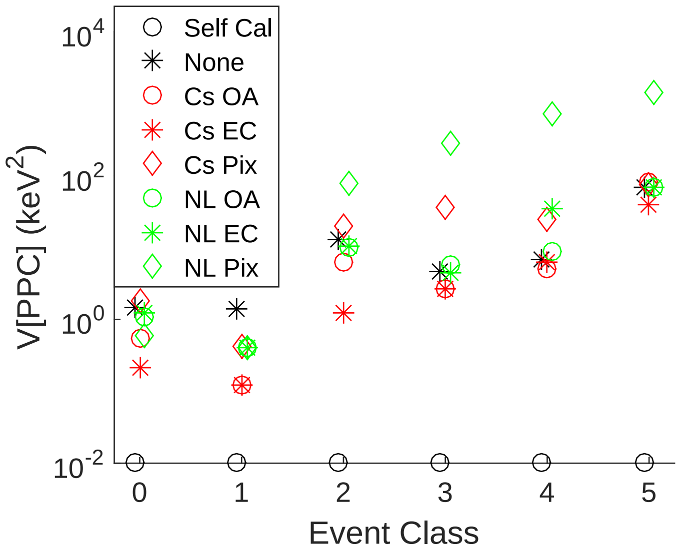

Figure 5.9: Centroid variances for each temperature gain correction method applied to Cs-137 measurements taken with simple-pixel detector. Self-calibration values are zero by definition and here artificially raised to appear on logarithmic axis.

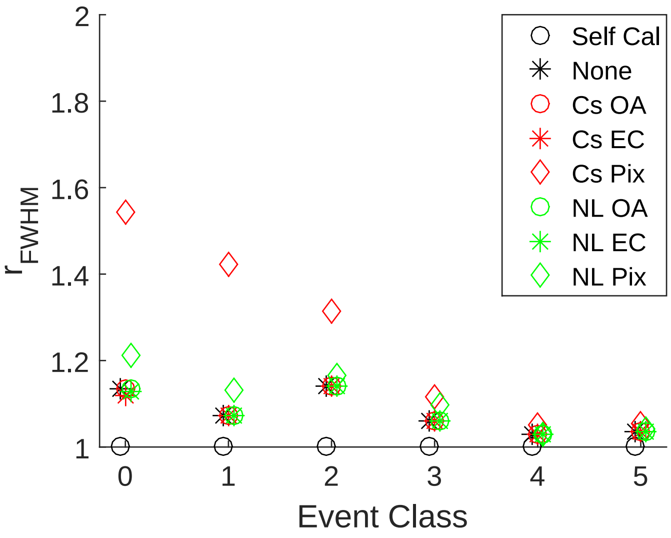

Figure 5.10: Resolution ratios for each temperature gain correction method applied to Cs-137 measurements taken with common-grid detector.

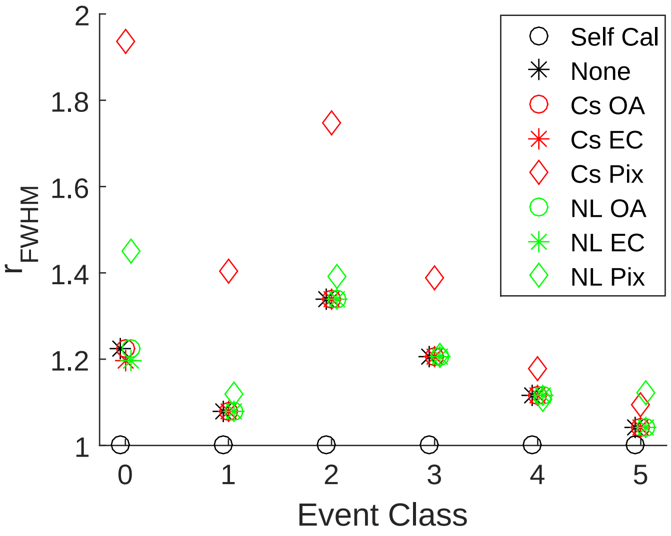

Figure 5.11: Resolution ratios for each temperature gain correction method applied to Cs-137 measurements taken with simple-pixel detector.

the simple-pixel detector in Figure 5.15. The Ba-133 384 keV and the Co-57 137 keV lines cannot be clearly resolved with every correction at every temperature thus are omitted from analysis. Additionally, the Ba-133 384 keV line is not sufficiently above background for every correction at every temperature to determine the resolution thus is omitted from the resolution ratio analysis.

Looking at the centroid variances, the Cs-137-only event class correction once again shows the best performance in both detectors and across the entire energy range, followed closely by the Cs-137-only overall correction. The Cs-137-only pixelated correction has very little centroid deviation from the self-calibration for photopeaks below 200 keV, but rapidly degrades and has worse performance than the uncorrected centroids above 600 keV. In both detectors, the nonlinearity temperature gain corrections are ubiquitously worse than the Cs-137-only corrections, indicating the fixed-temperature nonlinearity corrections don't change linearly with temperature. Comparatively, the pixelated nonlinearity correction outperforms the overall and event class nonlinearity corrections throughout the entire energy range in the common-grid detector and above 600 keV in the simple-pixel detector. This implies that the systematic variation as a function of temperature and energy exceeds the random variation by pixel, particularly for higher energies. This is possibly because the nonlinearity dependence on temperature is more linear in each pixel, but very different between pixels, so that the average of all pixels results in a less linear temperature dependence.

The resolution ratios shows similar trends, where solely the Cs-137-only correction improves on the overall energy resolution compared with no temperature correction. In both detectors, the pixelated corrections severely degrade the resolution across the entire energy range. Additionally, the nonlinearity pixelated correction typically shows reduced degradation. This improved peak alignment indicates that pixel-by-pixel there is some dependence of the temperature correction on the incident energy, but when averaged over all the pixels this dependence is smaller than the random performance variation across the pixels.

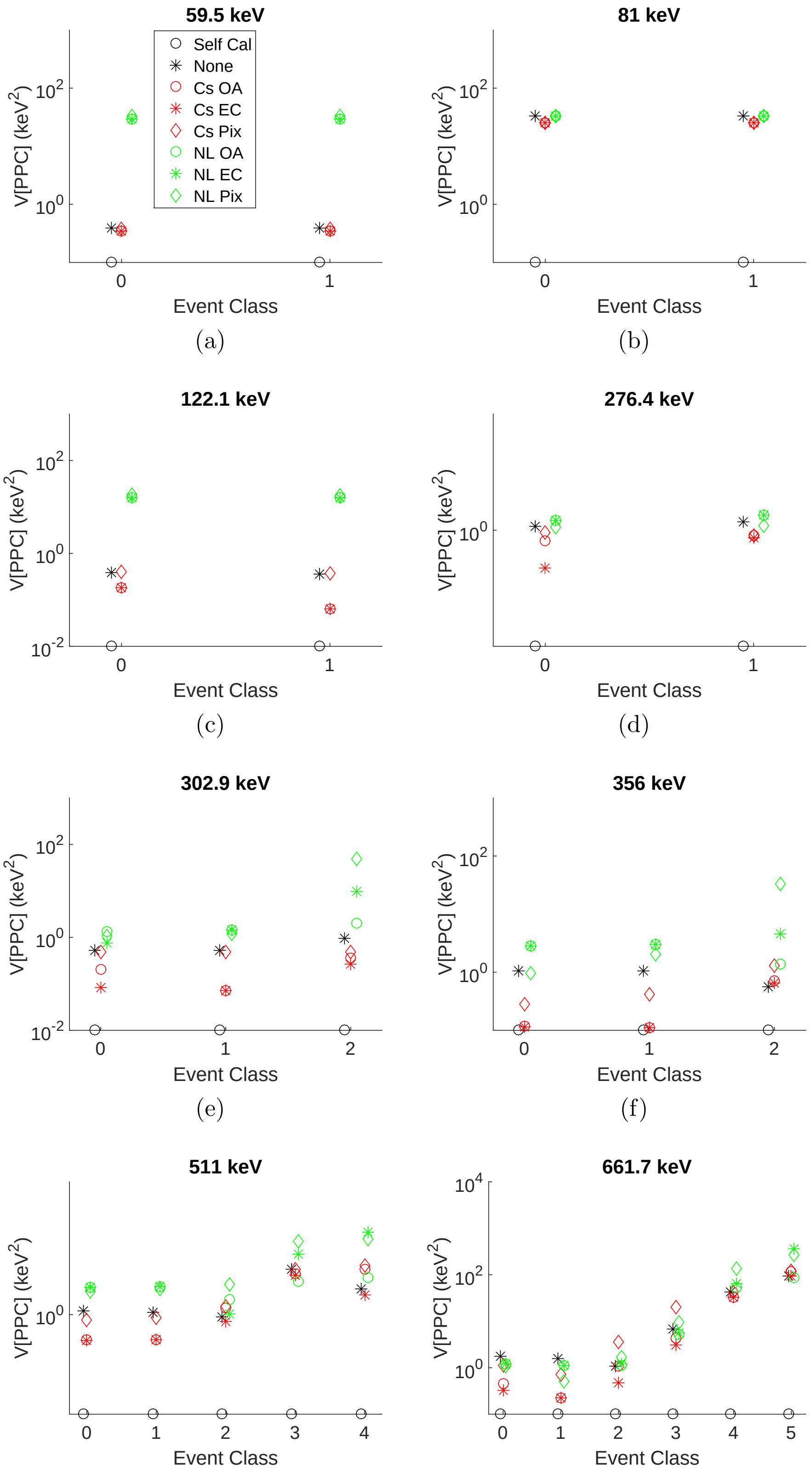
59.5 keV
81 keV
122.1 keV
276.4 keV
302.9 keV
356 keV
511 keV
661.7 keV
Self Cal
None
Cs OA
Cs EC
Cs Pix
NL OA
NL EC
NL Pix
V[PPC] (keV^2)
10^{-2}
10^0
10^2
10^4
Event Class
0
1
2
3
4
5

(a)

(b)

(c)

(d)

(e)

(f)

(g)

(h)

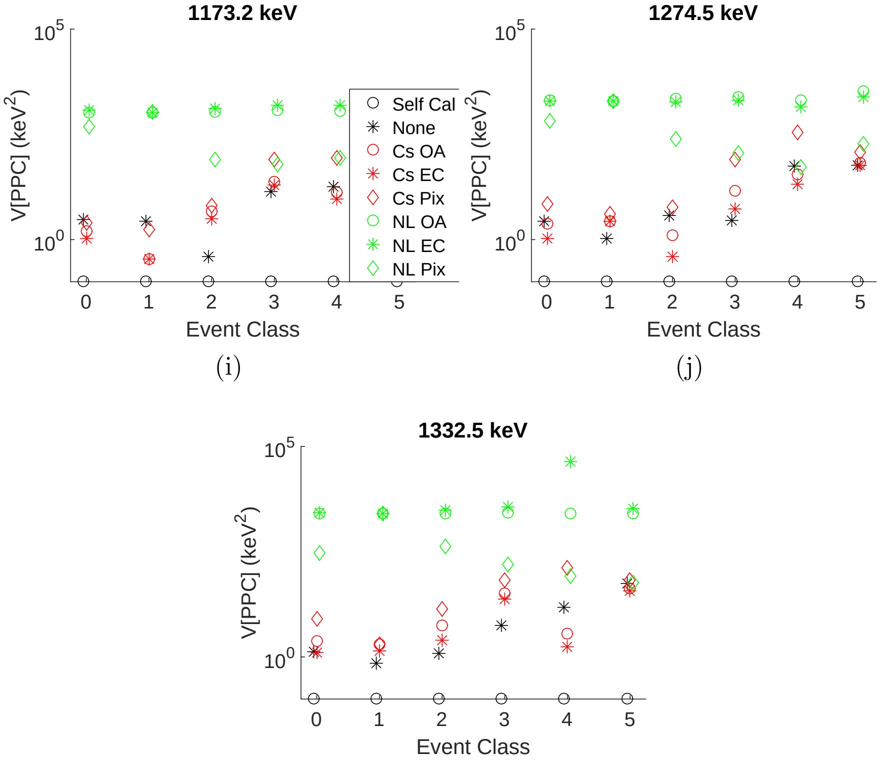

(i) (j)

(k)

Figure 5.12: Centroid variances for each temperature gain correction method applied to nonlinearity measurements taken with common-grid detector where subsequent plots correct sequentially increasing photopeak energies. The peaks corrected specifically are Am-241 60 keV in (a), Ba-133 81 keV in (b), Co-57 122 keV in (c), Ba-133 276 keV in (d), Ba-133 302 keV in (e), Ba-133 356 keV in (f), Na-22 511 keV in (g), Cs-137 662 keV in (h), Co-60 1173 keV in (i), Na-22 1275 keV in (j), and Co-60 1333 keV in (k). Self-calibration values are zero by definition and here artificially raised to appear on logarithmic axes.

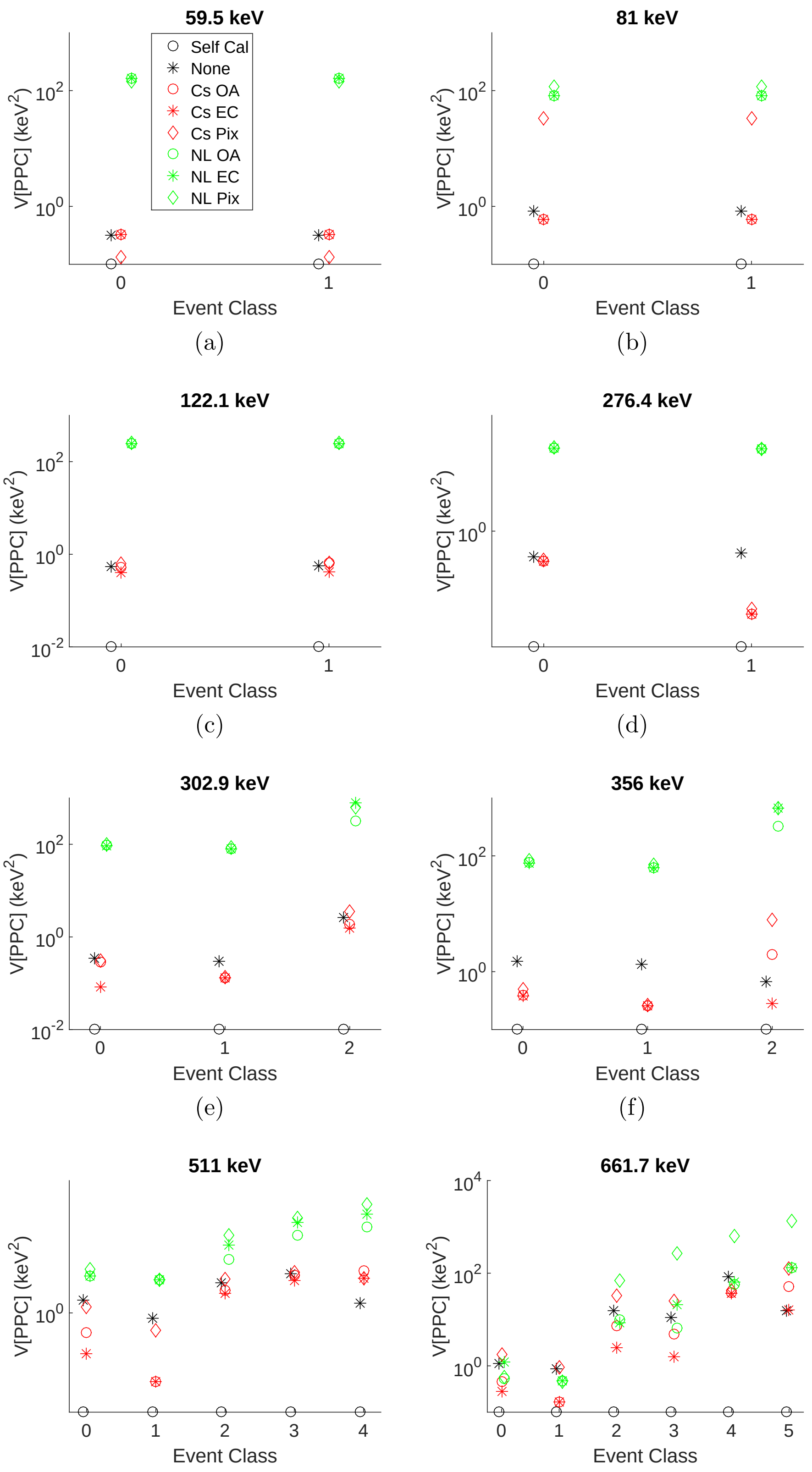
59.5 keV
81 keV
122.1 keV
276.4 keV
302.9 keV
356 keV
511 keV
661.7 keV
Self Cal
None
Cs OA
Cs EC
Cs Pix
NL OA
NL EC
NL Pix
V[PPC] (keV^2)
10^{-2}
10^0
10^2
10^4
Event Class
0
1
2
3
4
5

(a)

(b)

(c)

(d)

(e)

(f)

(g)

(h)

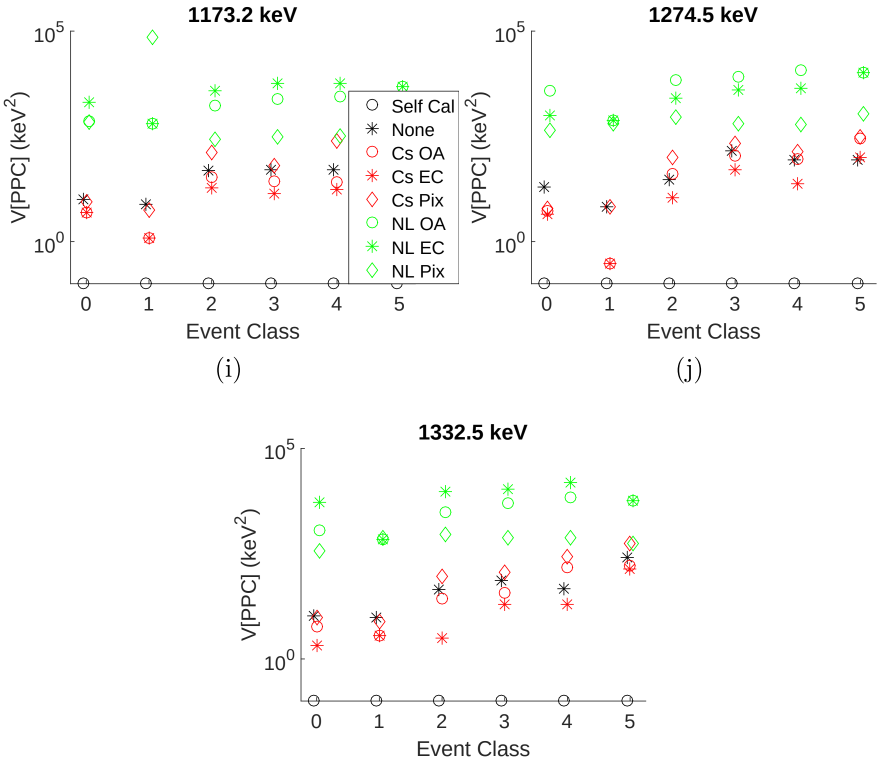

(i) (j)

(k)

Figure 5.13: Centroid variances for each temperature gain correction method applied to nonlinearity measurements taken with simple-pixel detector where subsequent plots correct sequentially increasing photopeak energies. The peaks corrected specifically are Am-241 60 keV in (a), Ba-133 81 keV in (b), Co-57 122 keV in (c), Ba-133 276 keV in (d), Ba-133 302 keV in (e), Ba-133 356 keV in (f), Na-22 511 keV in (g), Cs-137 662 keV in (h), Co-60 1173 keV in (i), Na-22 1275 keV in (j), and Co-60 1333 keV in (k). Self-calibration values are zero by definition and here artificially raised to appear on logarithmic axes.

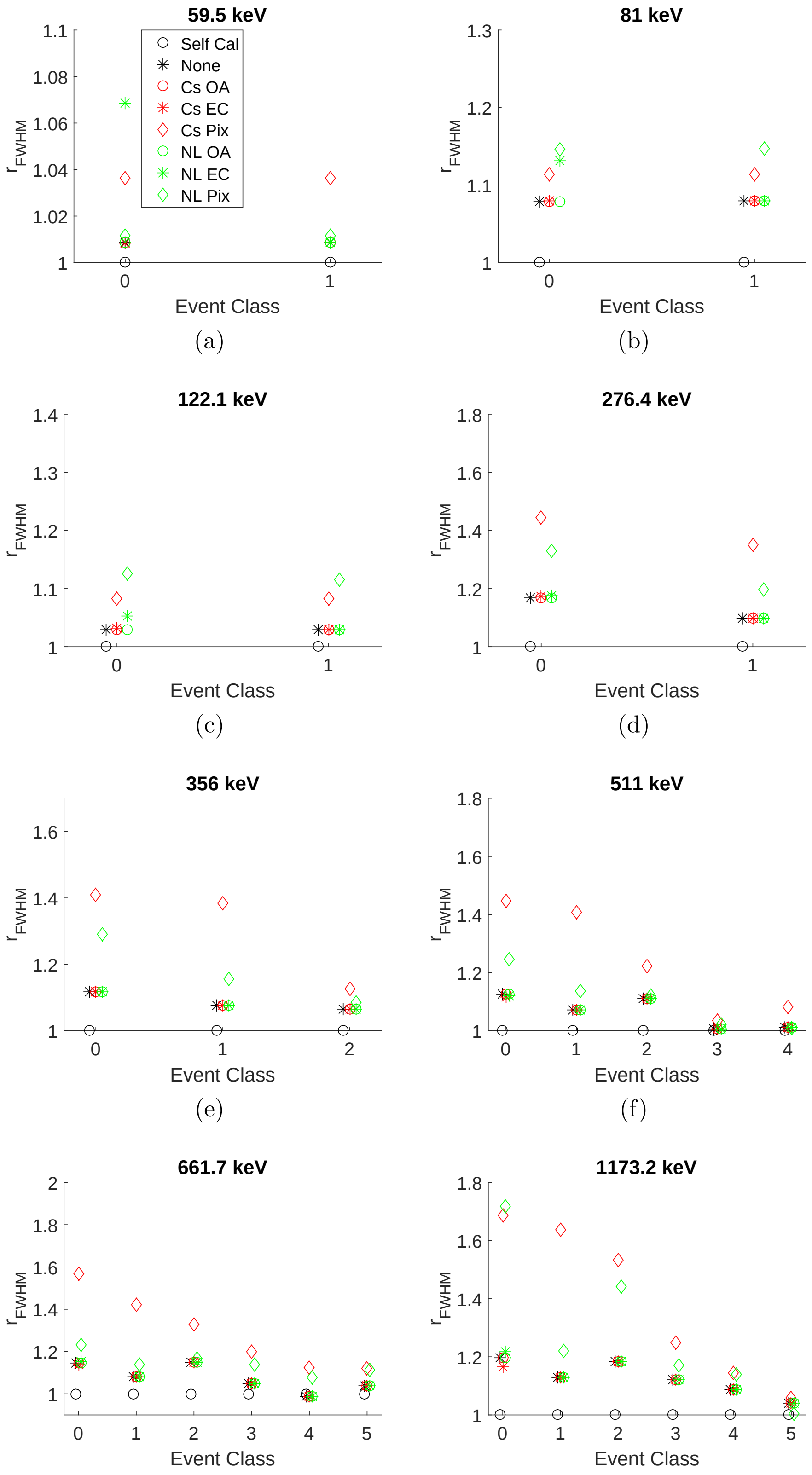
59.5 keV
Self Cal
None
Cs OA
Cs EC
Cs Pix
NL OA
NL EC
NL Pix
r_{FWHM}
1.1
1.08
1.06
1.04
1.02
1
0
1
Event Class
81 keV
r_{FWHM}
1.3
1.2
1.1
1
0
1
Event Class
122.1 keV
r_{FWHM}
1.4
1.3
1.2
1.1
1
0
1
Event Class
276.4 keV
r_{FWHM}
1.8
1.6
1.4
1.2
1
0
1
Event Class
356 keV
r_{FWHM}
1.6
1.4
1.2
1
0
1
2
Event Class
511 keV
r_{FWHM}
1.8
1.6
1.4
1.2
1
0
1
2
3
4
Event Class
661.7 keV
r_{FWHM}
2
1.8
1.6
1.4
1.2
1
0
1
2
3
4
5
Event Class
1173.2 keV
r_{FWHM}
1.8
1.6
1.4
1.2
1
0
1
2
3
4
5
Event Class

(a)

(b)

(c)

(d)

(e)

(f)

(g)

(h)

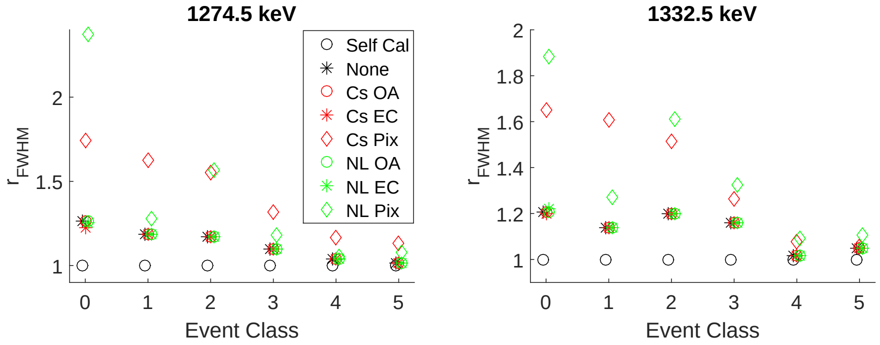

(i) (j)

Figure 5.14: Resolution ratios for each temperature gain correction method applied to nonlinearity measurements taken with common-grid detector where subsequent plots correct sequentially increasing photopeak energies. The peaks corrected specifically Am-241 60 keV in (a), Ba-133 81 keV in (b), Co-57 122 keV in (c), Ba-133 276 keV in (d), Ba-133 356 keV in (e), Na-22 511 keV in (f), Cs-137 662 keV in (g), Co-60 1173 keV in (h), Na-22 1275 keV in (i), and Co-60 1333 keV in (j).

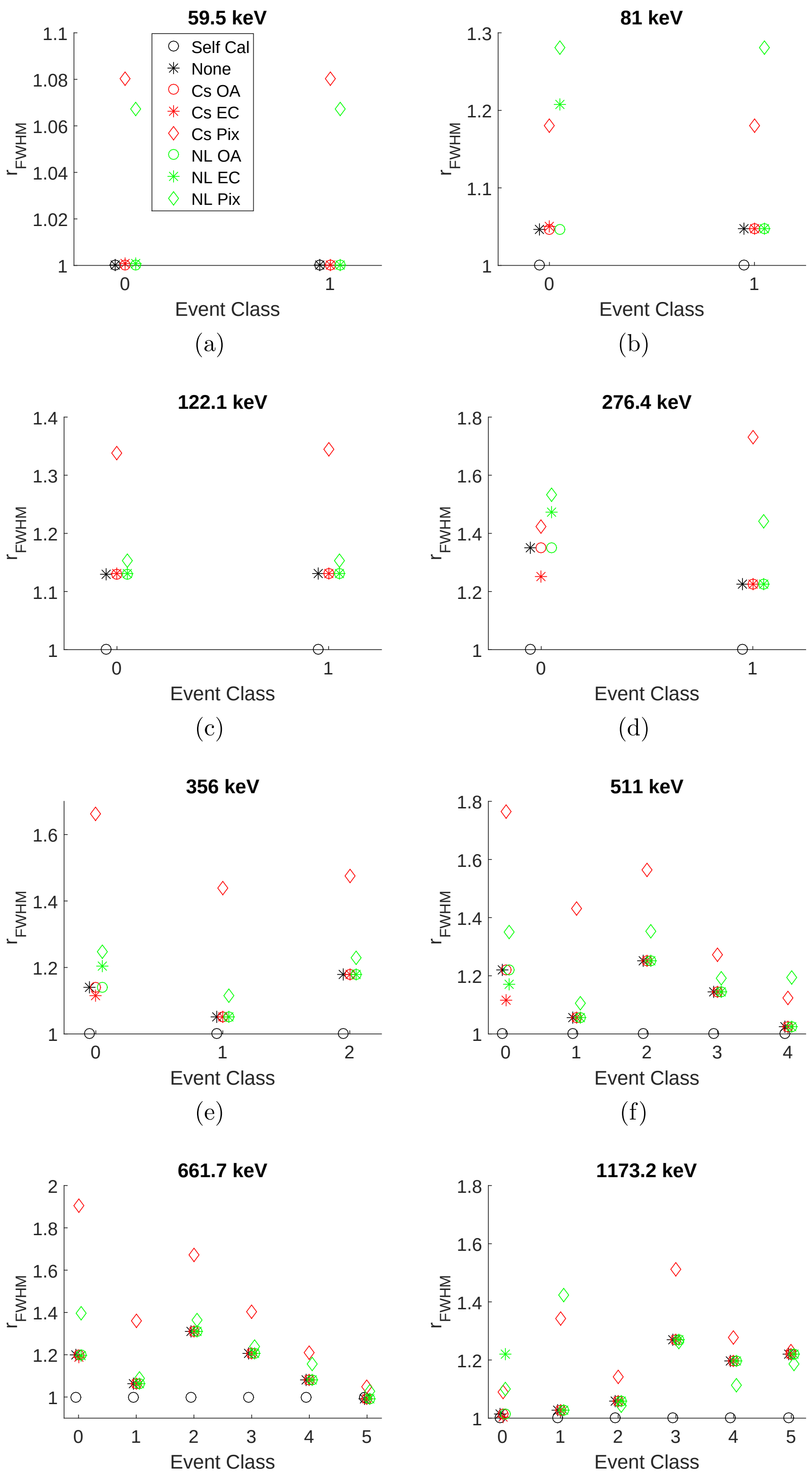
59.5 keV
81 keV
122.1 keV
276.4 keV
356 keV
511 keV
661.7 keV
1173.2 keV
Self Cal
None
Cs OA
Cs EC
Cs Pix
NL OA
NL EC
NL Pix
r_{FWHM}
Event Class
1
1.02
1.04
1.06
1.08
1.1
1.2
1.3
1.4
1.6
1.8
2
0
1
2
3
4
5

(a)

(b)

(c)

(d)

(e)

(f)

(g)

(h)

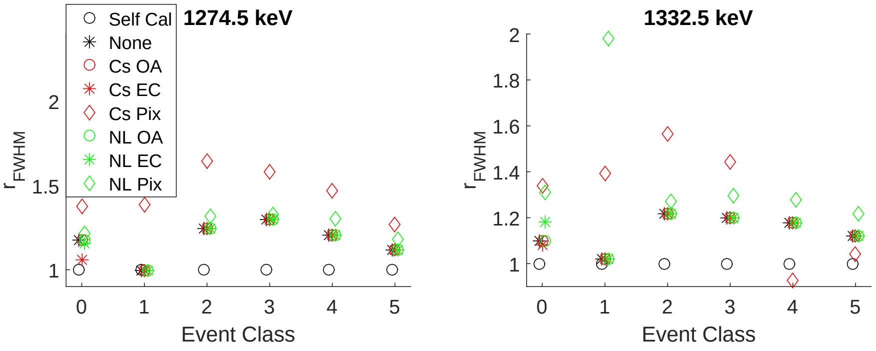

(i) (j)

Figure 5.15: Resolution ratios for each temperature gain correction method applied to nonlinearity measurements taken with simple-pixel detector where subsequent plots correct sequentially increasing photopeak energies. The peaks corrected specifically Am-241 60 keV in (a), Ba-133 81 keV in (b), Co-57 122 keV in (c), Ba-133 276 keV in (d), Ba-133 356 keV in (e), Na-22 511 keV in (f), Cs-137 662 keV in (g), Co-60 1173 keV in (h), Na-22 1275 keV in (i), and Co-60 1333 keV in (j).

Although they contain less information, the combined results are more illustrative of the relative performance of each correction. The combined centroid variances calculated via equation (5.7) are shown with the common-grid detector in Figure 5.16 and with the simple-pixel detector in Figure 5.17. Analogously, the combined resolution ratios calculated via (5.10) are shown with the common-grid detector in Figure 5.18 and with the simple-pixel detector in Figure 5.19.

The trends here are very clear and consistent in both detectors. The Cs-137-only event class correction shows the least variance and non-degraded resolution. The Cs-137-only pixelated and all nonlinearity corrections show greater variation than the uncorrected results. In terms of resolution, the nonlinearity pixelated correction shows slight degradation while the Cs-137-only pixelated correction shows significant degradation across the entire energy range. In both cases the results are poor and likely in part caused by poorer statistics. Therefore the nonlinearity pixelated correction outperforming Cs-137-pixelated correction may simply be caused by the greater number of counts included in the measurement.

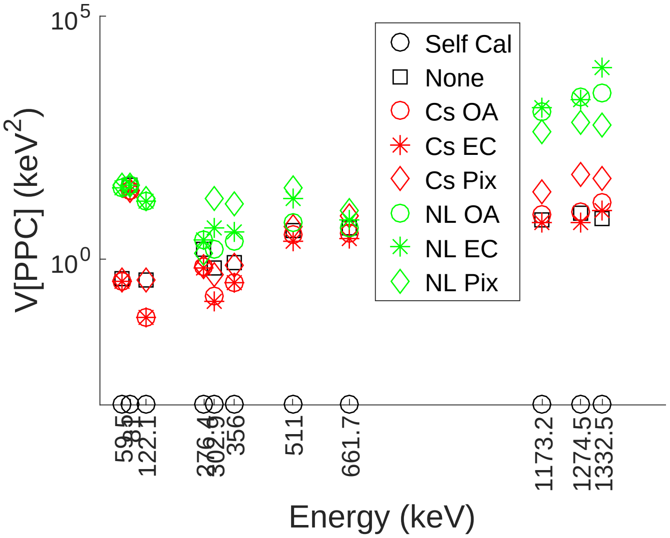

Figure 5.16: Combined centroid variances for each temperature gain correction method applied to nonlinearity measurements taken with common-grid detector as a function of photopeak energy. Self-calibration values are zero by definition and here artificially raised to appear on logarithmic axes.

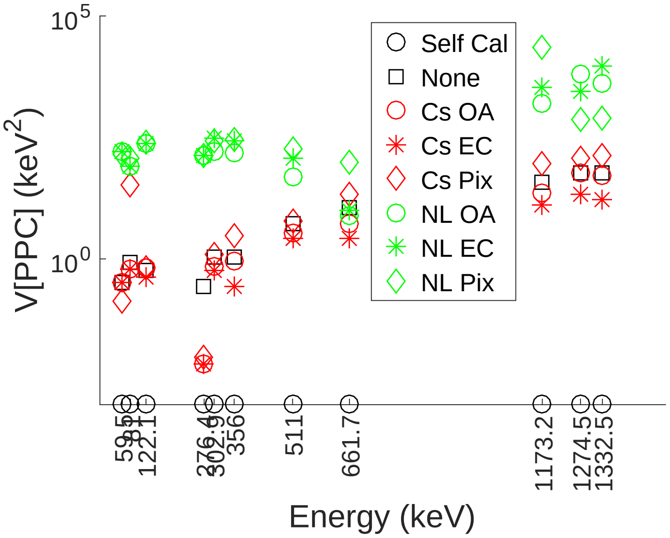

Figure 5.17: Combined centroid variances for each temperature gain correction method applied to nonlinearity measurements taken with simple detector as a function of photopeak energy. Self-calibration values are zero by definition and here artificially raised to appear on logarithmic axes.

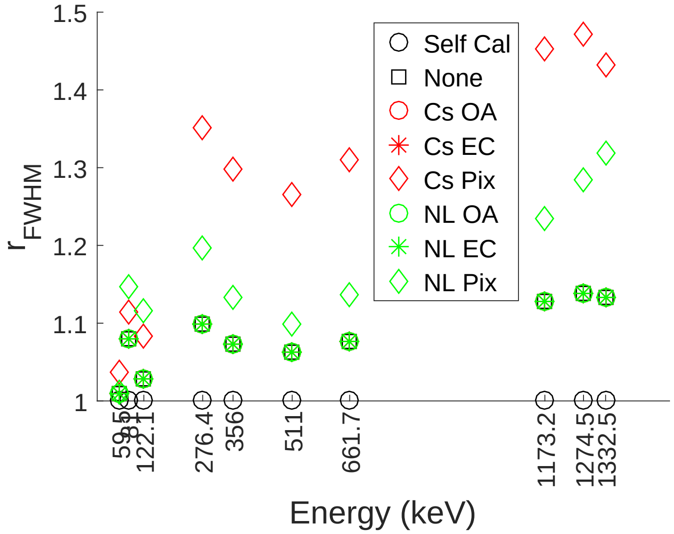

Figure 5.18: Combined resolution ratios for each temperature gain correction method applied to nonlinearity measurements taken with common-grid detector as a function of photopeak energy. Cs-137-only correction data points not visibly apparent are matched and obscured by the corresponding nonlinearity correction data points.

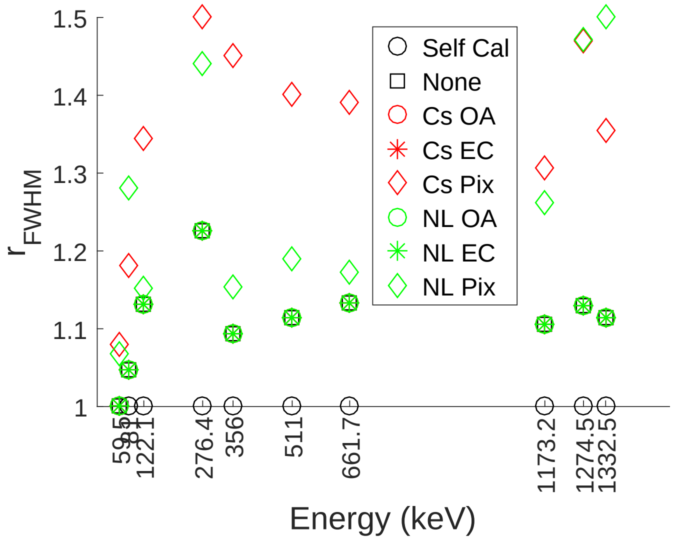

Figure 5.19: Combined resolution ratios for each temperature gain correction method applied to nonlinearity measurements taken with simple-pixel detector as a function of photopeak energy. Cs-137-only correction data points not visibly apparent are matched and obscured by the corresponding nonlinearity correction data points.

5.5.3 Eu-152 Measurements

The analysis applied to the nonlinearity measurements is repeated on the Eu-152 data. The centroid variances are shown individually for each photopeak energy with the common-grid detector in Figure 5.20 and with the simple-pixel detector in Figure 5.21. The resolution ratios are shown individually with the common-grid detector in Figure 5.22 and with the simple-pixel detector in Figure 5.23. For ease of viewing, the combined results were also generated. The combined centroid variances are shown with the common-grid detector in Figure 5.24 and with the simple-pixel detector in 5.25; the combined resolution ratios are shown with the common-grid detector in Figure 5.26 and with the simple-pixel detector in 5.27.

The trends observed in the nonlinearity measurements are mostly repeated here. The Cs-137-only event class correction has the least centroid variance and is the only correction able to improve on the overall resolution across the energy range. The Cs-137-only overall correction shows improved centroid variance with no resolution degradation compared with using no correction. The nonlinearity corrections uniformly have much higher centroid variance than the analogous Cs-137-only measurements. Similarly, the nonlinearity pixelated correction outperforms the other nonlinearity corrections at all energies in the common-grid detector and at energies above 800 keV in the simple-pixel detector.

5.5.4 Ramp Measurements

The best way to test the applicability of the temperature corrections is using them on the temperature ramp measurement. Because this measurement was taken with a single Cs-137 source and because the Cs-137-only corrections consistently outperform the nonlinearity corrections across the entire energy range, only the Cs-137-only corrections are used. Furthermore, the pixelated correction is omitted because of the detrimental effect on resolution. A comparison of the overall photopeak after the two

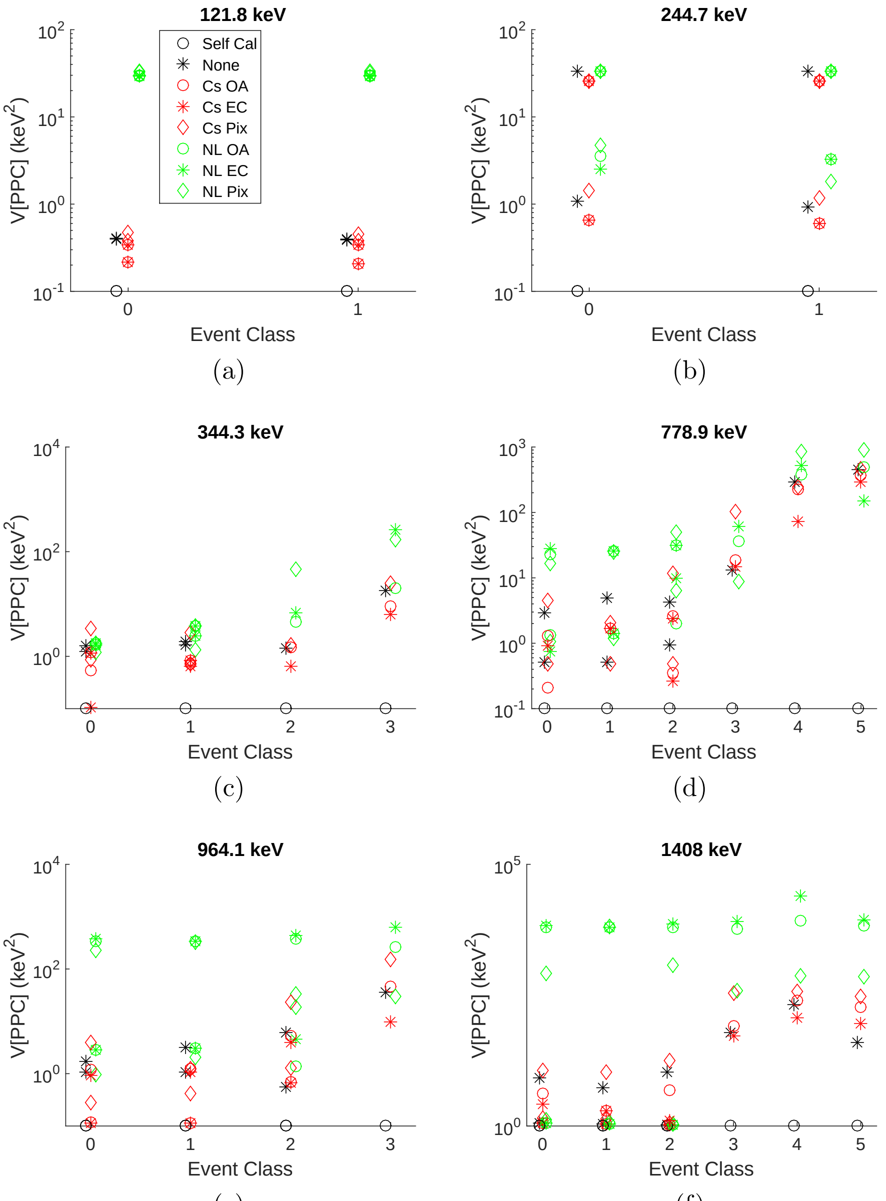

(a) (b) (c) (d) (e) (f)

Figure 5.20: Centroid variances for each temperature gain correction method applied to Eu-152 measurements taken with common-grid detector where subsequent plots correct sequentially increasing photopeak energies. The peaks corrected specifically are 121 keV in (a), 244 keV in (b), 344 keV in (c), 778 keV in (d), 964 keV in (e), and 1408 keV in (f). Self-calibration values are zero by definition and here artificially raised to appear on logarithmic axes.

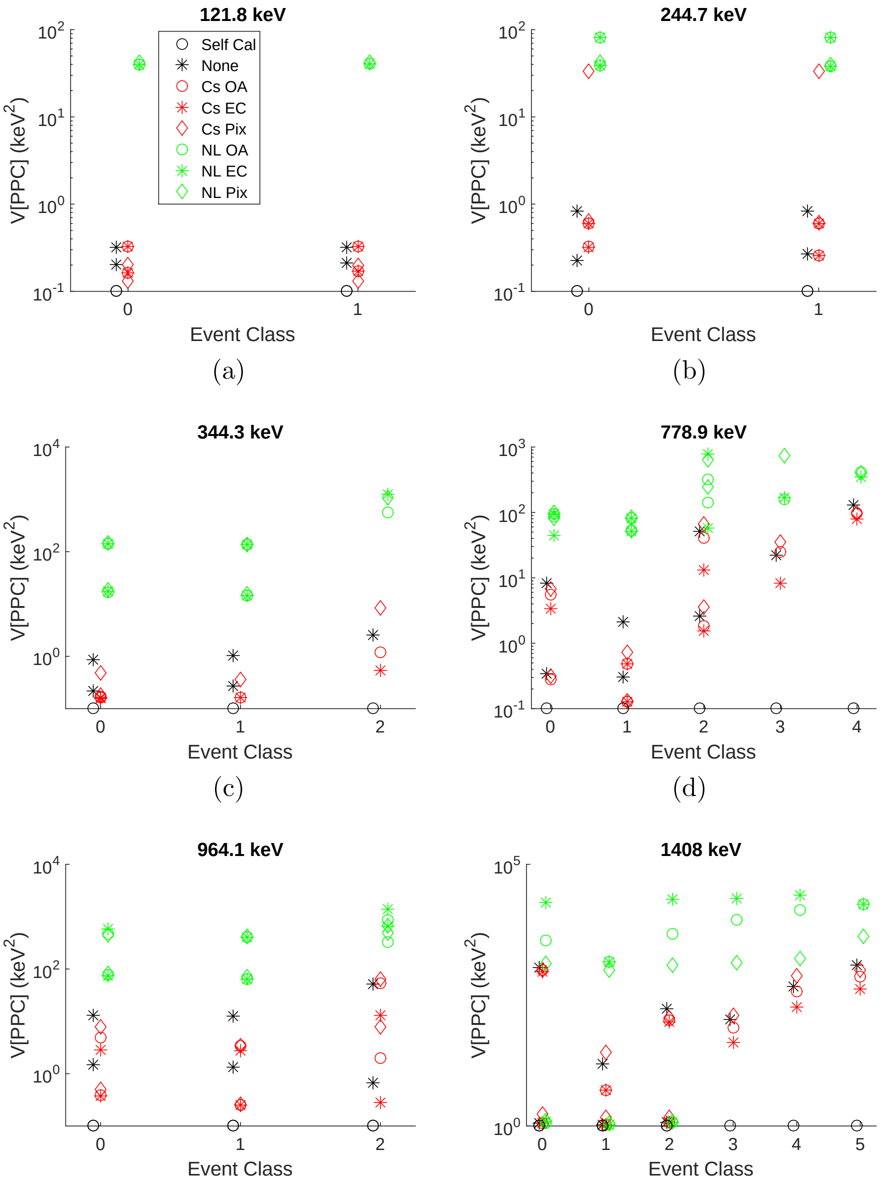

(a) (b)

(c) (d)

(e) (f)

Figure 5.21: Centroid variances for each temperature gain correction method applied to Eu-152 measurements taken with simple-pixel detector where subsequent plots correct sequentially increasing photopeak energies. The peaks corrected specifically are 121 keV in (a), 244 keV in (b), 344 keV in (c), 778 keV in (d), 964 keV in (e), and 1408 keV in (f). Self-calibration values are zero by definition and here artificially raised to appear on logarithmic axes.

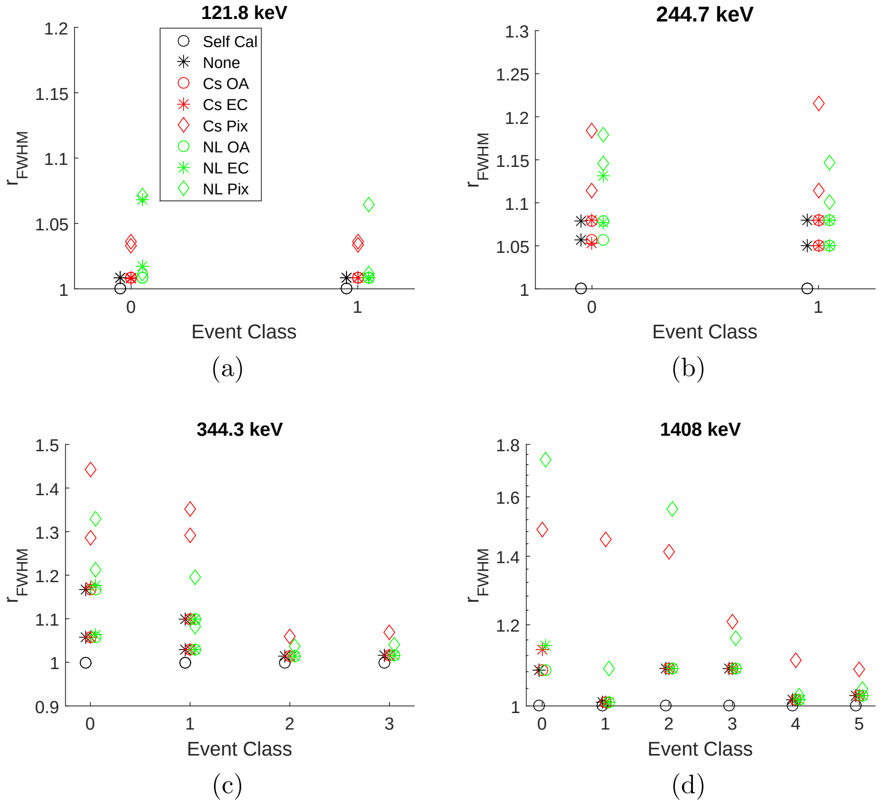

(a) (b)

(c) (d)

Figure 5.22: Resolution ratios for each temperature gain correction method applied to Eu-152 measurements taken with common-grid detector where subsequent plots correct sequentially increasing photopeak energies. The peaks corrected specifically are 121 keV in (a), 244 keV in (b), 344 keV in (c), and 1408 keV in (d).

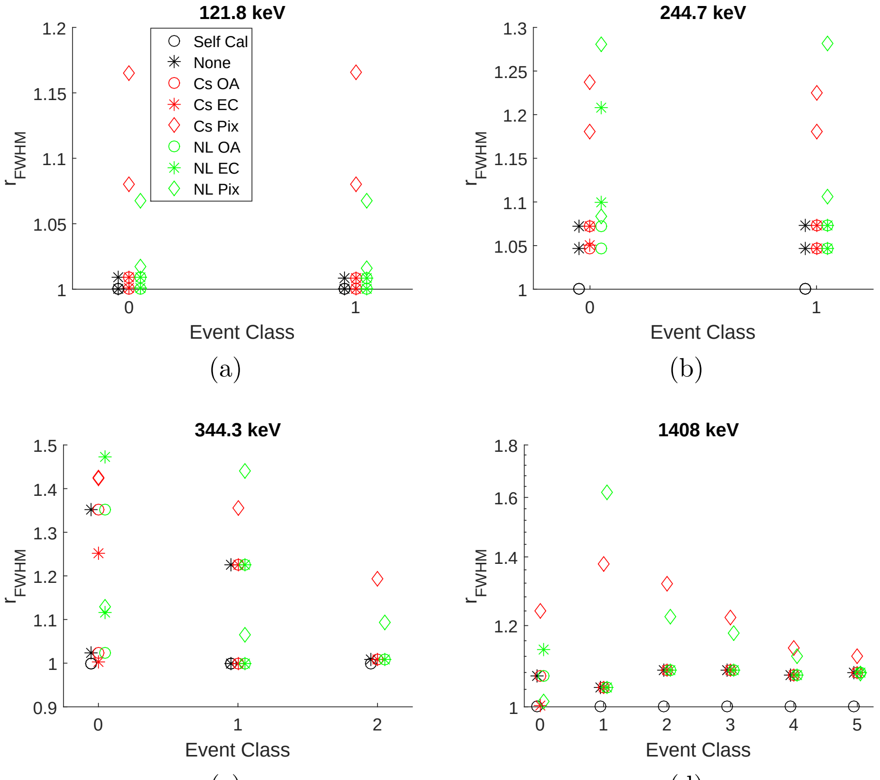

(a) (b)

(c) (d)

Figure 5.23: Resolution ratios for each temperature gain correction method applied to Eu-152 measurements taken with sumple-pixel detector where subsequent plots correct sequentially increasing photopeak energies. The peaks corrected specifically are 121 keV in (a), 244 keV in (b), 344 keV in (c), and 1408 keV in (d).

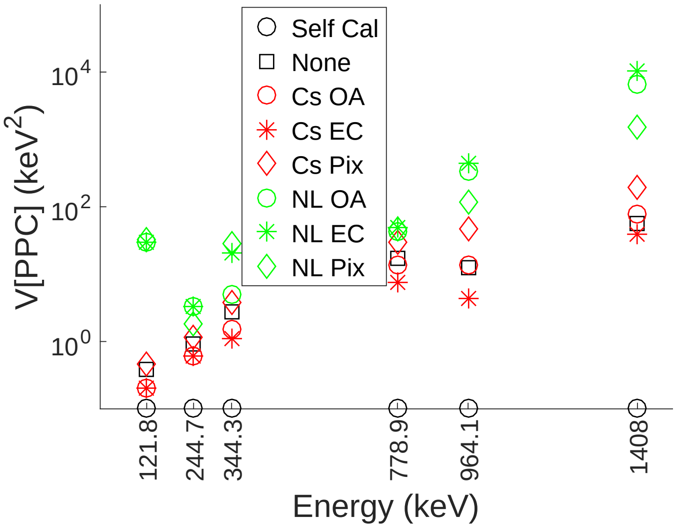

Figure 5.24: Combined centroid variances for each temperature gain correction method applied to Eu-152 measurements taken with common-grid detector as a function of photopeak energy. Self-calibration values are zero by definition and here artificially raised to appear on logarithmic axes.

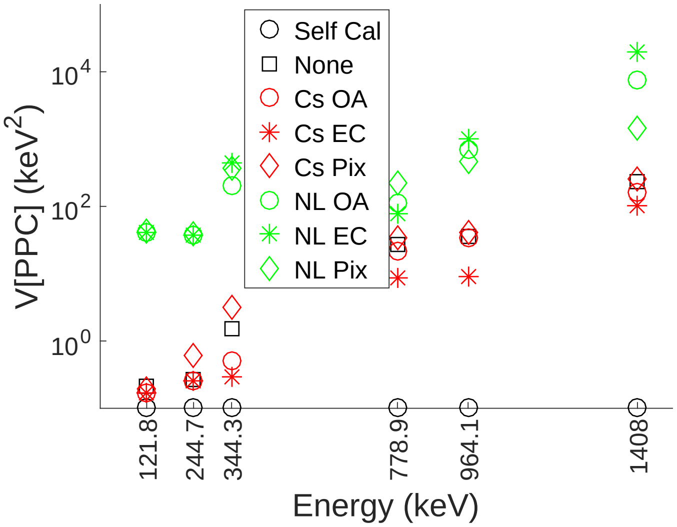

Figure 5.25: Combined centroid variances for each temperature gain correction method applied to Eu-152 measurements taken with simple-pixel detector as a function of photopeak energy. Self-calibration values are zero by definition and here artificially raised to appear on logarithmic axes.

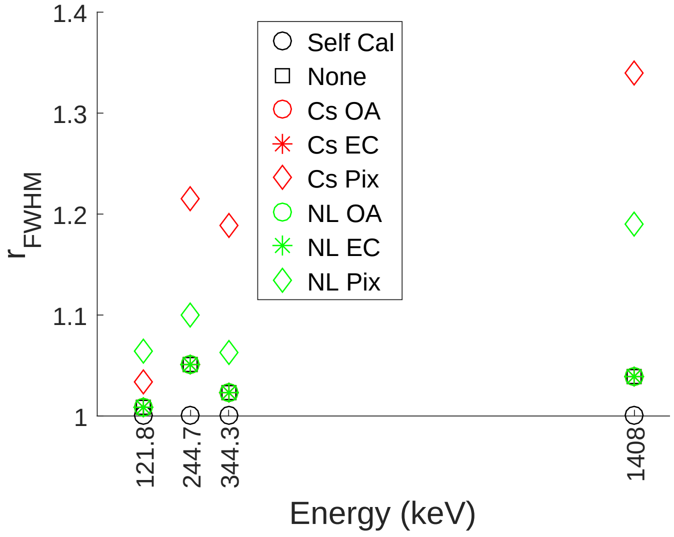

Figure 5.26: Combined resolution ratios for each temperature gain correction method applied to Eu-152 measurements taken with common-grid detector as a function of photopeak energy. Cs-137-only correction data points not visibly apparent are matched and obscured by the corresponding nonlinearity correction data points.

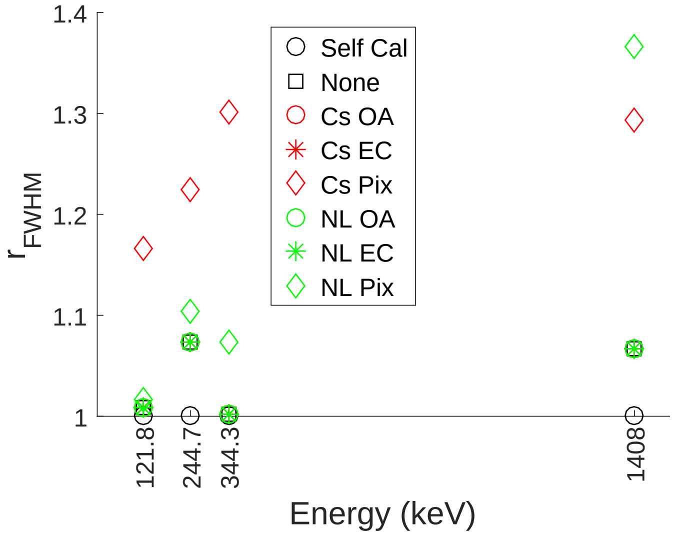

Figure 5.27: Combined resolution ratios for each temperature gain correction method applied to Eu-152 measurements taken with simple-pixel detector as a function of photopeak energy. Cs-137-only correction data points not visibly apparent are matched and obscured by the corresponding nonlinearity correction data points.

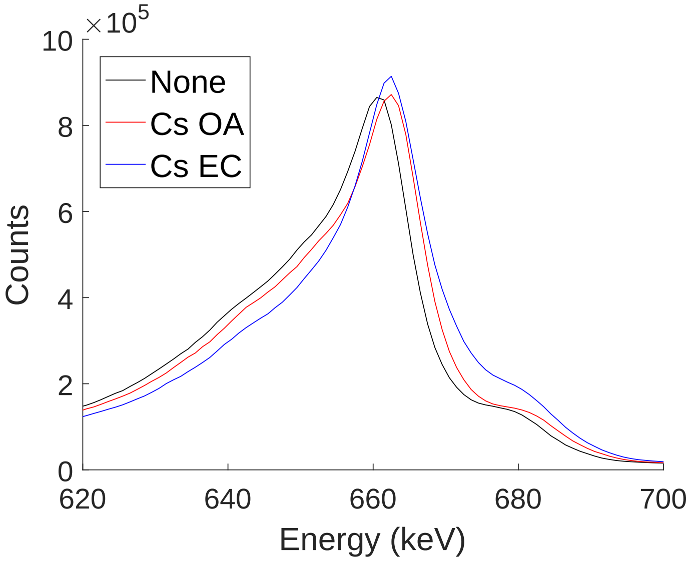

Figure 5.28: Comparison of the overall photopeaks before and after a posteriori gain corrections are applied to Cs-137 temperature ramp measurement.

remaining corrections to the uncorrected photopeak is shown in Figure 5.28.

Without correction, the peak has a centroid at 659.86 keV and 3.11% resolution. The overall correction shifts the centroid to 661.78 keV and slightly improves the resolution to 3.07%, while the event class correction shifts the centroid to 661.86 keV and improves the resolution to 2.58%. The overall resolution can in theory here improve the overall resolution because it is realigning the peaks in different temperature ranges, but in practice it improves it very little, suggesting the difference in photopeak position as a function of temperature by event class exceeds the overall photopeak position as a function of temperature. Additionally, there is a prevalent high energy ledge in the uncorrected spectrum. This obvious artifact isn't affected at all by the overall correction and is only slightly improved by the event-class correction. This suggests it is only partially the result of peak misalignment by event class and requires a more detailed correction to fully correct for it.

5.6 Summary and Future Work

A thorough investigation of the various temperature correction techniques reveals several trends. Across the entire energy range, including the temperature dependence of the energy nonlinearity degrades the resolution and shifts the photopeak further from the correct value. Furthermore, when only accounting for the movement of the Cs-137 photopeak with temperature, a pixel-by-pixel correction similarly degrades the resolution and shifts the photopeak further from the correct value. A single Cs-137 temperature correction shifts the photopeak closer to the target value without degrading the resolution, but a temperature correction for each event class performs better by both metrics. This is seen across the entire energy range for both the common-grid and simple pixel detector.

In terms of implementation, the Cs-137-only event class correction is best. It requires only a single set of nonlinearity measurements taken at the pivot temperature. Furthermore the Cs-137 calibrations taken at other temperatures require far fewer counts because only the overall photopeak is accounted for, not the photopeaks in each pixel or voxel. Finally, because the correction is linear, only measurements at two temperatures are strictly necessary.

Even the ideal gain correction cannot match the self-calibration performance nor fully eliminate spectral artifacts. A more detailed a priori correction that examines the effect of temperature on detector physics must therefore be studied. Additionally, this correction cannot account for events above the highest nonlinearity photopeak with certainty, and time permitting should be repeated with Na-24 to include the entire dynamic range of the detector.

This study included a wide temperature range that would permit drastically reduced temperature regulation, but a fully populated Polaris system with no active cooling can reach 20°C above ambient, corresponding to 45°C in a hot lab. Excessive leakage from the anode to the grid capped the maximum operating temperature of the common-grid detector, but not the simple-pixel detector. Measurements using nonlinearity sources with widely separated photopeaks should be taken at higher temperatures with simple-pixel detectors to establish an upper temperature bound for this correction method. Furthermore, these measurements should be repeated with both detectors at reduced temperatures to establish a lower temperature bound for this correction method. Although this wouldn't permit cooling power reduction, it could improve performance of outdoor detector systems in cold or temperature-varying climates.

CHAPTER VI

Parametric Temperature Correction

6.1 Parametric Correction Testing

Because the temperature gain corrections performed after fixed-temperature calibration cannot match the self-calibration performance when the operating temperature differs from the pivot temperature, an improved temperature correction should take place during fixed-temperature calibration. Rather than simply adjusting the final gain based on an interpolation of expected photopeak positions, individual calibration parameters are interpolated from the fixed-temperature calibrations and are used to correct the raw data. This analysis focuses on three parameters that change the most with temperature and have the most influence on detector performance. The first is the PHD correction because the peak-hold circuitry has a small temperature dependence. The second is the depth deficit correction to correct for the systematic decrease in the calculated depth with decreasing temperature. Relatedly, the final correction is the gain as a function of depth correction, which changes slightly but systematically with temperature.

6.1.1 Peak Hold Drop Correction

As described in 2.2.6, PHD calibrations were performed at each temperature to generate individual corrections for each temperature. Because PHD is a correction to the ASIC gain, the magnitude and temperature trends do not depend on the detector coupled to the ASIC and are expected to be similar for both the ASICs used in the measurement. The raw PHD corrections at each temperature are shown for the ASIC coupled to the common-grid detector in Figure 6.1 and for the ASIC coupled to the simple-pixel detector in Figure 6.2.

The effect of temperature on the PHD correction manifests itself in two ways. First the time of the minimum drop occurs later with rising temperature. This approximates the peaking time, indicates that increasing operating temperature results in a delayed peaking time, and is shown in Figure 6.3. Second the average PHD value changes with rising temperature. The PHD correction is calculated via an artificial test pulse injection covering the entire range of possible peak hold times, but the overwhelming majority of real events occur with a peak hold time between 2.5 and 4 μs. Therefore the average PHD value is calculated for each amplitude using only the values between these two peak hold times, as shown in Figure 6.4. Here uncertainty is the standard deviation of the data points only occurring within the time domain of real events.

In both ASICs, for amplitudes below 3000 ADC units the difference in PHD as a function of temperature is small and has no apparent pattern from one amplitude to the next. Above 3000 ADC units, which corresponds to approximately 1500 keV, there is a clear trend where the average PHD decreases with increasing temperature. This comparatively large change at high amplitudes is deceptively unimportant, however. PHD represents a fixed rather than proportional loss in recorded amplitude. Furthermore although at fixed temperatures it does increase with amplitude, the increase is slower than linear. Consequently, for fixed temperature calibrations, the PHD correction only noticeably impacts the performance for low energy depositions. These trends are more clearly seen by examining the proportional average PHD, where the signal deficit is expressed as a percentage of the peak signal. This is shown in

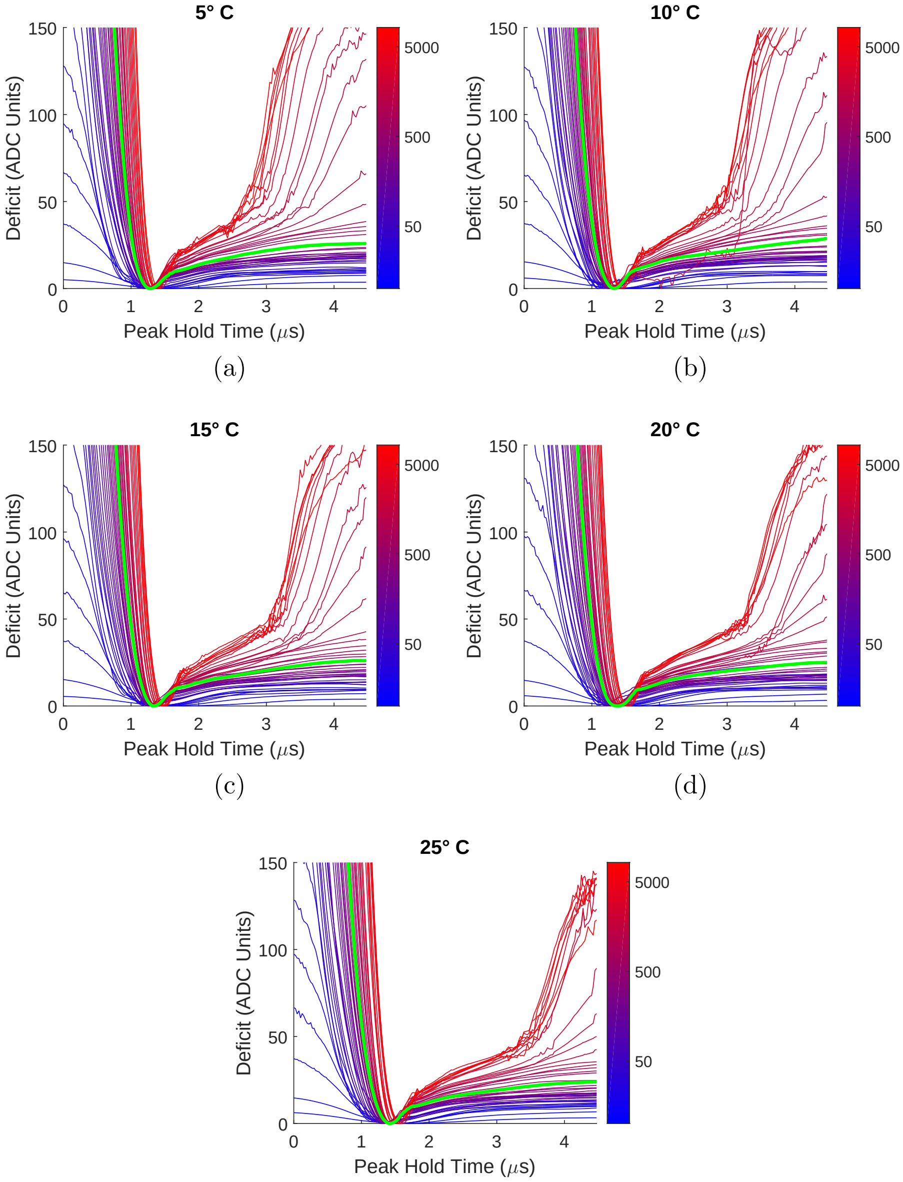

(a)

(b)

(c)

(d)

(e)

Figure 6.1: Peak hold drop for the ASIC coupled with the common-grid detector as a function of peak hold time for amplitudes covering the entire ASIC dynamic range. PHD is shown for 5°C in (a), for 10°C in (b), for 15°C in (c), for 20°C in (d), and for 25°C in (e). The green trends represent the amplitude nearest Cs-137 energy.

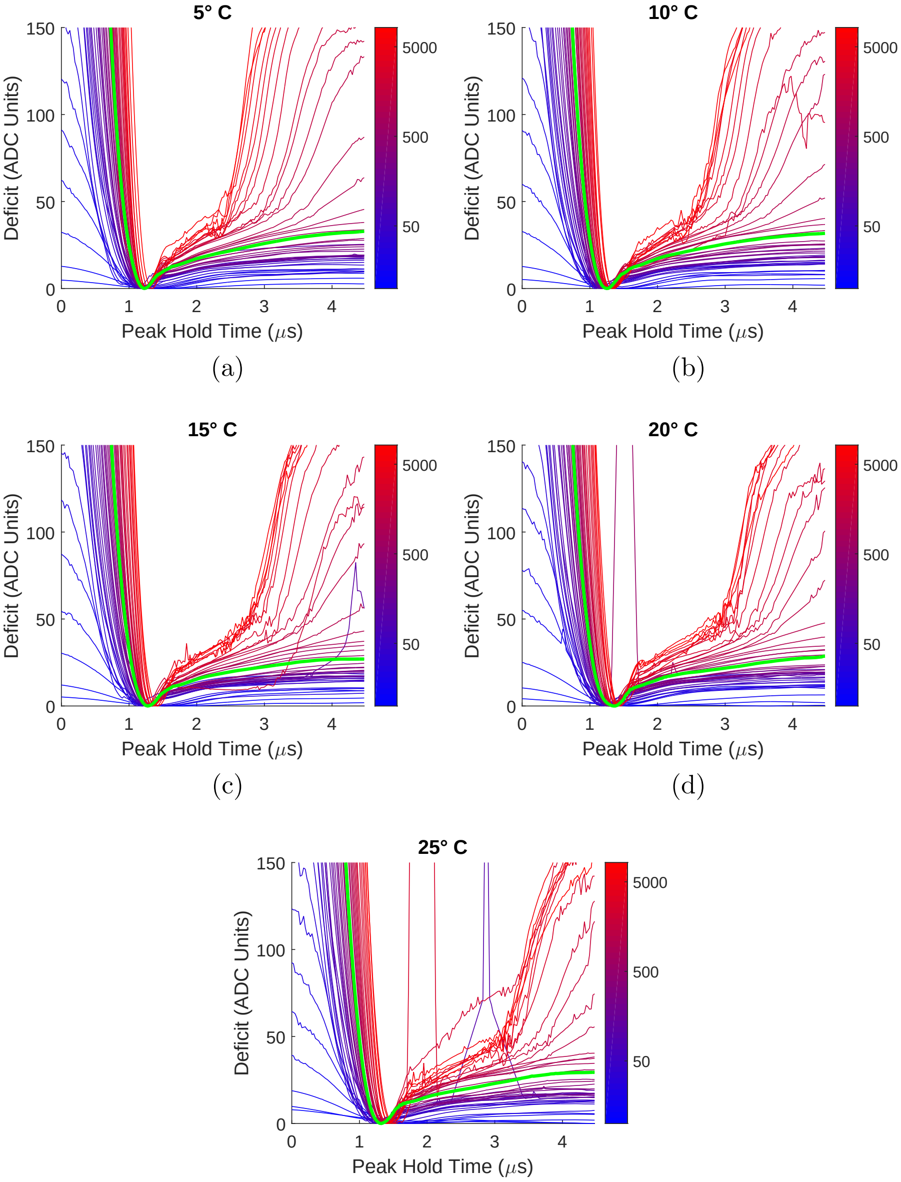

(a) (b) (c) (d) (e)

Figure 6.2: Peak hold drop for the ASIC coupled with the simple-pixel detector as a function of peak hold time for amplitudes covering the entire ASIC dynamic range. PHD is shown for 5°C in (a), for 10°C in (b), for 15°C in (c), for 20°C in (d), and for 25°C in (e). The green trends represent the amplitude nearest Cs-137 energy.

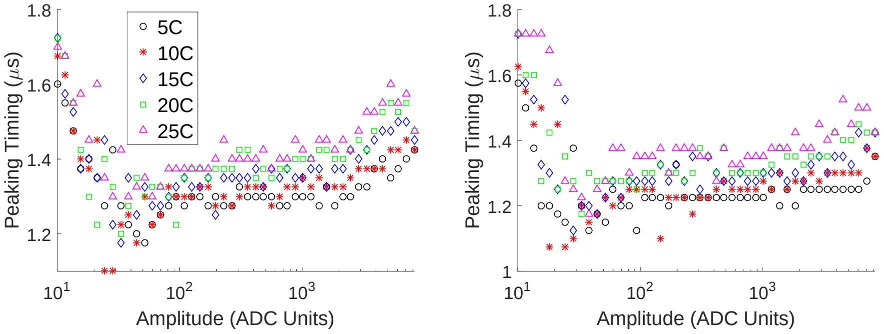

(a) (b)

Figure 6.3: Approximated peaking time for the ASIC coupled to the common-grid detector (a) and for the ASIC coupled to the simple-pixel detector (b) as a function of amplitude for each temperature.

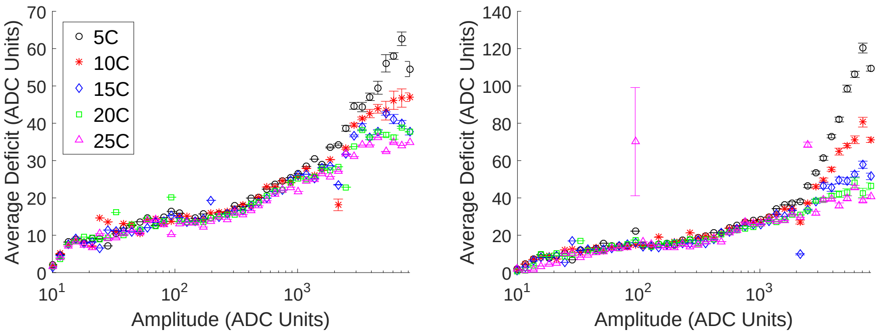

(a) (b)

Figure 6.4: Average PHD over time range of most events for the ASIC coupled to the common-grid detector (a) and for the ASIC coupled to the simple-pixel detector (b) as a function of amplitude for each temperature.

Figure 6.5. Because the PHD correction is ASIC rather than detector dependent, the differences between the two ASICs do not represent a systematic difference between common-grid and simple-pixel detectors. Furthermore, although the data smoothing used by the fixed-temperature PHD correction precludes rigorously quantifying the uncertainty of each data point, the smaller average proportional deficit of the ASIC coupled to the simple-pixel detector at 25°C for low amplitudes cannot be described by uncertainty alone. However, this high-temperature, low-amplitude region represents the operating domain most affected by electronic noise and is likely caused by a small difference in the noise-temperature relationship between the two ASICs.

In addition to being proportionally a larger fixed-temperature correction for low amplitudes, the proportional PHD varies over a larger range with temperature for low amplitudes. This range is expressed as the difference between the average PHD drop values for the highest and lowest temperature calibrations, and is shown in Figure 6.6. By extension, a temperature correction to the PHD is only significant for low energy events. Because the change in PHD as a function of temperature is not systematic at very low amplitudes and is smaller than the width of photopeaks at all other amplitudes, it causes no systematic change in the centroid position with temperature. As a result, a temperature PHD correction will only improve the resolution and will not shift the pivot calibration centroid nearer to the self-calibration centroid.

The temperature adjustment to the PHD correction is implemented analogously to the a posteriori gain corrections. The floating-temperature PHD correction references the fixed-temperature PHD factors at each calibration temperature. On an event-by-event basis, new PHD factors are calculated for the operating temperature by interpolating between the nearest calibration PHD factors, then the fixed-temperature PHD correction is performed on the recorded event using the new PHD factors. The impact of this correction on the Cs-137 energy resolution is shown for the common-grid detector in Figure 6.7 and for the simple-pixel detector in 6.8.

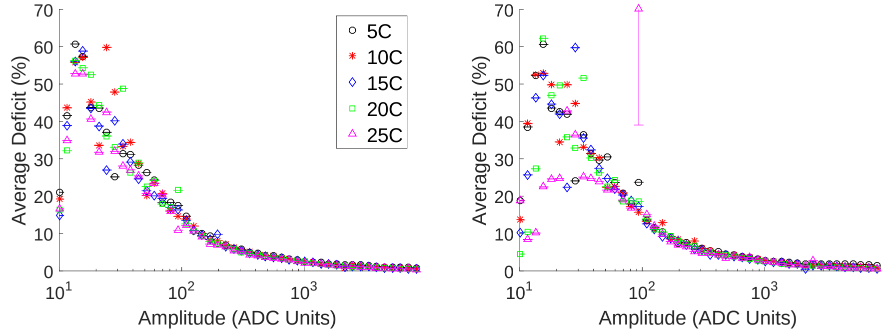

(a) (b)

Figure 6.5: Proportional average PHD over time range of most events for the ASIC coupled to the common-grid detector (a) and for the ASIC coupled to the simple-pixel detector (b) as a function of amplitude for each temperature expressed proportional to peak signal for ease of visualizing diminishing effects of PHD with increasing signal amplitude.

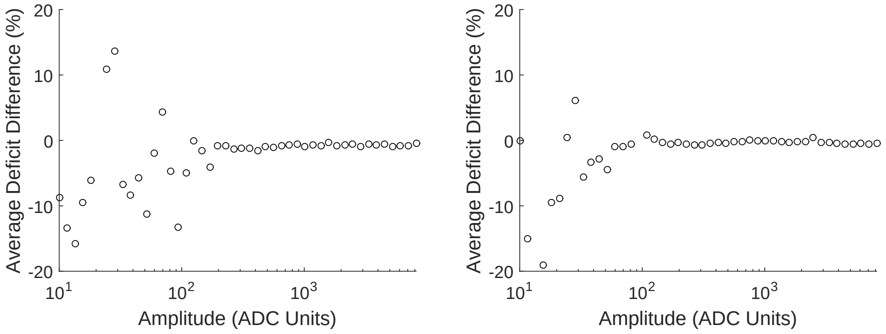

(a) (b)

Figure 6.6: Range of proportional average PHD across temperature calibrations for the ASIC coupled to the common-grid detector (a) and for the ASIC coupled to the simple-pixel detector (b) as a function of amplitude.

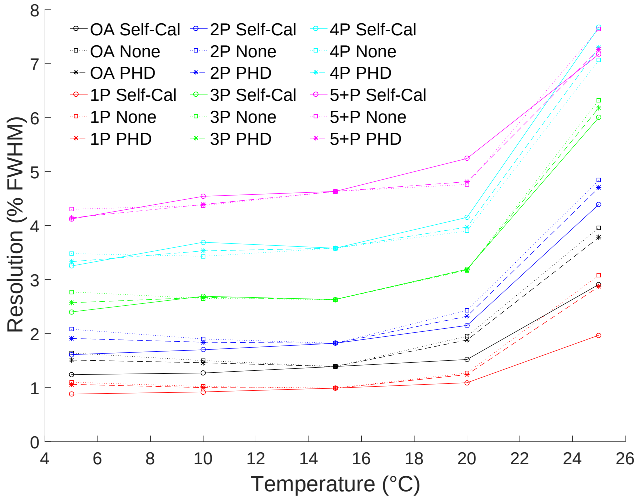

Figure 6.7: Comparison of resolution by event class in common-grid detector between self-calibration, uncorrected pivot-temperature calibration, and PHD-corrected pivot-temperature calibration.

As expected, the PHD temperature adjustment has little impact on large energy depositions. To elaborate, the improvement offered by this adjustment is a strong function of the event class. Single pixel events with 661.7 keV energy deposition per interaction show very little improvement, two pixel events with an average of 330.8 keV show much greater improvement, and five-or-more pixel events with an average below 132.3 keV show such improvement that the PHD temperature-corrected resolution nearly reaches the self-calibration resolution. This correction is therefore important for multi-pixel events, but does not fully account for the performance degradation with temperature of all events.

6.1.2 Depth Deficit Correction

When the spatial position is calculated for each interaction within a detector, the x and y coordinates are determined by the position of the triggered pixel, but the depth coordinate is derived from the ratio of the cathode to anode signal. The cathode spectrum changes with temperature therefore the calculated depth of interaction changes with temperature. The temperature-dependent cathode spectra are shown in

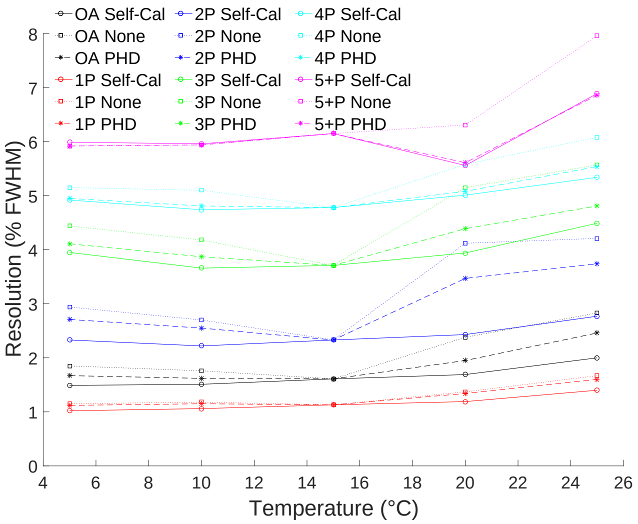

Figure 6.8: Comparison of resolution by event class in simple-pixel detector between self-calibration, uncorrected pivot-temperature calibration, and PHD-corrected pivot-temperature calibration.

Figure 6.9. The larger shifts in the simple-pixel detector cathode spectra are caused by a less uniform electric field in the center of the detector, thus a less linear cathode response and less sharply defined cutoffs. This is a well-known bulk material defect and does not represent a systematic difference between common-grid and simple-pixel detectors.

To measure the impact of changes to the cathode signal on the calculated interaction depth, events from the same dataset were processed twice. For each dataset,

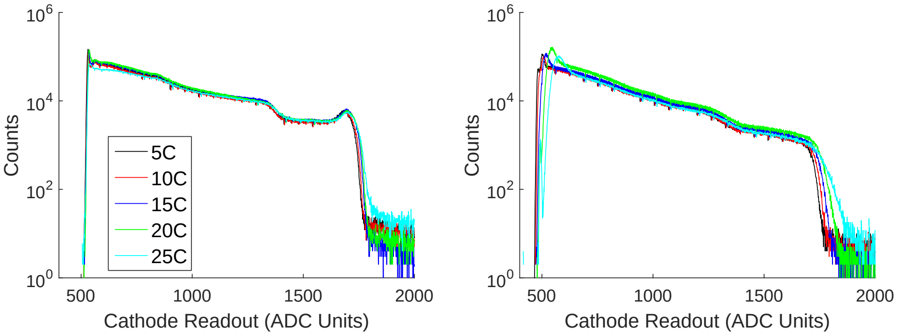

(a) (b)

Figure 6.9: Cathode spectra from the common-grid (a) and simple-pixel (b) detectors for each temperature.

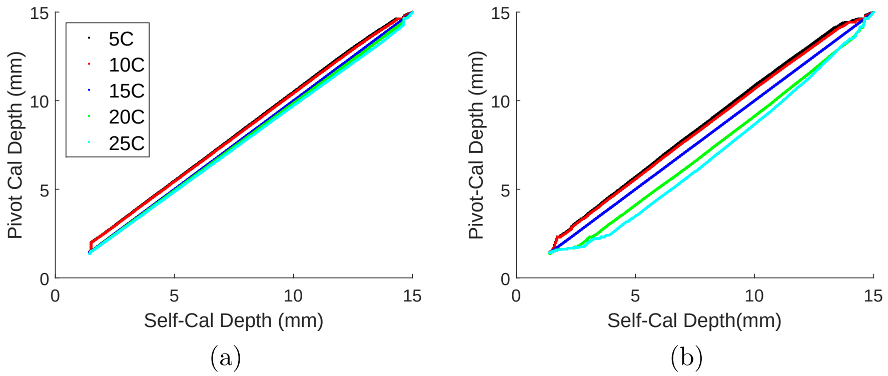

Figure 6.10: Fixed-temperature using pivot calibration reconstructed depth by operating temperature for common-grid (a) and simple-pixel (b) detectors.

the self-calibration depth was found by processing the events using the calibration taken at the same operating temperature, and the pivot-temperature depth was found by processing the events using the calibration taken at the pivot temperature. The depth deficit is then the difference between the self-calibration depth and the pivot-calibration depth. By plotting the pivot-temperature depth against the self-calibration depth, the small magnitude of the change as a function of temperature becomes apparent. This is shown in Figure 6.10. By plotting the depth deficit against the self-calibration depth, the trends with depth and temperature are clearly visible. This is shown in Figure 6.11. Depth is rounded to the nearest 100 μm, as evident in the y-value granularity in Figure 6.11a. Consequently, for each temperature there is a depth deficit correction factor every 100 μm that is calculated by taking the average difference between the self-calibration depth and pivot-calibration depth for all events with the corresponding self-calibration depth. The convergence at cathode surface is caused by the rounding performed by the fixed-temperature depth correction, where events with a corrected CAR above unity are placed at the cathode surface.

In order to correct for depth deficit, the axes of the depth vs. depth plot are flipped and correction factors are binned by pivot-calibration depth for each self-calibration temperature. The corrected depth D_{cor} for a given self-calibration temperature T_{sc}

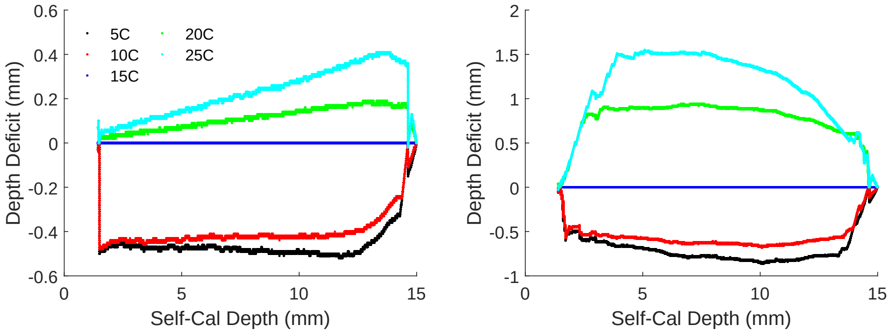

(a) (b)

Figure 6.11: Depth deficit by operating temperature for common-grid (a) and simple-pixel (b) detectors.

is then the sum of the pivot depth D_p and the depth deficit δ, as shown in Equation (6.1).

$$D_{cor}(T_{sc}) = D_{pvt} + \delta(D_p, T_{sc}) \tag{6.1}$$

During operation, for each event the self-calibration corrected depth is calculated for both the nearest self-calibration temperatures above and below the operating temperature, then interpolated based on the operating temperature to determine the final corrected depth. Because the gain changes very little as a function of depth, correcting the depth deficit has a negligible effect on spectroscopic performance. It neither shifts the photopeak centroid nor improves the energy resolution. It does however impact the depth distribution of events, significantly reducing systematic error in the depth reconstruction as a function of temperature. This is best visualized by comparing a histogram of pivot-temperature events by depth before and after depth deficit correction to the self-calibration depth histogram. Using 15°C as the pivot temperature, this is shown for the common-grid detector in Figure 6.12 and for the simple-pixel detector in 6.13.

Because the mean-free path in CZT of 661.7 keV photons is larger than any dimension of the detector crystals used, the events are approximately uniformly distributed

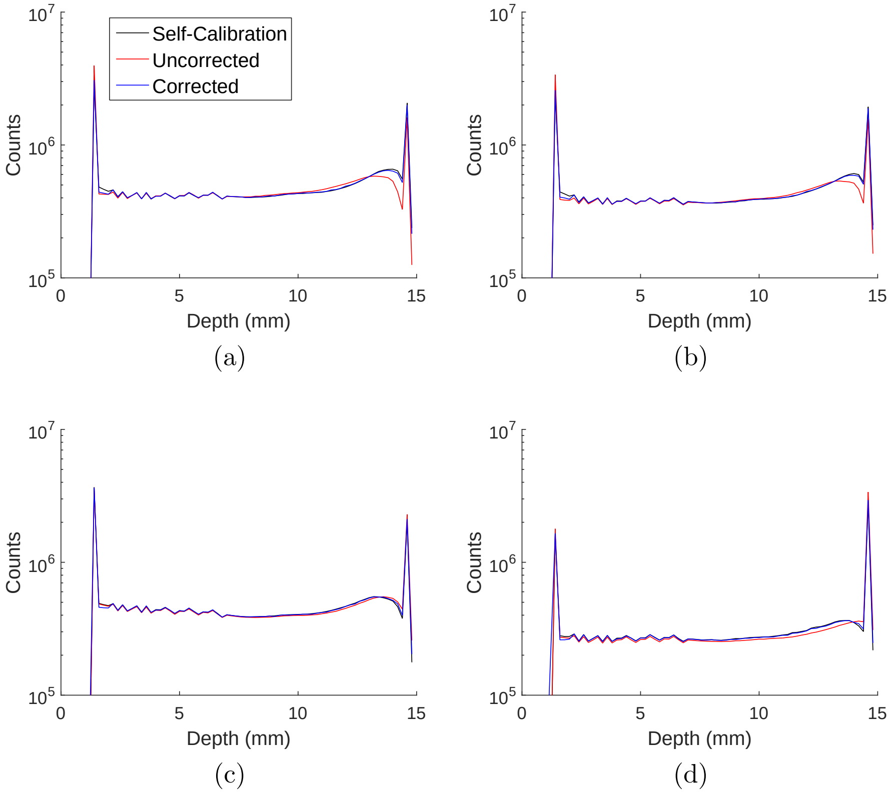

(a) (b)

(c) (d)

Figure 6.12: Effects of depth deficit correction on event depths in common-grid detectors at 5°C (a), 10°C (b), 20°C (c), and 25°C (d).

throughout the detector by depth. Therefore, at intermediate depths events pushed to higher depths by the deficit correction are compensated by events raised from lower depths, and there is little apparent change in the depth profile. The impact of the correction is clear near the electrodes where the depth profile after correction is much closer to the depth profile from self-calibration than from the uncorrected pivot-calibration.

6.1.3 Depth Gain Correction

The gain at each depth also has some temperature dependence. Because the gain in each channel is different, this temperature dependence must be calculated independently for each channel. This precludes easily post-processing the depth-temperature gain relationship analogously to the depth deficit, which is done once

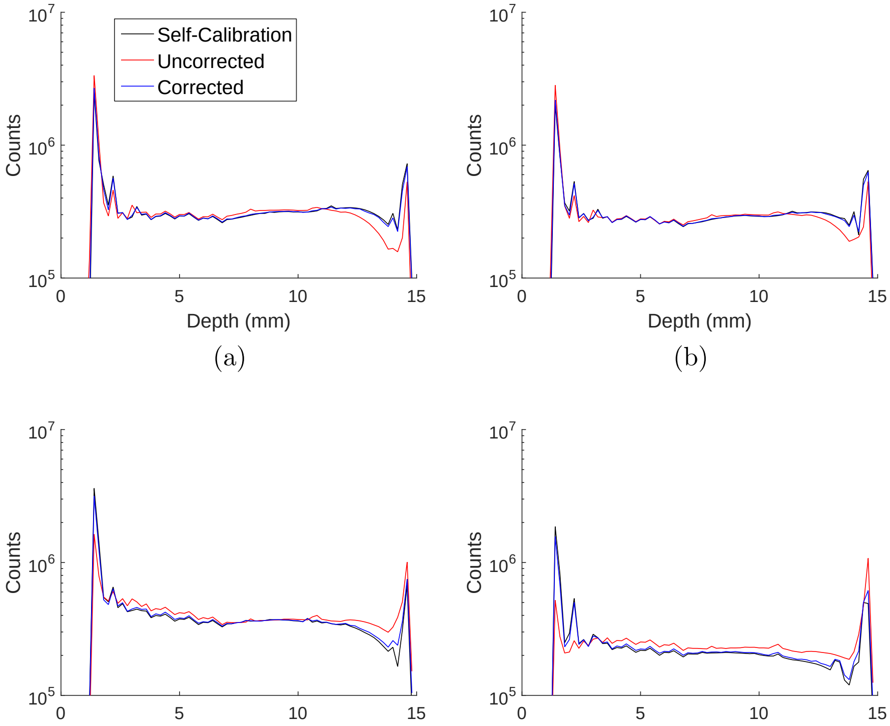

(a) (b)

(c) (d)

Figure 6.13: Effects of depth deficit correction on event depths in simple-pixel detectors at 5°C (a), 10°C (b), 20°C (c), and 25°C (d).

for the entire detector. Fortunately, the necessary data are already collected during fixed-temperature calibration, where the photopeak centroid is calculated in ADC units for each voxel. Using this formulation, the centroid for each channel can be expressed as a function of depth.

Using the self-calibration centroids for each temperature, the temperature dependence of the depth-gain curve can be seen. While there is a clear temperature trend for each pixel, the trend in each pixel is different. To facilitate visualizing these trends, the deviation of the gain at each temperature from the mean gain for all temperatures is calculated as a function of depth. The average of these deviations across all depths larger than 5 mm shows the temperature trend. The depth-gain profiles and averaged trends are shown for a couple apparently linear pixels in Figure 6.14 and for a couple apparently quadratic pixels in Figure 6.15. It is important to note that these trends are not physically meaningful by themselves and only serve to demonstrate the necessity of separate depth corrections for each pixel.

The temperature-centroid dependence is used during operation to convert the incident event deposition from ADC units to energy. Instead of using the centroid from the pivot-temperature calibration, the centroid values from the corrected depth of the nearest self-calibration temperature above and below the operating temperature are interpolated to yield a new centroid value. This interpolated value is used to correct the incident event, and this process is referred to as the temperature-dependent depth gain correction.

Because this process shifts the recorded energy of each event, it changes both the overall centroid position and the overall resolution. However, because the temperature trend in each pixel is different, the overall centroid shift is small. This is confirmed by examining the centroid variance defined in 5.4.1 for the Cs-137 peak before and after correction, as shown for the common-grid detector in Figure 6.16 and for the simple-pixel detector in Figure 6.17. The greater improvement in the common-grid detector

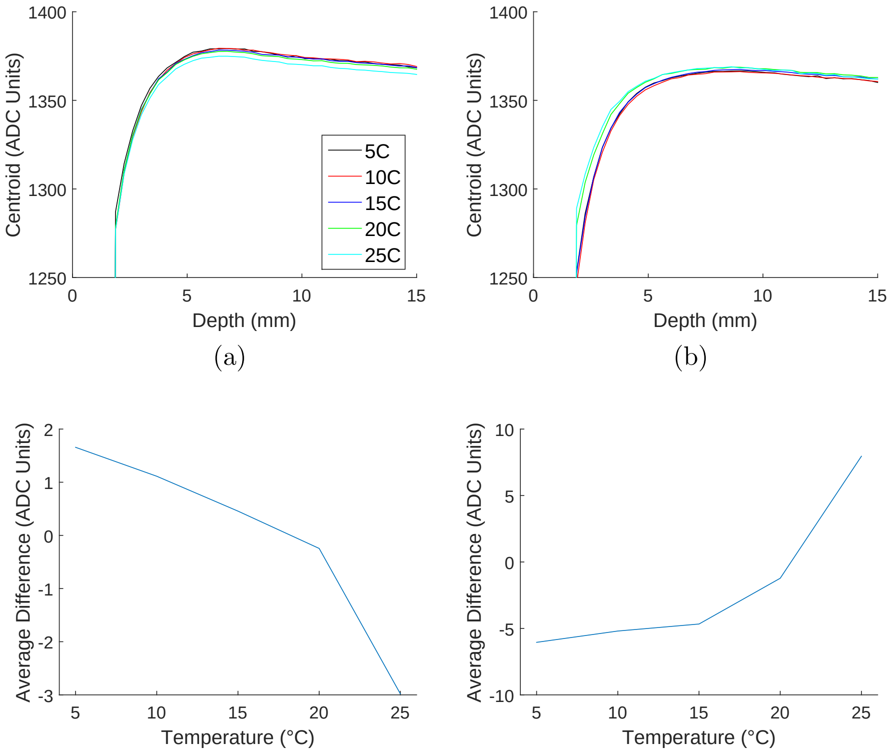

(a)

(b)

(c)

(d)

Figure 6.14: Centroids vs. depth at each self-calibration temperature in the common-grid (a) and simple pixel (b) detectors for pixels with a linear temperature relationship. The averaged difference in the common-grid (c) and simple-pixel (d) pixels highlights how the depth gain trends with temperature.

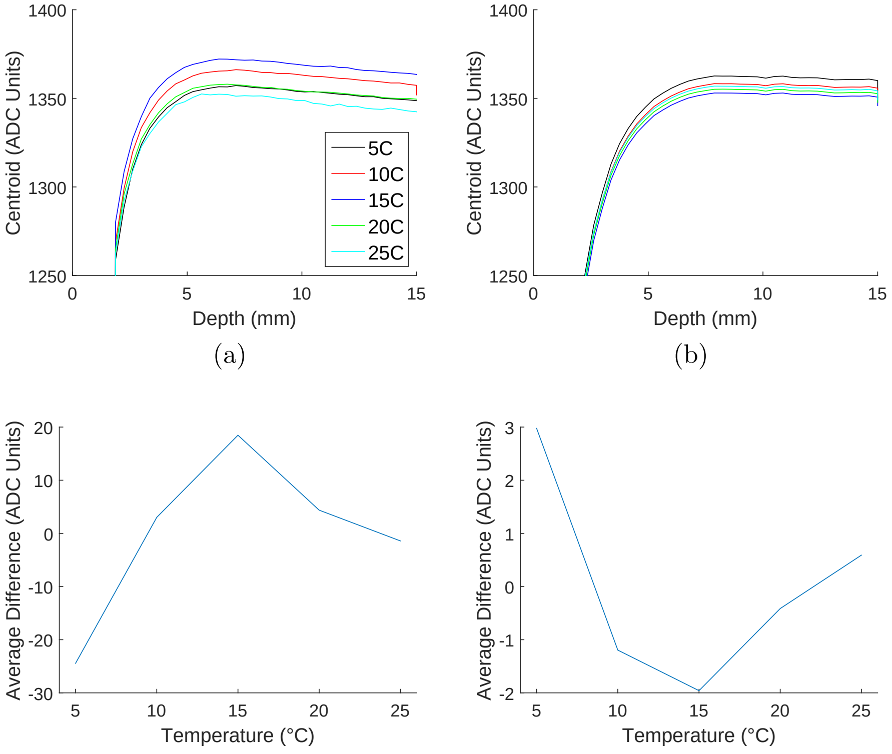

(a) (b)

(c) (d)

Figure 6.15: Centroids vs. depth at each self-calibration temperature in the common-grid (a) and simple pixel (b) detectors for pixels with a quadratic temperature relationship. The averaged difference in the common-grid (c) and simple-pixel (d) pixels highlights how the depth gain trends with temperature.

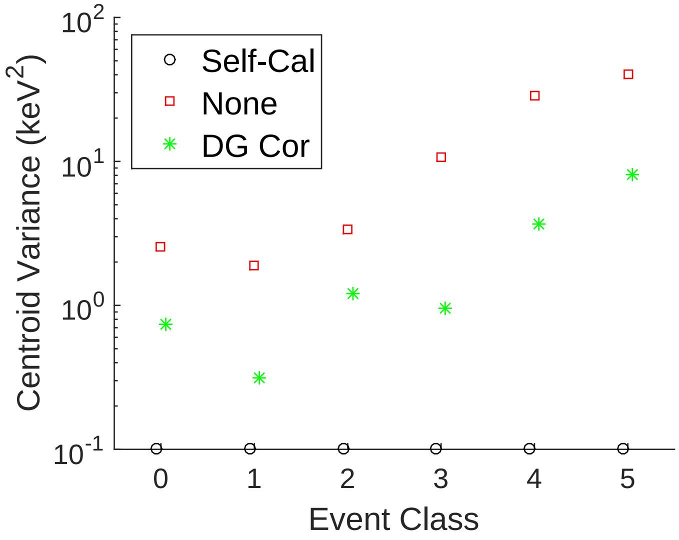

Figure 6.16: Centroid variance for the common-grid detector before and after temperature-dependent depth gain correction. The self-calibration values are by definition zero and are here artificially raised to appear on plot.

is likely caused by the more stable cathode resulting in reduced depth uncertainty for each event, and is not a systematic different between common-grid and simple-pixel detectors.

The most significant impact of the temperature-dependent depth gain correction is on the resolution improvement. Shown for the common-grid detector in Figure 6.18 and for the simple-pixel detector in Figure 6.19, this correction significantly improves the resolution for every event class. While the improvement is reduced at 25°C, at and below 20°C this correction nearly recovers the self-calibration performance.

6.1.4 Performance Impact on Ramp Measurements

The general applicability of the parametric temperature corrections is gauged by testing them on the temperature ramp measurement. A comparison of the corrected and uncorrected overall photopeaks is shown in Figure 6.20. Because the parametric corrections shift the centroid very little, a Cs-137-only event-class a posteriori gain correction is also applied to properly position the photopeak.

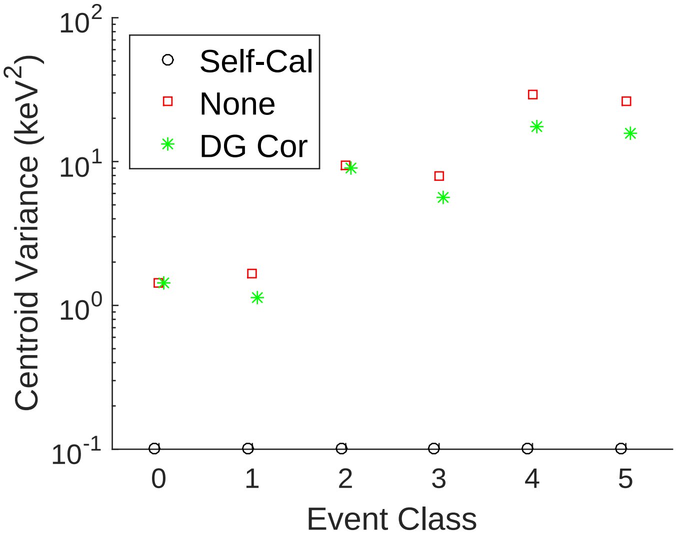

Figure 6.17: Centroid variance for the simple-pixel detector before and after temperature-dependent depth gain correction. The self-calibration values are by definition zero and are here artificially raised to appear on plot.

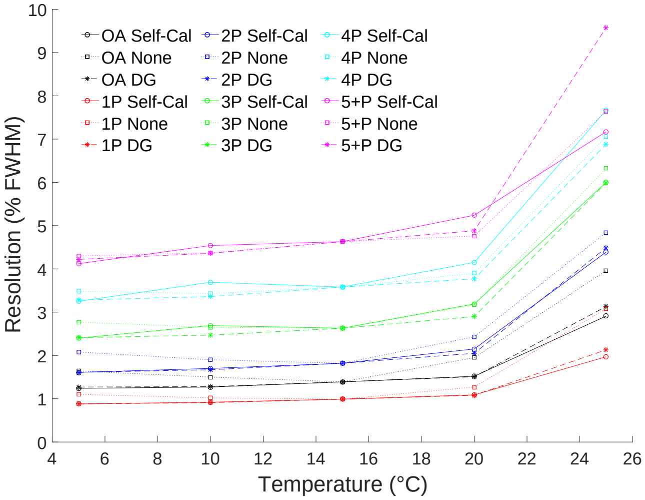

Figure 6.18: Comparison of resolution by event class in common-grid detector between self-calibration, uncorrected pivot-temperature calibration, and depth gain-corrected pivot-temperature calibration.

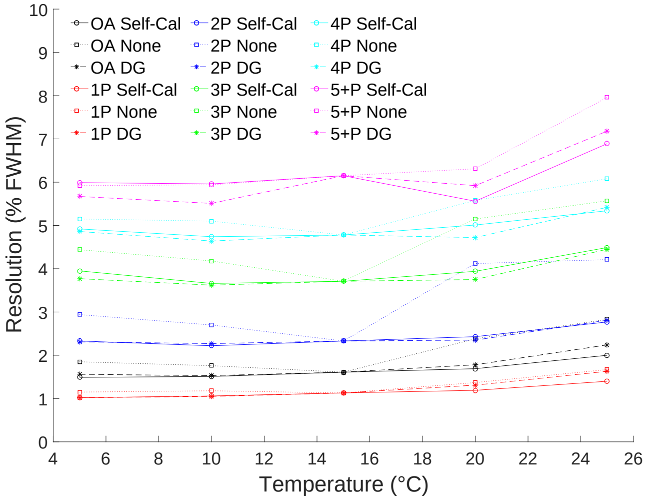

Figure 6.19: Comparison of resolution by event class in simple-pixel detector between self-calibration, uncorrected pivot-temperature calibration, and depth gain-corrected pivot-temperature calibration.

Without correction, the peak has a centroid at 659.86 keV and 3.11% resolution. The parametric corrections alone improve the resolution to 1.67% but only shifts the centroid to 660.04 keV. By utilizing the a posteriori gain correction, the centroid is repositioned to 661.78 keV and the resolution is improved slightly to 1.66%. Additionally, the parametric corrections remove the high-energy ledge feature and reduce the low energy tail. These corrections are sufficient to recover most system performance and eliminate temperature-induced spectral artifacts.

6.2 Required Data Minimization

The temperature corrections as implemented in sections 5.3 and 6.1 are effective, but require a large amount of data. A full calibration is needed at each temperature, and includes a voxel-wise Cs-137 calibration, a PHD calibration, and energy nonlinearity calibrations. The measurement times for each of these scale linearly with the number of detectors involved, except for the PHD measurement which is done in parallel for up to six detectors at a time and the optional Na-24 measurement which is

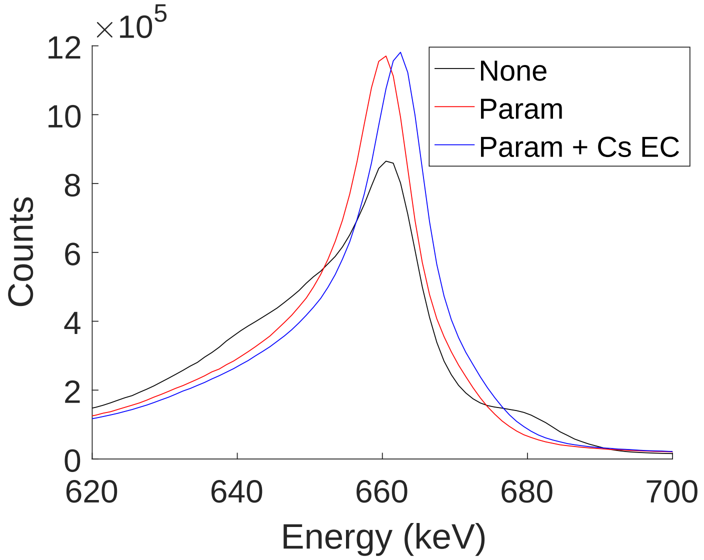

Figure 6.20: Comparison of the overall photopeaks before and after parametric corrections are applied to Cs-137 temperature ramp measurement.

done in parallel for a plane of nine detectors. The calibration times are broken down in Table 6.1. Neglecting equilibration time after changing the temperature before colltecting data, a full calibration can be taken for a single detector in nine hours. For the entire system, each temperature requires just under a week without the Na-24 calibration, and more than two weeks with it.

Binning temperature coarsely and taking calibrations every 5 °C, it would require more than two months to calculate the temperature corrections for an array system. This is prohibitively long for a practical field instrument and necessitates a reduction in calibration times. This is accomplished first by determining the separability of temperature effects from other parameters. Although temperature alters the centroid photopeak as a function of depth, if the effects of depth and temperature are separable then only a single voxel-wise Cs-137 calibration at the pivot temperature is necessary and a depth-averaged Cs-137 calibration requiring far less data can be used at all other calibration temperatures. Similarly, temperature-PHD separability would necessitate a full PHD calibration at the pivot temperature and a PHD reading for only a single amplitude at each other temperature. Finally, temperature-nonlinearity separability

Table 6.1: Full Calibration Times

Measurement		Single Detector Time (hr:min)	18 Detector Array Time (hr:min)
PHD		0:20	2:00
Voxel-wise Cs-137		4:00	72:00
NL	Cs-137	0:40	12:00
	Ba-133	0:20	6:00
	Na-22	1:20	24:00
	Co-57	0:10	3:00
	Am-241	0:10	3:00
	Co-60	2:00	36:00
	Na-24	96:00	192:00
Total	w/o Na-24	9:00	158:00
	w/ Na-24	105:00	350:00

would require a full nonlinearity calibration at only the pivot temperature and only a single energy measurement at each other temperature. A depth-averaged Cs-137 measurement would fulfill this single-energy requirement, and could potentially be used in both the temperature dependent depth correction and nonlinearity correction.

6.2.1 Determining Separability

Separability is quantified via SVD, which is an eigenvalue decomposition generalized for a rectangular matrix[73]. This factorization expresses the $m \times n$ original matrix $\boldsymbol{M}$ as the product of $m \times m$ left singular matrix $\boldsymbol{U}$, the $m \times n$ diagonal matrix $\boldsymbol{\Sigma}$, and the $n \times n$ right singular matrix $\boldsymbol{V}$ conjugate transpose, as expressed in Equation (6.2).

$$\boldsymbol{M} = \boldsymbol{U}\boldsymbol{\Sigma}\boldsymbol{V}^* \tag{6.2}$$

There are then $N = \min(m, n)$ singular values σ_i built from the diagonal elements of $\boldsymbol{\Sigma}$ in descending order and shown in Equation (6.3). The corresponding columns from each of the singular matrices are then referred to as the left and right singular vectors $\boldsymbol{U}_i$ and $\boldsymbol{V}_i$. The outer product of these singular vectors yields a decreasing series of $m \times n$ matrices $\boldsymbol{A}_i$ that then sum to the original matrix, as expressed in Equation (6.4).

$$\boldsymbol{\sigma} = \text{sortmax}\big(\text{diag}(\boldsymbol{\Sigma})\big) \tag{6.3}$$

$$\boldsymbol{M} = \sum_{i}^{N} \boldsymbol{A}_i = \sum_{i}^{N} \sigma_i \boldsymbol{U}_i \otimes \boldsymbol{V}_i^* \tag{6.4}$$

Because each outer-product matrix is separable, if the first outer-product matrix can fully express the original matrix such that $\boldsymbol{M} = \boldsymbol{A}_1$, then the original matrix represents separable data. This is quantified by defining the index of separability α, shown in Equation (6.5), as the ratio of the first singular value squared to the sum of all singular values squared. A value of unity indicates perfect separability while a value less than unity indicates correlation. Real data subject to statistical variation will never have an index of separability of exactly unity, however a small deviation from unity means the data can be accurately approximated by a separable model[74].

$$\alpha = \frac{\sigma_1^2}{\sum_i \sigma_i^2} \tag{6.5}$$

To illustrate this comparison, consider two functions of independent variables x and y. First is the separable equation $z = (x + 1)y^2$, second is the non-separable equation $z = (x+y)^2$. The original matrices are then the evaluation of each equation over a domain of inputs from -10 to 10 for each variable. The index of separability for the first equation is exactly equal to unity, and the original data can be perfectly reconstructed from the first outer product matrix, as shown in Figure 6.21. The index of separability for the second equation is 0.5708, which is very far from unity and indicates that a separable model very poorly approximates the underlying function. This is confirmed in Figure 6.22, where the difference between the original and

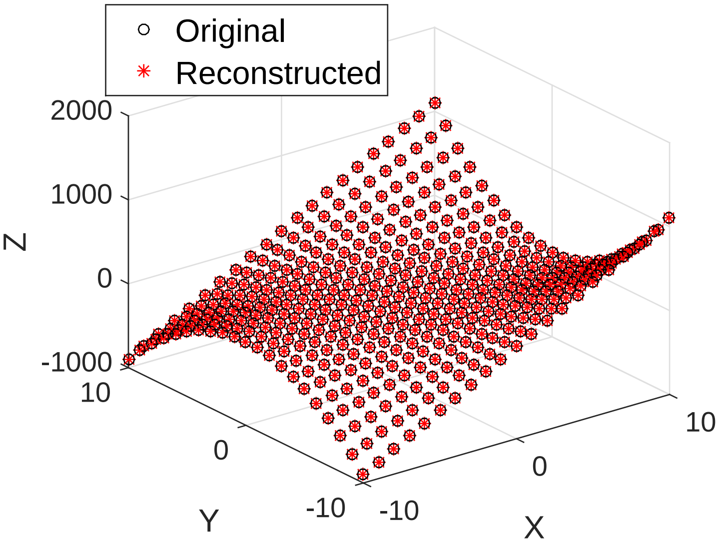

Figure 6.21: Original and reconstructed data from SVD first outer product matrix for separable function.

reconstructed data is visibly large.

6.2.2 Peak Hold Drop Separability

In each detector, the PHD temperature correction is stored as a three-dimensional array of data, with peak-hold time on one axis, raw amplitude on the second, and temperature on the final axis. In an effort to separate the effects of amplitude from the effects of temperature, a two-dimensional matrix is considered independently for each time bin. An SVD is then performed on each of these matrices, where the rows correspond to the calibration temperature, the columns correspond to the raw amplitude, and the values are the magnitudes of the peak-hold drop. The deviations of the indices of separability from unity are shown for each time bin in Figure 6.23.

Because PHD is an ASIC rather than detector property, the separability by time looks similar for both. The separability is very poor for peak-hold times below 1.5 μs, where the peak-hold time approximates the peaking time. This indicates an inseparable temperature and amplitude dependence of the peaking time, but doesn't accurately reflect normal peak-hold time. During operation, almost all events are

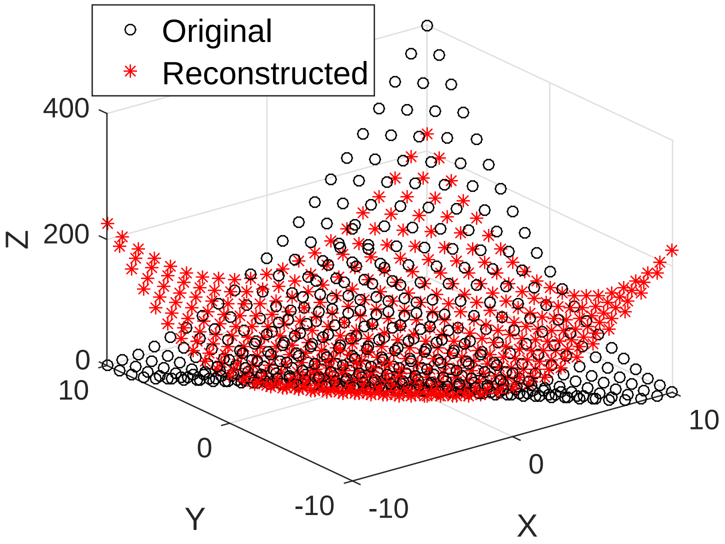

Figure 6.22: Original and reconstructed data from SVD first outer product matrix for non-separable function.

recorded with a peak-hold time between 2.5 and 4 μs, as highlighted by the blue vertical bars. In this restricted time domain, the indices are very near unity, suggesting a separable model is a good approximation for both detectors. This is confirmed in Figure 6.24, where original PHD data at each calibration temperature is plotted against the PHD data reconstructed from the first outer product matrix for a representative time bin in the common-grid detector with little difference between them. This difference is shown explicitly in Figure 6.25, where the magnitude is small but clearly trends with temperature and for small amplitudes does not fall within uncertainty. The temperature trend indicates residual temperature dependence and that the separable model is imperfect, but the small magnitude confirms the separable model is a good approximation.

The first left singular vector represents the PHD temperature dependence in a separable model, and has a value for each calibration temperature. To test the spectroscopic effects of assuming PHD separability, only the pivot-temperature PHD is considered. Rather than interpolating PHD values based on the operating temperature, values of the first left singular vector are interpolated. The pivot-temperature

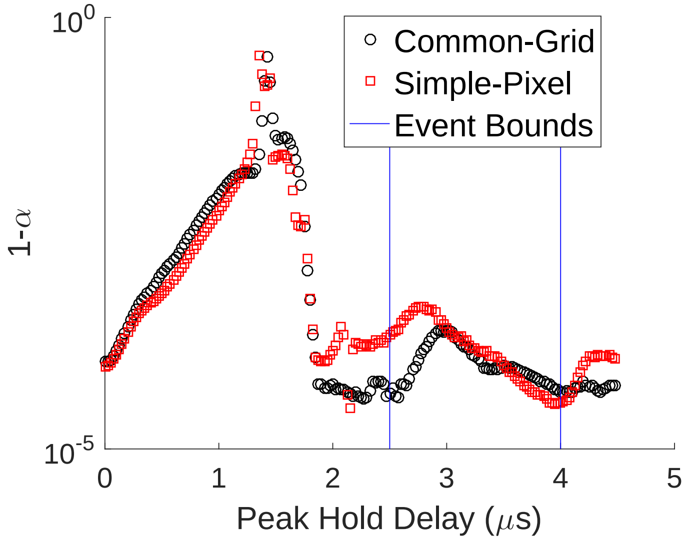

Figure 6.23: Deviations of the indices of separability from unity by peak hold time for PHD SVD.

PHD values are then adjusted by the ratio of the operating-temperature to pivot-temperature first left singular vector values, then the fixed-temperature PHD correction is performed.

This formulation is a test of separability. It isn't practical for data reduction because although it requires much less data during operation, it still requires a full PHD correction dataset at each calibration temperature for the a priori left singular vector calculation. To gauge a practical implementation of PHD separability, the first left singular vector is approximated by the values of the amplitude line corresponding to 661.7 keV normalized by the value at the pivot temperature. Because the first left singular vector is calculated from all amplitudes, it is different from the single-amplitude estimated vector, but because temperature and amplitude are separable it is a good approximation. The spectroscopic performance is tested identically, and a comparison of the full PHD, SVD PHD, and estimated SVD PHD resolutions are shown for the common-grid detector in Figure 6.26 and for the simple-pixel detector in Figure 6.27.

There is some performance degradation caused by assuming temperature and am-

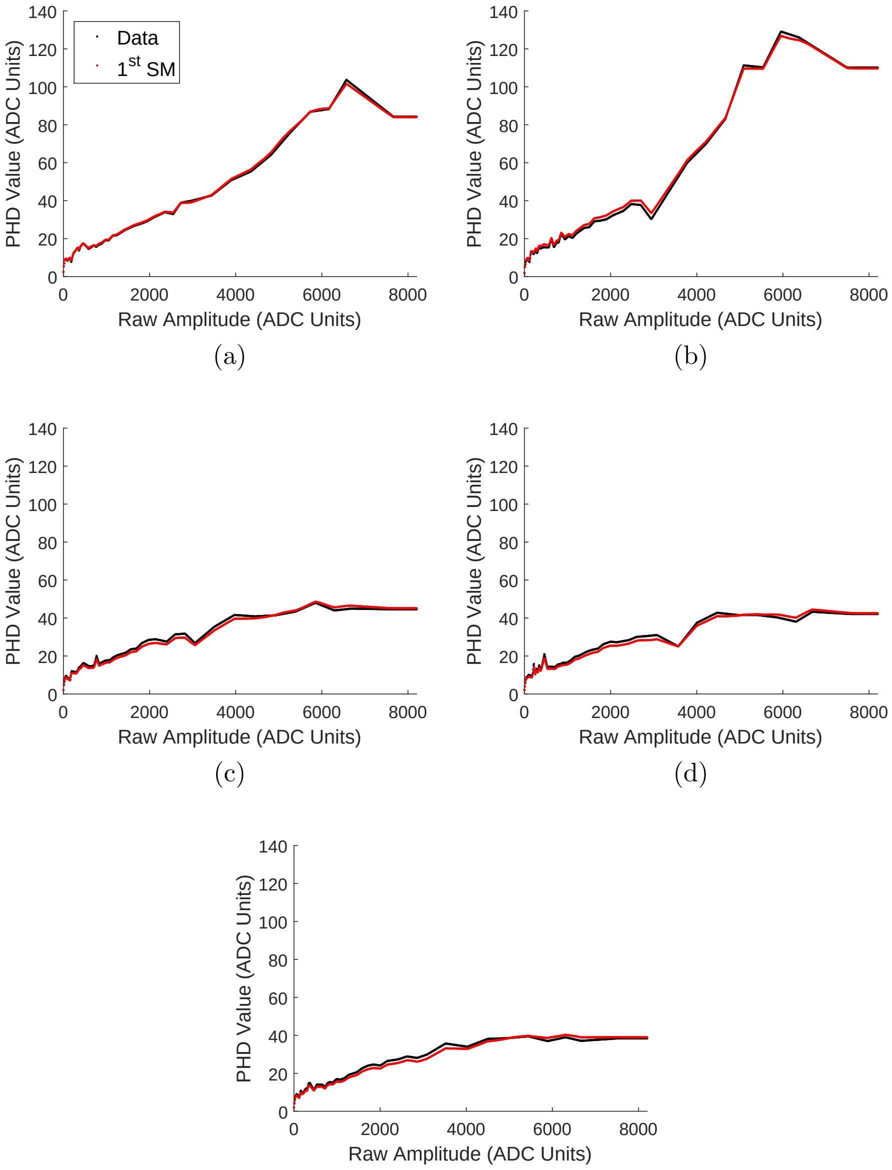

(a)

(b)

(c)

(d)

(e)

Figure 6.24: Original and reconstructed data taken at 5°C (a), 10°C (b), 15°C (c), 20°C (d), and 25°C (e) with ASIC mounted to common-grid detector PHD SVD at peak-hold time 3.125 ns.

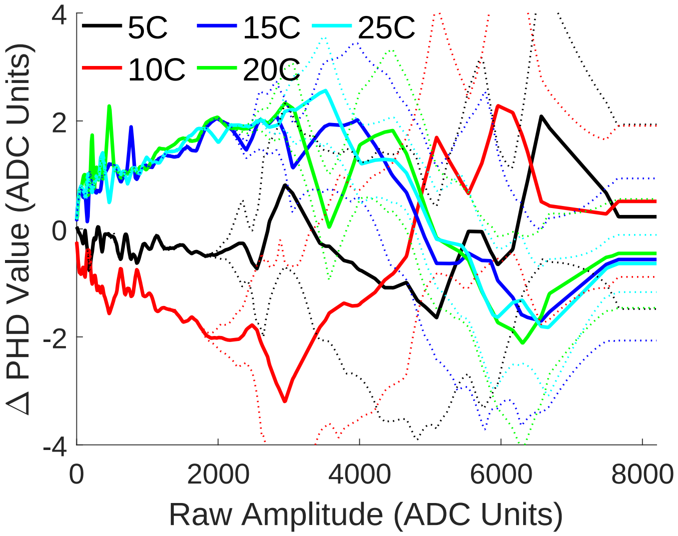

Figure 6.25: Deviation of PHD SVD reconstructed data from original PHD data taken at each temperature with data shown by solid lines and uncertainty bounds shown by dashed lines.

plitude separability in the PHD data, but this degradation is very small. There is further degradation estimating the left-singular vector with a single amplitude, but once again this degradation is slight. Furthermore, the performance is still substantially improved compared with no PHD temperature correction. In accepting this slight performance degradation, a full PHD calibration must only be taken at the pivot temperature, and PHD data must be collected for only a single amplitude at all other calibration temperatures. This process, even for an array system, takes less than one minute, and represents a significant time savings.

6.2.3 Depth Deficit Separability

In each detector, the depth deficit is a two-dimensional array of data with temperature on one axis and depth on the other. This array is then assigned to a matrix where the rows correspond to calibration temperature, the columns correspond to the self-calibration depth, and the values are equal to the depth deficit. Performing an SVD on this matrix yields a deviation from unity in the index of separability for the

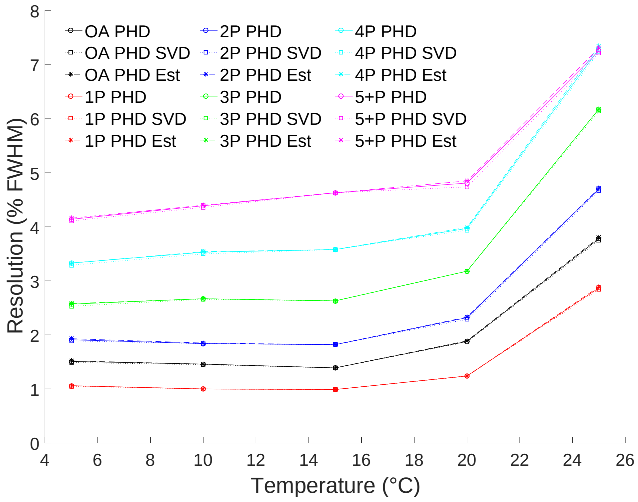

Figure 6.26: Comparison of resolution by event class for various models of PHD data in common-grid detector.

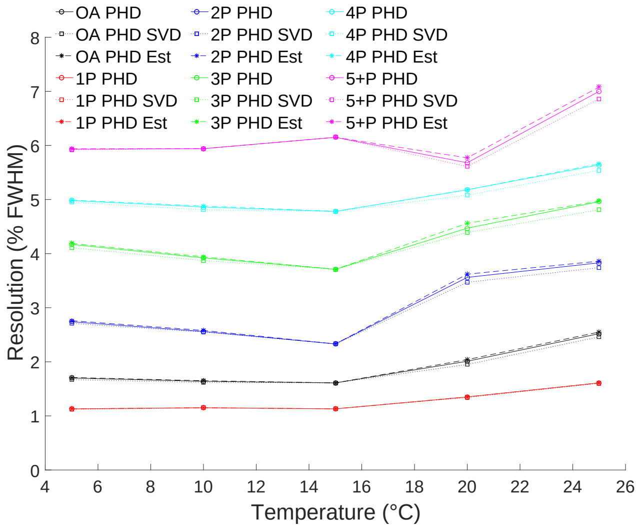

Figure 6.27: Comparison of resolution by event class for various models of PHD data in simple-pixel detector.

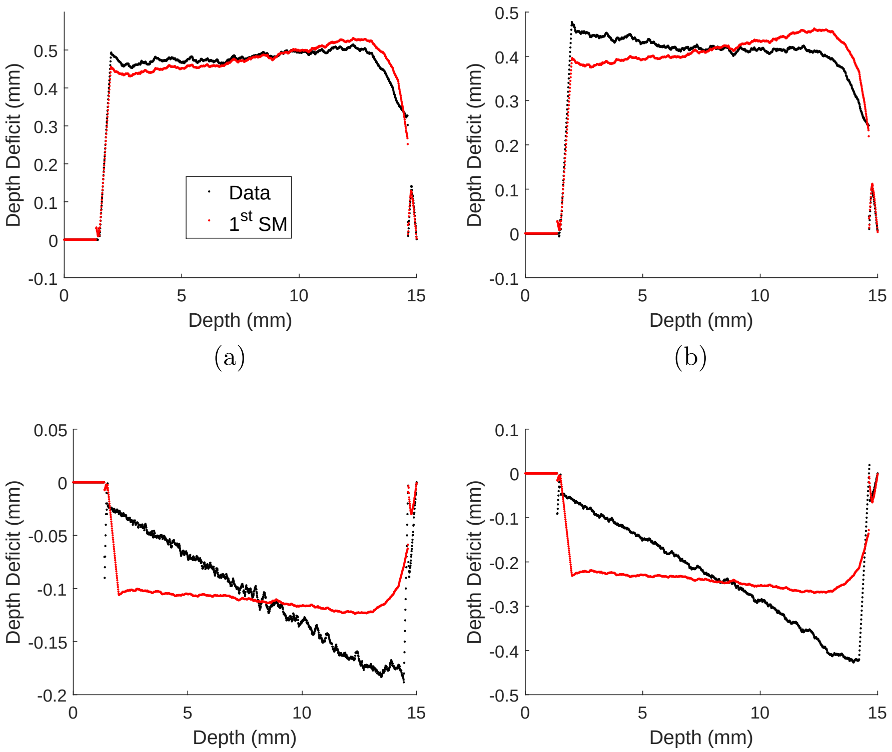

(a) (b)

(c) (d)

Figure 6.28: Original and reconstructed data from common-grid depth deficit SVD at 5°C (a), 10°C (b), 20°C (c), and 25°C (d).

common-grid detector of $2.87 * 10^{-2}$ and for the simple-pixel detector of $2.03 * 10^{-2}$. These relatively large values suggest a separable model is a poor approximation and that there are correlated effects of interaction depth and operating temperature on the depth deficit. This is confirmed visually by comparing the original depth deficit values to the reconstructed values from the first outer product matrix. This is shown for the common-grid detector in Figure 6.28 and for the simple-pixel detector in Figure 6.29. In both detectors, there is significant deviation between the original and reconstructed data, particularly at the extremes of depth near the electrodes.

Although the required data for the depth deficit correction cannot be reduced by taking different measurements at the pivot temperature than all other calibration temperatures, it can be reduced by using less data overall. The correction should depend on the number of events used, but plots of the depth deficit are visually indis-

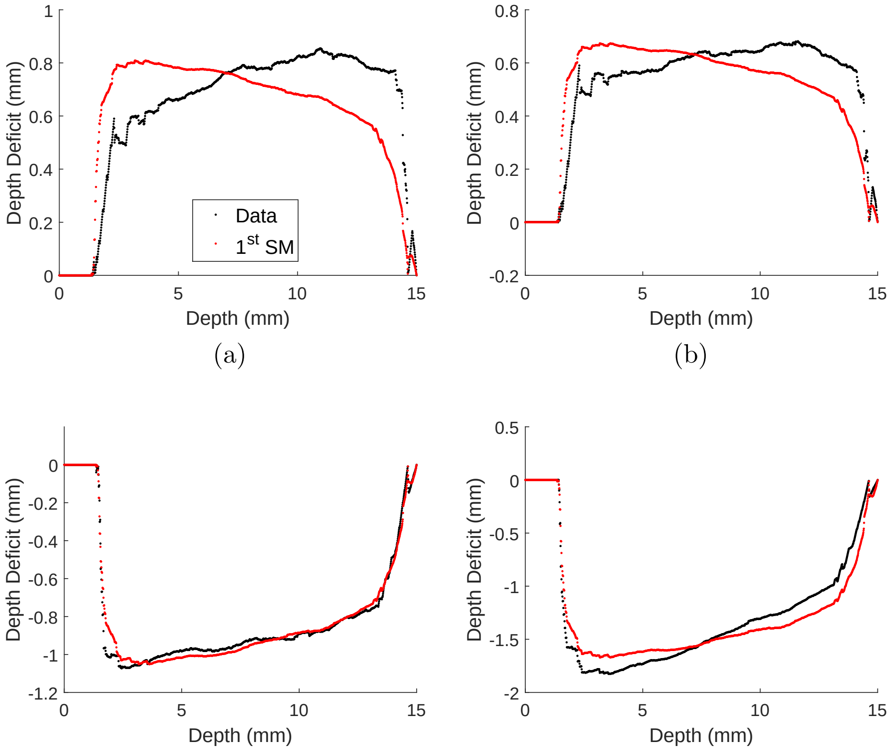

(a) (b) (c) (d)

Figure 6.29: Original and reconstructed data from simple-pixel depth deficit SVD at 5°C (a), 10°C (b), 20°C (c), and 25°C (d).

tinguishable using only 10 000 events at each temperature, and the correction factors are identical to four significant figures using only 100 000 events at each temperature. Therefore, instead of requiring the full 50 000 000 events collected during each voxel-wise Cs-137 calibration, only 100 000 are needed to accurately correction for depth deficit.

6.2.4 Depth Gain Separability

In each detector, the temperature-dependent depth gain correction is stored individually for each pixel as a two-dimensional array, with temperature on one axis and depth on the other. For each pixel, a matrix is built and an SVD performed analogously to the procedure described in section 6.2.3 with the matrix values equal to the centroid position. The deviation of the indices of separability from unity are shown in Figure 6.30.

In both detectors, the indices are very near unity and suggest that the effects of temperature and depth on centroid position are approximately separable. This is visually gauged by comparing the original data to reconstructed data of the first outer product matrix and further tested by examining the difference between the two datasets. For the common-grid detector, the raw and reconstructed data from the first pixel are compared in Figure 6.31, and the difference between the two is shown in Figure 6.32. For the simple-pixel detector, the raw and reconstructed data from the first pixel are compared in Figure 6.33, and the difference between the two is shown in Figure 6.34. The centroid uncertainty σ_{PPC} of each voxel is calculated directly from the resolution R_{FWHM}, as shown in equation (6.6).

$$\sigma_{ppc} = \frac{R_{FWHM}}{2.35 \times 100\%} \tag{6.6}$$

In both detectors, the channel-by-channel index of separability deviation from unity varies by an order of magnitude. This is a consequence of different temperature

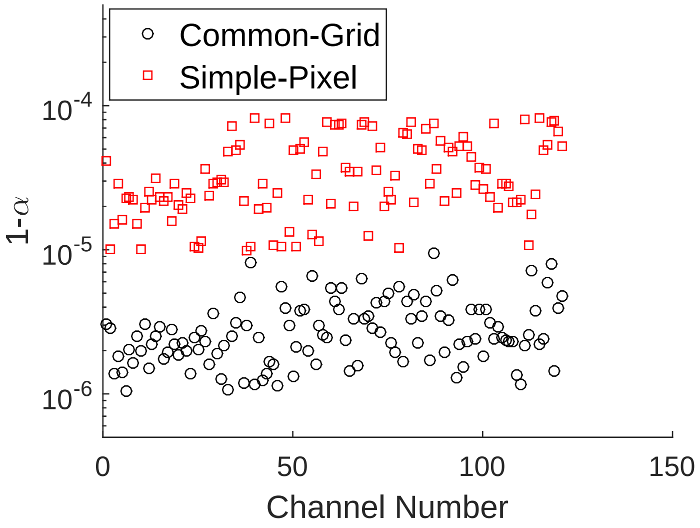

Figure 6.30: Deviations of the indices of separability from unity by channel for depth gain SVD.

trends in each pixel, and reinforces the assertion that the correction must be done independently for each pixel. Furthermore, the average index of separability deviation is an order of magnitude larger in the simple-pixel detector. This is caused by the greater cathode noise and resulting increased depth uncertainty in the simple-pixel detector, and does not represent a systematic difference between the detector types. It also manifests as larger deviations between the raw and reconstructed data in the simple-pixel detector than the common-grid detector. Finally, the small magnitude of the residual deviations in both detectors all being within the centroid uncertainty confirms that a separable model is an excellent approximation.

Because separability is a good approximation here, the limited spectroscopic data is tested with implementation identical to the PHD temperature correction described in 6.2.2. Once again only the pivot-temperature depth gain data is considered. The left-singular vector values are interpolated from the nearest calibration temperatures based on the operating temperature and used to adjust the depth gain. Once again this is a proof-of-concept test of separability because it still requires voxel-wise Cs-137 data at each temperature to generate the left-singular vector a priori. For prac-

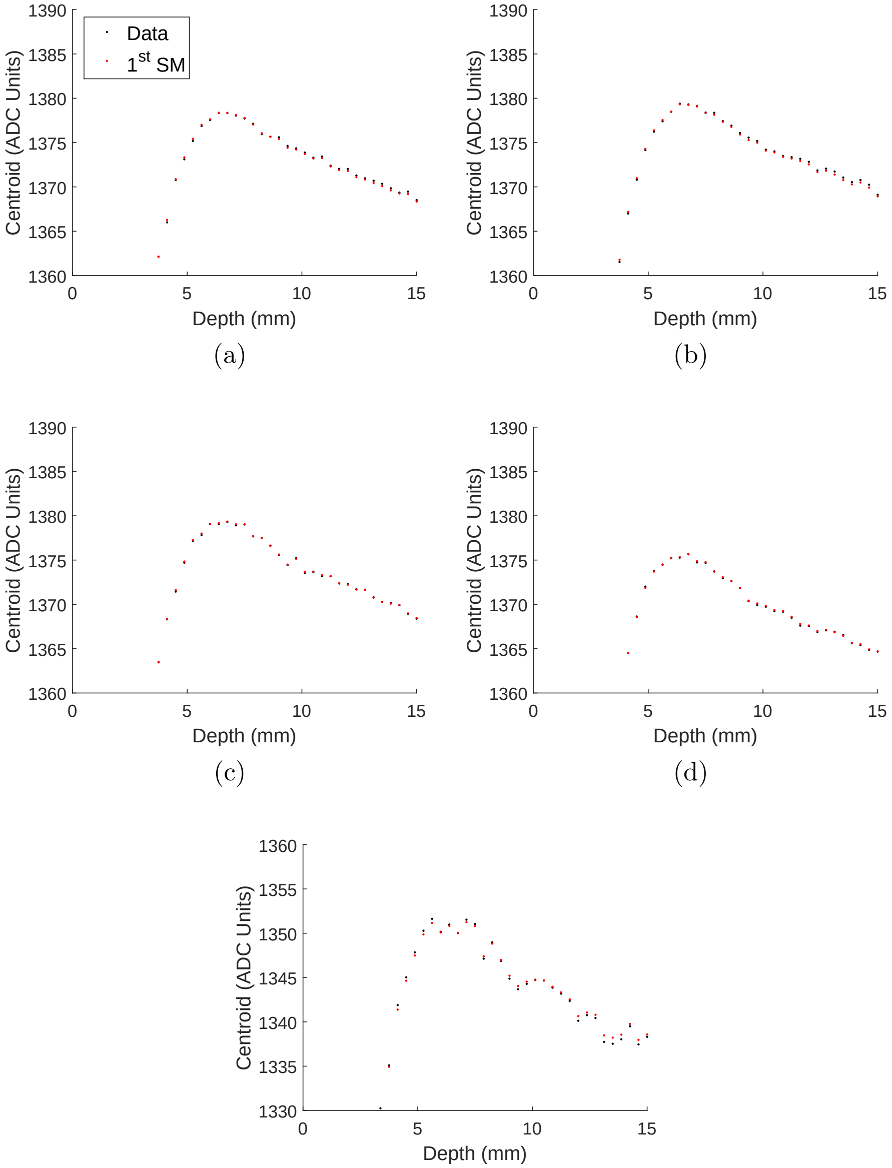

(a) (b) (c) (d) (e)

Figure 6.31: Original and reconstructed data from common-grid detector depth gain SVD in first pixel at 5°C (a), 10°C (b), 15°C (c), 20°C (d), and 25°C (e).

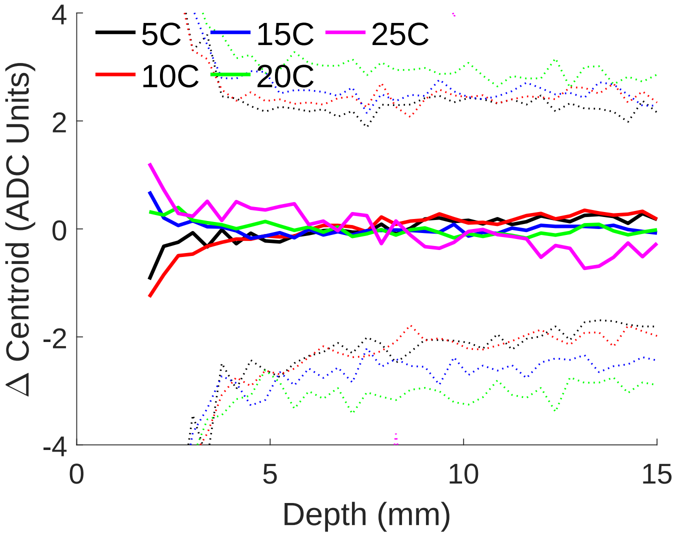

Figure 6.32: Deviation of depth gain SVD reconstructed data from original depth gain data taken at each temperature in the common-grid detector with data shown by solid lines and uncertainty bounds shown by dashed lines.

tical operation, the photopeak centroid for an entire pixel normalized to the pivot-temperature calibration value is used as an estimate of the left-singular vector. A comparison of the full temperature-dependent depth gain, SVD depth gain, and estimated SVD depth gain resolutions is shown for the common-grid detector in Figure 6.35 and for the simple-pixel detector in Figure 6.36.

In both detectors, there is negligibly small resolution degradation from substituting the full depth gain dataset with depth gain from a single temperature and an SVD temperature vector. Furthermore, approximating the temperature vector with photopeak position over all depths again causes negligibly small degradation. This means a voxel-wise Cs-137 calibration is only required at the pivot-temperature, and a pixel-wise Cs-137 calibration at each other calibration temperature is sufficient. During calibration each pixel is divided into 40 depth bins, so this represents a factor of 40 time reduction in the Cs-137 calibration time.

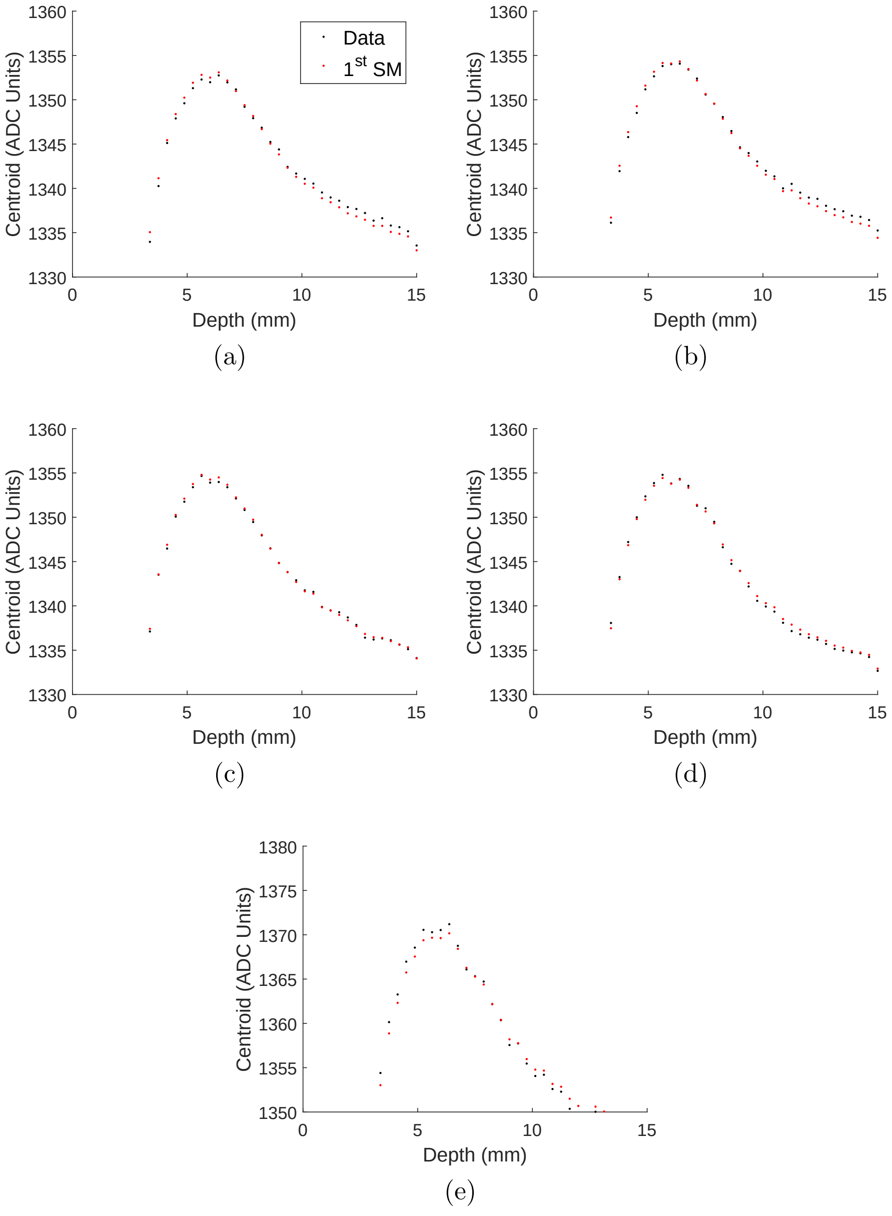

(a) (b) (c) (d) (e)

Figure 6.33: Original and reconstructed data from simple-pixel detector depth gain SVD in first pixel at 5°C (a), 10°C (b), 15°C (c), 20°C (d), and 25°C (e).

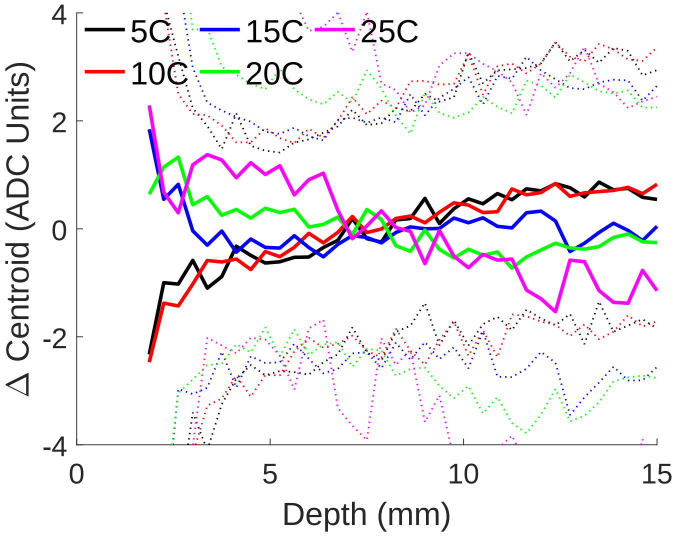

Figure 6.34: Deviation of depth gain SVD reconstructed data from original depth gain data taken at each temperature in the simple-pixel detector with data shown by solid lines and uncertainty bounds shown by dashed lines.

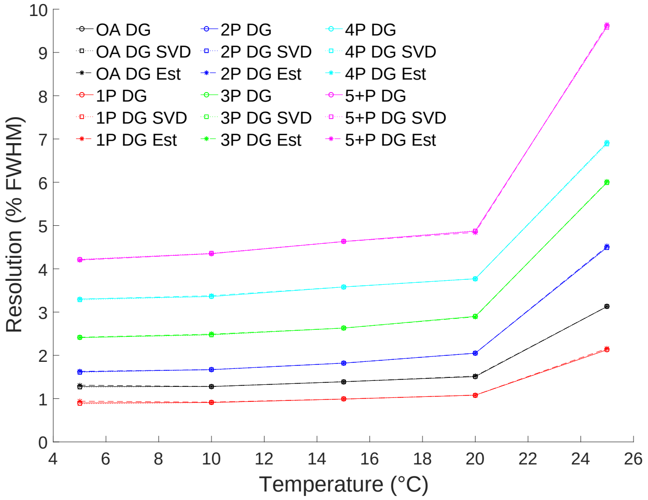

Figure 6.35: Comparison of resolution by event class for various models of temperature-dependent depth gain data in common-grid detector.

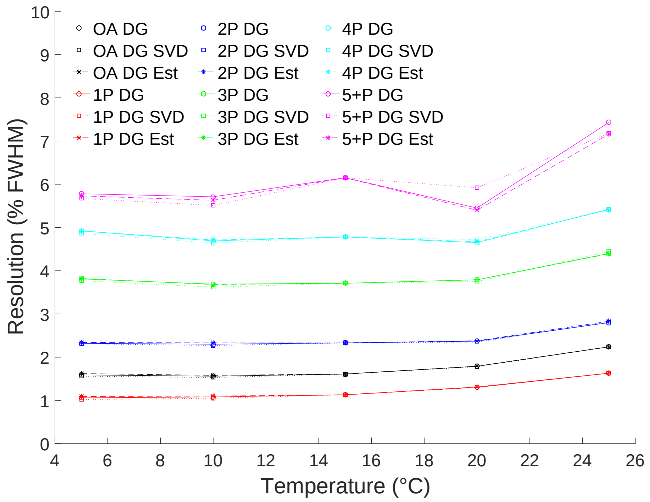

Figure 6.36: Comparison of resolution by event class for various models of temperature-dependent depth gain data in simple-pixel detector.

6.2.5 Nonlinearity Separability

There is no parametric temperature-dependent correction for energy nonlinearity because energy nonlinearity is the final correction performed during fixed-temperature calibration. Correcting during data processing cannot change any subsequent parameters, thus the results would be the same as correcting during post-processing. An event-by-event parametric correction is functionally identical to the overall nonlinearity correction while an incident-by-incident parametric correction is functionally identical to the pixelated nonlinearity correction both described in section 5.3.

Separability can still be gauged to determine the necessity of collecting nonlinearity data at every calibration temperature. This is tested both for the overall and pixelated nonlinearity correction. In both cases, the nonlinearity-corrected centroids are stored in a matrix with the rows corresponding to the calibration temperature and the columns corresponding to the centroids before correction. An SVD of the overall nonlinearity data yields of deviation of the index of separability from unity of $1.59 * 10^{-3}$ for the common-grid detector and of $1.14 * 10^{-3}$ for the simple pixel detector. These values suggests temperature and energy nonlinearity are fairly well

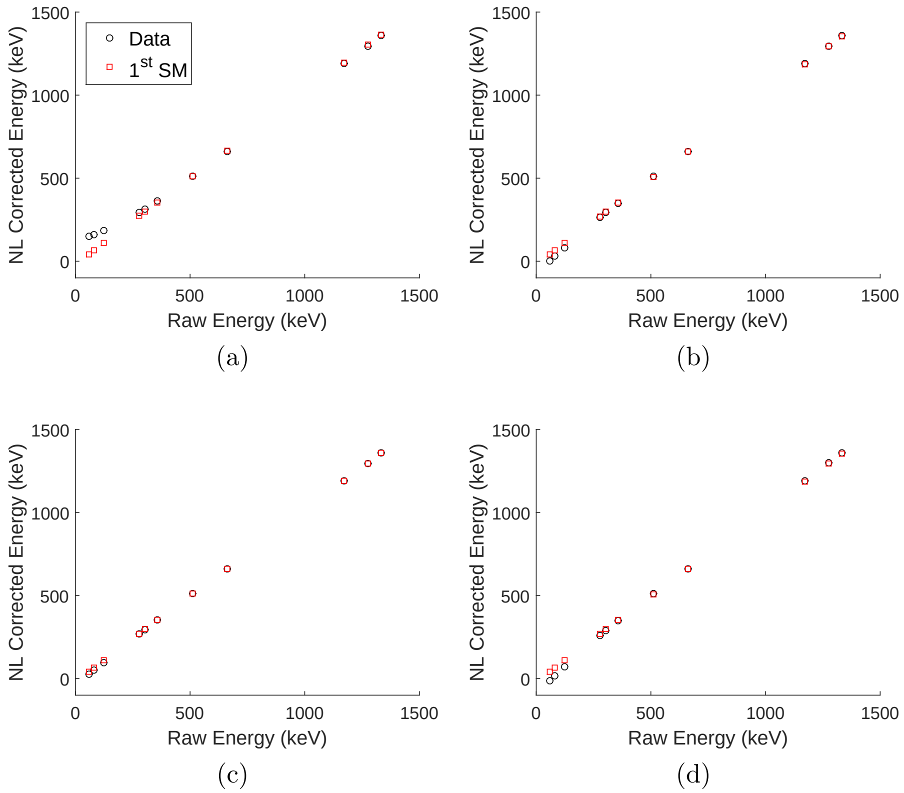

(a) (b) (c) (d)

Figure 6.37: Original and reconstructed data from common-grid detector overall energy nonlinearity SVD at 5°C (a), 10°C (b), 15°C (c), and 20°C (d).

approximated by a separable model. This is shown via a comparison of the original corrected centroids and the first outer-product matrix for the common-grid detector in Figure 6.37 with the residuals shown in Figure 6.38. An analogous comparison is shown for the simple-pixel detector in Figure 6.39 with the residuals shown in Figure 6.38.

The separable model fits the original data reasonable well everywhere except for the lowest energies at the temperature extremes, where there is significant deviation. A better approach is to look at each pixel individually. An SVD is performed on each pixel nonlinearity analogously to the overall nonlinearity, and index of separability deviations are shown in Figure 6.41. The magnitudes are very small in both detectors, indicating good separability. Moreover, in both detectors every pixel has better separability than the overall nonlinearity. Separability is an underlying assumption of the

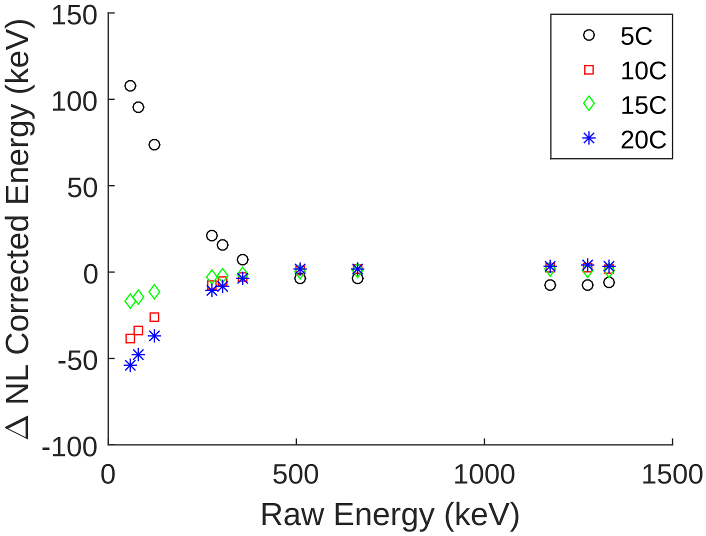

Figure 6.38: Deviation of nonlinearity SVD reconstructed data from original depth gain data taken at each temperature in the common-grid detector.

linear corrections implemented a posteriori. In section 5.5, the pixelated nonlinearity correction outperformed the overall nonlinearity correction despite the pixelated Cs-137-only correction performing worse than the overall Cs-137-only correction. This is likely a result of the better temperature-nonlinearity separability of individual pixels than the detectors overall.

The good separability by pixel also limits the amount of data required for correction. A full nonlinearity correction is only required at the pivot temperature, and a single energy calibration is sufficient at each other calibration temperature. The Cs-137 measurement taken for the temperature-dependent depth gain correction can fill this role, once again offering a substantial time savings. This is identical in implementation to using the Cs-137-only a posteriori correction, which only depends on the nonlinearity calibrations at the pivot temperature. Separability being a good approximation is further reinforced by the superior performance of the Cs-137-only corrections to the nonlinearity corrections.

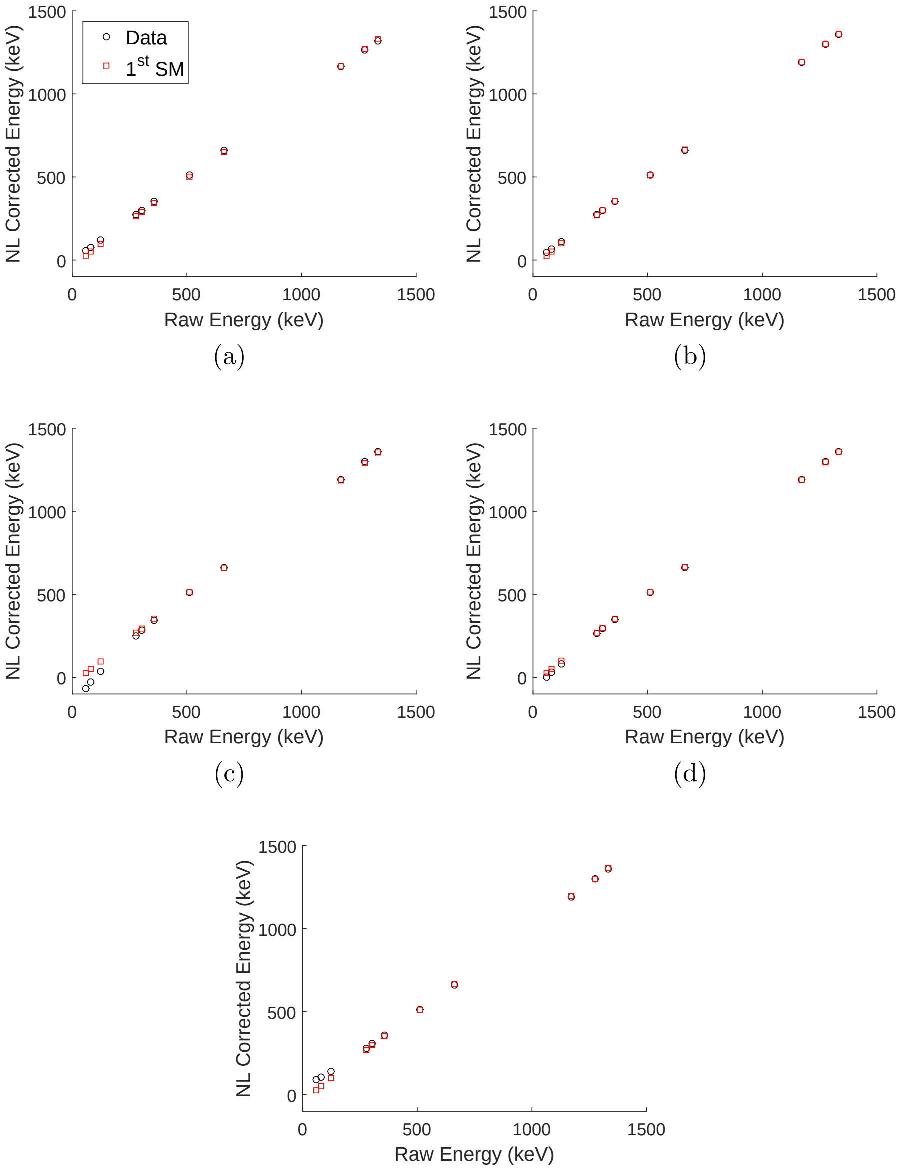

(a) (b) (c) (d) (e)

Figure 6.39: Original and reconstructed data from simple-pixel detector overall energy nonlinearity SVD at 5°C (a), 10°C (b), 15°C (c), 20°C (d), and 25°C (e).

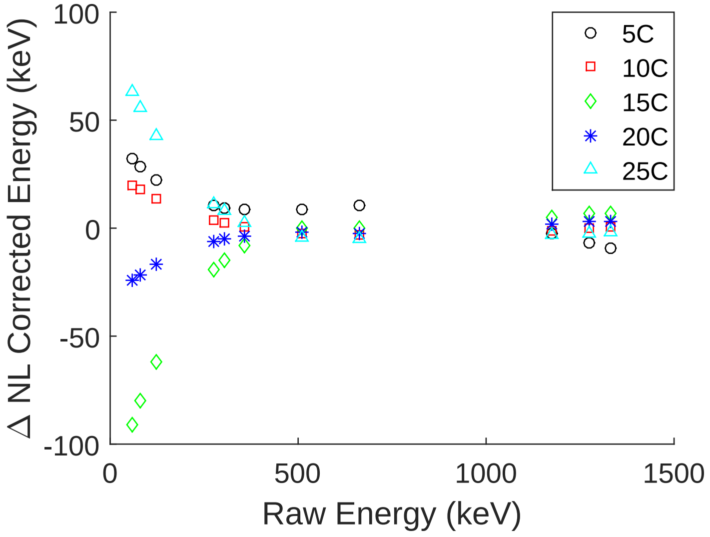

Figure 6.40: Deviation of nonlinearity SVD reconstructed data from original depth gain data taken at each temperature in the simple-pixel detector.

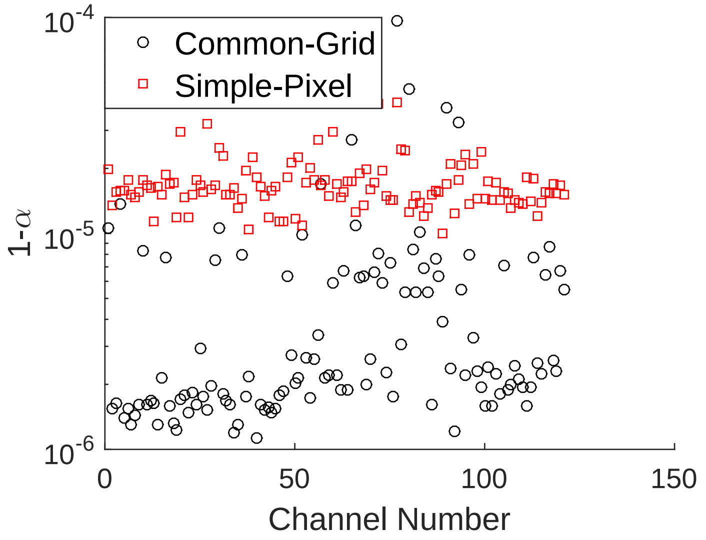

Figure 6.41: Deviations of the indices of separability from unity by channel for nonlinearity SVD.

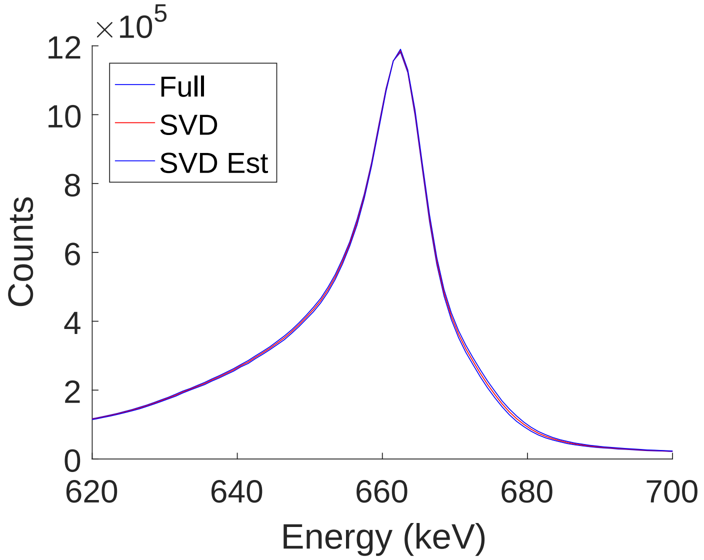

Figure 6.42: Comparison of the overall photopeaks using full and data-minimized parametric corrections.

6.2.6 Performance Impact on Ramp Measurements

The final test of data minimization techniques is to use them with the Cs-137 ramp measurement. A comparison of the photopeak using the full data corrections, the SVD corrections, and the estimated SVD corrections is shown in Figure 6.42. Each parametric correction is once again post-processed with an event-class Cs-137-only gain correction. There is a negligible shift in the overall photopeak from 661.78 keV to 661.80 keV using the SVD corrections, and to 661.82 keV using the estimated SVD. There is also a slight degradation in the overall resolution from 1.67% to 1.70% using the SVD corrections and to 1.72% using the estimated SVD.

6.3 Summary and Future Work

A careful examination of several calibration parameters yielded a method to recover performance losses introduced from large differences in calibration and operating temperatures. By correcting for the temperature variation in the peak-hold circuitry using the operating temperature, peaks are better aligned and resolution improves.

Table 6.2: Reduced Calibration Times for Temperature Other than Pivot Temperature

Measurement	Single Detector Time (hr:min)	18 Detector Array Time (hr:min)
Single- Amplitude PHD	0:01	0:01
Pixel-wise Cs-137	0:20	6:00
Total	0:21	6:01

This is especially true for low energy events and manifests for the Cs-137 calibration in the high event class spectra. By adding back the depth deficit as a function of operating temperature, events are reconstructed nearer where they physically occurred. Finally by adjusting the voxel-by-voxel gain as a function of operating temperature, almost all temperature-induced resolution degradation is recovered. The corrections in conjunction with a linear a posteriori Cs-137 correction generate a spectrum for the ramping temperature measurement comparable to a fixed-temperature measurement.

The parametric temperature corrections can be performed with much less calibration data. Because the effects of temperature and amplitude on the PHD values are separable for the peak-hold times of real events, a single PHD calibration is sufficient. Because the effects of temperature and depth on the gain are separable, a single voxel-wise Cs-137 calibration sufficient. Because the effects of temperature and incident energy on nonlinearity are separable, a single nonlinearity calibration is sufficient. At all calibration temperatures other than the pivot temperature, only a single-amplitude PHD measurement and a pixel-wise Cs-137 calibration are needed, with time requirements summarized in Table 6.2. Including equilibration time following temperature changes, up to three calibrations can be performed per day. This makes the pivot-temperature calibration the most significant bottleneck and means an array system can be calibrated for floating temperature operation only two days after it is calibrated for fixed temperature operation.

Floating temperature operation opens the doors to a lot of future work. In the immediate future, the robustness of the algorithm should be tested by slightly altering the operating conditions. Further down the road, an existing system should be tested outside of laboratory conditions with temperature correction. Finally, this algorithm should be tested with and refined for different detector types and ASICs.

6.3.1 Algorithm Testing

The largest limitation of the temperature correction algorithms developed in this work is the limited energy range. While the GMI analog ASIC has a dynamic range up to 3 MeV, the highest energy photopeak considered was 1408 keV. This limitation is minor because only the nonlinearity corrections would be affected, but is fairly simple albeit time-intensive to address. Including measurements of a Na-24 source with a photopeak at 2754 keV would include nearly all of the ASIC dynamic range and should be completed whenever such a source is available. Additionally, the separability of energy nonlinearity from temperature suggests that the existing correction algorithm will be successful at energies other than 661.7 keV, but this should be tested with a Eu-152 temperature ramp measurement.

Because data minimization drastically speeds up the calibration time at temperatures other than the pivot temperature, the effects of varying the number of calibrations should be studied. The performance degradation resulting from very few calibrations and interpolation over a wide temperature range should be quantified. Additionally, the number of calibrations should be increased so interpolation occurs over a narrow range. The performance degradation should be examined as a function of temperature steps between calibrations, where the optimal temperature step is the largest step after degradation reaches its minimum.

Finally, the effects of temperature on imaging should be studied. Properly reconstructing the spatial coordinates of each event is paramount in both Compton and coded aperture imaging modalities. Because the reconstructed depth of interaction changes as a function of temperature, floating temperature operation is expected to blur the image. The depth-deficit correction is therefore expected to mostly remove that blur. Testing these expectations would require a much larger environmental chamber so the source can be placed in different positions further from the detector. It would additionally require longer count times or hotter sources to account for this greater distance, making this difficult but important to study in the future.

6.3.2 System Fielding

This work considers a range of temperatures useful for indoor operation, but it was limited at the upper end to prevent ASIC damage and at both ends due to time constraints. The upper and lower bounds of the temperature correction should be studied. Lowering the minimum temperature presents no known risk to the detectors or ASICs and would be useful for outdoor detector operation in arctic environments. Raising the maximum temperature can damage the ASICs above 35°C due to increased leakage current overloading the compensation circuit. This study should therefore ideally be done with simple-pixel detectors because of their reduced leakage current and more linear leakage response to temperature. This would be useful for hot-environment operation, such as in a power-plant, underground, or outdoors in a tropical environment.

After establishing temperature bounds both for the effectiveness of the correction algorithm and for the safe operation of the hardware, the system should be operated without temperature regulation. This would begin in a lab environment with very little external temperature variation, but should ultimately expand to outdoor operation. Here humidity is a concern, so additional work should be done to study the spectroscopic effects of humidity or to hermetically seal the detector modules.

6.3.3 Alternate Hardware

The temperature correction algorithms were shown to be effective for large-volume CZT detectors mounted on GMI analog ASICs in a test box. The simplest extension of this is a Polaris array system, which uses the same hardware but has 18 detectors instead of two. The temperature correction is expected to work the same, but must be tested. It should also be tested on the BNL analog ASIC, where the detector-specific corrections are expected to work the same but the PHD correction is not. The BNL analog ASIC uses peak-sampling rather than peak-hold circuitry, so the effects of temperature on this component should be studied. Finally, the temperature correction should be implemented on the GMI digital ASIC, where PHD corrections are unnecessary because the digitized waveform is sampled on an event-by-event basis. Still, it is important to test the effectiveness of the detector-specific corrections, and determine the effect of temperature on the additional subpixel position information only available with the digital ASIC.

The temperature correction algorithms should also be tested with different detectors. Due to the small pixel effect covering a larger portion of the detector bulk, the depth reconstruction is poorer in thin detectors near the anode. The magnitude of depth deficit and the effectiveness of the correction should be studied in 5 mm and 10 mm thick detectors.

BIBLIOGRAPHY

BIBLIOGRAPHY

[1] H. A. Bethe. The range-energy relation for slow alpha-particles and protons in air. *Reviews of Modern Physics*, 22:213–219, Apr 1950.

[2] P. Steinmeyer. Beta-particle shielding. *Radiation Protection Management*, 6:71–76, 1989.

[3] V. McLane, C.L. Dunford, and P.F. Rose. *Neutron cross sections: Volume 2, Neutron cross section curves.* Academic Press, Inc., Jan 1988.

[4] S.A. Pozzi, Y. Xu, T. Zak, S.D. Clarke, M. Bourne, M. Flaska, T.J. Downar, P. Peerani, and V. Protopopescu. Fast neutron spectrum unfolding for nuclear non-proliferation and safeguards applications. *Nuovo Cimento C*, 33:207–214, 2010.

[5] J.H. Hubbell. Photon cross sections, attenuation coefficients, and energy absorption coefficients from 10 kev to 100 gev. *Nuovo Cimento C*, Aug 1969.

[6] *Nuclides and Isotopes : Chart of the Nuclides, 17th Edition.* Knoll Atomic Power Laboratory: Bechtel, 2010.

[7] D.H. Wilkinson. *Ionization Chambers and Counters.* Cambridge University Press, 1950.

[8] B.B. Benson. Design of a proportional counter for gammarays. *"Review of Scientific Instruments*, 17:533–536, 1946.

[9] W.K. Sinclair. Comparison of geiger-counter and ion-chamber methods of measuring gamma radiation. *Nucleonics*, 7:21–26, Dec 1950.

[10] J.B. Birks, D.W. Fry, L. Costrell, and K. Kandiah. *The Theory and Practice of Scintillation Counting.* Pergamon Press, 1964.

[11] I. Holl, E. Lorenz, and G. Mageras. A measurement of the light yield of common inorganic scintillators. *IEEE Transactions on Nuclear Science*, 35, Oct 1987.

[12] R.B. Owen and A.E.A. Harwell. The decay times of organic scintillators and their application to the discrimination between particles of differing specific ionization. *IRE Transactions on Nuclear Science*, 5:198–201, Dec 1958.

[13] D.C. Northrop and O. Simpson. Semiconductor counters: I. theory. *Proceedings of the Physical Society*, 80:262, 1962.

[14] S. Sasaki, H. Tawara, K. Saito, M. Miyajima, and E. Shibamura. Average energy required per scintillation photon and energy resolution in inorganic, scintillation crystals for gamma-rays. *High Energy Accelerator Research Organization*, 2:976–979, Nov 2001.

[15] A. Owens. Compound semiconductor radiation detectors. *Nuclear Instruments and Methods in Physics A*, 531:18–37, Sep 2004.

[16] A.H. Compton. A quantum theory of the scattering of x-rays by light elements. *Physics Review*, 21:483–502, May 1923.

[17] H. Hall. The theory of photoelectric absorption for x-rays and -rays. *Review of Modern Physics*, 8:358, Oct 1936.

[18] L. Nedelsky and J.R. Oppenheimer. The production of positives by nuclear gamma-rays. *Physical Review*, 44:948–949, 1933.

[19] R.D. Evans. *The Atomic Nucleus*. McGraw Hill, 1955.

[20] R. Trammell and F.J. Walter. The effects of carrier trapping in semiconductor gamma-ray spectrometers. *Nuclear Instruments and Methods*, 76:317–321, Dec 1969.

[21] S. Krishna, R.S. Scott, and B. J. Baliga. Optimum semiconductors for high-power electronics. *IEEE Transactions on Electron Devices*, 36:1811–1823, 1989.

[22] M.J. Berger, J.H. Hubbell, S.M. Seltzer, J. Chang, J.S. Coursey, R. Sukumar, D.S. Zucker, and K. Olsen. Xcom: Photon cross section database (version 1.5). http://physics.nist.gov/xcom, Nov 2010.

[23] M. Khandaker. High purity germanium detector in gamma-ray spectrometry. *International Journal of Fundamental Physical Sciences*, 1:42–46, Jun 2011.

[24] *Germanium Detectors*, Mar 2014. http://www.canberra.com/products/detectors/pdf/Germani Det-SS-C39606.pdf.

[25] F. Nava, G. Bertuccio, A. Cavallini, and E. Vittone. Silicon carbide and its use as a radiation detector material. *Measurement Science and Technology*, 19, Aug 2008.

[26] Shaw K.S., J.C. Lund, F. Olschner, L. Moy, and M.R. Squillante. Thallium bromide radiation detectors. *IEEE Transactions on Nuclear Science*, 36:199–202, Feb 1989.

[27] T. Takahashi, T. Mitani, Y. Kobayashi, M. Kouda, G. Sato, S. Watanabe, Nakazawa K., Y. Okada, M. Funaki, R. Ohno, and K. Mori. High-resolution schottky cdte diode detector. *IEEE Transactions on Nuclear Science*, 49:1297–1303, Jun 2002.

[28] A.A. Melnikov. Cdznte radiation detectors. *Journal of Crystal Growth*, 197:663–665, Feb 1999.

[29] G. Li, W. Jie, T. Wang, and G. Yang. Impurities in cdznte crystal grown by vertical bridgman method. *Nuclear Instruments and Methods A*, 534:511–517, Dec 2004.

[30] J. Baciak. *Development of pixilated HgI2 radiation detectors for room temperature gamma-ray spectroscopy.* PhD thesis, University of Michigan, 2004.

[31] W. Koehler, Z. He, C. Thrall, S. O'Neal, H. Kim, L. Cirignano, and K. Shah. Quantitative investigation of room-temperature breakdown effects in pixelated tlbr detectors. *IEEE Transactions on Nuclear Science*, 61:2573–2578, Oct 2014.

[32] S.A. Awadalla, J. Mackenzie, H. Chen, B. Redden, G. Bindley, Duff M.C., A. Burger, M. Groza, V. Buliga, J.P. Bradley, Dai Z.R., N. Teslich, and D.R. Black. Characterization of detector-grade cdznte crystals grown by traveling heater method (thm). *Journal of Crystal Growth*, 312:507–513, Feb 2010.

[33] F. Zhang and Z. He. 3d position-sensitive cdznte gamma-ray spectrometers: improved performance with new asics. *Proceedings of SPIE*, 5540:135–143, 2004.

[34] Z. He, G.F. Knoll, D.K. Wehe, R. Rojeski, C.H. Mastrangelo, M. Hamming, C. Barrett, and A. Uritani. 1-d position sensitive single carrier semiconductor detectors. *Nuclear Instruments and Methods A*, 380:228–231, 1996.

[35] Z. He, G.F. Knoll, D.K. Wehe, and Du Y.F. Coplanar grid patterns and their effect on energy resolution of cdznte detectors. *Nuclear Instruments and Methods A*, 411:107–113, 1998.

[36] D.S. McGregor, Z. He, H.A. Seifert, R.A. Rojeski, and D.K. Wehe. Cdznte semiconductor parallel strip frisch grid radiation detectors. *IEEE Transactions on Nuclear Science*, 45:443–449, Jun 1998.

[37] Z. He, W. Li, G.F. Knoll, Wehe D.K., J. Berry, and C.M. Stahle. 3-d position sensitive cdznte gamma-ray spectrometers. *Nuclear Instruments and Methods A*, 422:173–178, Feb 1999.

[38] A. Ruzin and Y. Nemirovsky. Methodology for evaluation of mobility-lifetime product by spectroscopy measurements in cdznte spectrometers. *Journal of Applied Physics*, 82:4166, Jul 1997.

[39] Y.A. Boucher, F. Zhang, W. Kaye, and Z. He. New measurement technique for the product of the electron mobility and mean free drift time for pixilated semiconductor detectors. *Nuclear Instruments and Methods A*, 671:1–5, Apr 2012.

[40] S.A. Soldner, A.J. Narvett, D.E. Covalt, and C. Szeles. Characterization of the charge transport uniformity of cdznte crystals for large-volume nuclear detector applications. *IEEE Transactions on Nuclear Science*, 51:2443–2447, Oct 2004.

[41] J. Mackenzie, H. Chen, S.A. Awadalla, P. Marthandam, B. Redden, G. Bindley, Z. He, D.R. Black, M. Duff, M. Amman, J.S. Lee, P. Luke, M. Groza, and A. Burger. Recent advances in thm czt for nuclear radiation detection. *MRS Proceedings*, 1164, Jul 2009.

[42] W. Li, Z. He, G.F. Knoll, D.K. Wehe, and C.M. Stahle. Spatial variation of energy resolution in 3-d position sensitive czt gamma-ray spectrometers. *IEEE Transactions on Nuclear Science*, 46:187–192, Jun 1999.

[43] M. Prokesch and C. Szeles. Accurate measurement of electrical bulk resistivity and surface leakage of cdznte radiation detector crystals. *Journal of Applied Physics*, 100, Jul 2006.

[44] S. Ramo. Currents induced by electron motion. *Proceedings of the IRE*, 27:584–585, 1939.

[45] G. Cavelleri, E. Gatti, G. Fabri, and V. Svelto. Extension of ramo's theorem as applied to induced charge in semiconductor detectors. *Nuclear Instruments and Methods*, 92:137–140, Mar 1971.

[46] Z. He. Review of the shockley-ramo theorem and its application in semiconductor gamma-ray detectors. *Nuclear Instruments and Methods A*, 463:250–267, May 2001.

[47] O. Bunemann, T.E. Cranshaw, and J.A. Harvey. Design of grid ionization chambers. *Canadian Journal of Research*, 27a:191–206, May 1949.

[48] R.M. Krishna, S.K. Chaudhuri, K.J. Zavalla, and K.C. Mandal. Characterization of cd0.9zn0.1te based virtual frisch grid detectors for high energy gamma ray detection. *Nuclear Instruments and Methods A*, 701:208–213, Feb 2013.

[49] Z. He. Potential distribution within semiconductor detectors using coplanar electrodes. *Nuclear Instruments and Methods A*, 365:572–575, Nov 1995.

[50] J.L. Matteson, F. Duttweiller, G.L. Huszar, P.C. Leblanc, R.T. Skelton, E.A. Stephan, P.L. Hink, P.F. Dowkontt, Slavis K.R., T.O. Tumer, and S.D. Kravis. Position-sensitive czt detector module. *Proceedings SPIE*, 3446, Jul 1998.

[51] W. Li, Z. He, Knoll G.F., Wehe D.K., and J. Berry. A data acquisition and processing system for 3d position sensitive czt gamma-ray spectrometers. *IEEE Transactions on Nuclear Science*, 46:1989–1994, Dec 1999.

[52] M.D. Wilson, R. Cernik, H. Chen, C. Hansson, K. Iniewski, Jones L.L., P. Seller, and M.C. Veale. Small pixel czt detector for hard x-ray spectroscopy. *Nuclear Instruments and Methods A*, 652:158–161, Oct 2011.

[53] Y.F. Du, Z. He, G.F. Knoll, and D.K. Wehe. Evaluation of a compton scattering camera using 3-d position sensitive cdznte detectors. *Nuclear Instruments and Methods A*, 457:203–211, Jan 2001.

[54] G.F. Knoll. *Radiation Detection and Measurement, 3rd Edition*. John Wiley and Sons, Inc., 2000.

[55] J. Jaworski. *Compton Imaging Algorithms for Position-Sensitive Gamma-Ray Detectors in the Presence of Motion*. PhD thesis, University of Michigan, 2013.

[56] S. Joshi. *Coded Aperture Imaging Applied to Pixelated CdZnTe Detectors*. PhD thesis, University of Michigan, 2014.

[57] A.E. Bolotnikov, J. Butcher, G.S. Camarda, Y. Cui, G. De Geronimo, J. Fried, Gul R., P.M. Fochuk, M. Hamade, A. Hossain, K.H. Kim, O.V. Kopach, M. Petryk, E. Vernon, G. Yang, and R.B. James. Array of virtual frisch-grid czt detectors with common cathode readout for correcting charge signals and rejection of incomplete charge-collection events. *IEEE Transactions on Nuclear Science*, 59:1544–1551, Mar 2012.

[58] C.E. Seifert, M.J. Myjak, and D.V. Jordan. Simulated performance of the gamma tracker cdznte handheld radioisotope identifier. *IEEE Nuclear Science Symposium Conference Record*, 2:940–944, 2007.

[59] F. Zhang, Z. He, and D. Xu. Improved resolution for 3-d position sensitive cdznte spectrometers. *IEEE Transactions on Nuclear Science*, 51:2427–2431, May 2004.

[60] Y.A. Boucher. *Analysis of Cadmium Zinc Telluride Detector Performance and Characteristics for Applications in Gamma-Ray Imaging Spectrometers*. PhD thesis, University of Michigan, 2013.

[61] F. Zhang, C. Herman, De Geronimo G., E. Vernon, and J. Fried. Characterization of the h3d asic readout system and 6.0 cm3 3-d position sensitive cdznte detectors. *IEEE Transactions on Nuclear Science*, 59:233–243, Feb 2012.

[62] H. Yang. *Applications of Digital ASIC Array System for Noise Analysis, Nonlinearity Correction, Event Classification and Reconstruction*. PhD thesis, University of Michigan, 2013.

[63] J.C. Kim, S.E. Anderson, W. Kaye, F. Zhang, Y. Zhu, S. Joshi, and Z. He. Charge sharing in common-grid pixelated cdznte detectors. *Nuclear Instruments and Methods A*, 654:233–243, Oct 2011.

[64] L. Meng and Z. He. Exploring the limiting timing resolution for large volume czt detectors with waveform analysis. *Nuclear Instruments and Methods A*, 550:435–445, Sep 2005.

[65] W. Kaye. *Energy and Position Reconstruction in Pixelated CdZnTe Detectors*. PhD thesis, University of Michigan, 2012.

[66] W. Kaye, Y.A. Boucher, F. Zhang, and Z. He. Calibration and operation of the polaris 18-detector cdznte array. *IEEE Nuclear Science Symposium Conference Record*, pages 3821–3824, 2010.

[67] W. Kaye, Y.A. Boucher, F. Zhang, J. Mann, and Z. He. Operational considerations due to cdznte detector problems. SORMA Conference Presentation, May 2012.

[68] W. Li, Z. He, G.F. Knoll, Wehe D.K., and J. Berry. Experimental results from an imarad 88 pixellated czt detector. *Nuclear Instruments and Methods A*, 458:518–526, Feb 2001.

[69] A.E. Bolotnikov, S.E. Boggs, H. Chen, W.R. Cook, F.A. Harrison, and S. M. Schindler. Properties of pt schottky type contacts on high-resistivity cdznte detectors. *Nuclear Instruments and Methods A*, 482:395–407, Apr 2002.

[70] Rogers Corporation. *curamik Ceramic Substrates*, 2016. rev. 2.16 eng. https://www.rogerscorp.com/documents/3009/pes/curamik/curamik-Ceramic-Substrates-Product-Information.pdf.

[71] F. Zhang. *Events reconstruction in 3-D position sensitive CdZnTe gamma-ray spectrometers*. PhD thesis, University of Michigan, 2005.

[72] Vishay. *Lower Voltage Ceramic DC Disc Capacitors*, Mar 2015. http://www.vishay.com/docs/23108/561r.pdf.

[73] G. Strang. *Linear Algebra and Its Applications, 4th edition.* Thomson, Brooks/Cole, 2006.

[74] V.C. Klema and A.J. Laub. The singular value decomposition: Its computation and some applications. *IEEE Transactions on Automatic Control*, 25:164–176, Apr 1980.